Title
Collective Dynamics and Coherent Diagnostics of Microbunched Relativistic Electron Beams

Author
Marinelli, Agostino

Publication Date
2012

Peer reviewed|Thesis/dissertation

University of California
Los Angeles

Collective Dynamics and Coherent Diagnostics of Microbunched Relativistic Electron Beams

A dissertation submitted in partial satisfaction
of the requirements for the degree
Doctor of Philosophy in Physics

by

Agostino Marinelli

2012

Abstract of the Dissertation

Collective Dynamics and Coherent Diagnostics of Microbunched Relativistic Electron Beams

by

Agostino Marinelli

Doctor of Philosophy in Physics

University of California, Los Angeles, 2012

Professor James B. Rosenzweig, Chair

The x-ray free-electron laser has established itself as the brightest available source of x-rays, extending the coherence and brilliance properties of conventional atomic lasers down to the sub-Angstrom level. The high-brightness electron beams that are used to drive the free-electron laser process, undergo a number of collective instabilities that can generate complex phase-space structures and induce the emission of coherent radiation, an effect that is generally termed microbunching instability.

The main subject of this dissertation is the collective evolution of beam microbunching under the effect of longitudinal space-charge forces. We develop a three-dimensional kinetic theory of space-charge effects leading to collective suppression and amplification of beam microbunching. This model gives, for the first time, a fully self-consistent description of the space-charge instability, with the inclusion of three-dimensional and thermal effects. After establishing a self-consistent theoretical foundation for space-charge effects, we present two experiments related to the space-charge instability. The generation of broadband coherent undulator radiation with a longitudinal space-charge amplifier is demonstrated experimentally for the first time. This experiment extends the capabilities of free-electron laser facilities by allowing the generation of coherent broadband radiation pulses, thus accessing regimes of operation currently unavailable for fourth generation light sources. Finally a coherent diffraction imaging technique for the reconstruction of beam microbunching is designed and experimentally tested. This technique is based on the application of an oversampling phase-retrieval method to the far-field coherent transition radiation emitted by a microbunched electron beam and has applications in the diagnostic of compressed electron beams and free-electron lasers.

While the microbunching instability is generally regarded as a detrimental effect, this work shows that the coherent effects associated with the induced microbunching can be optimized and used to our advantage for the development of new coherent radiation sources and advanced beam diagnostics.

The dissertation of Agostino Marinelli is approved.

Matteo Pellegrini

George J. Morales

Claudio Pellegrini

James B. Rosenzweig, Committee Chair

University of California, Los Angeles

2012

To my Parents . . .

Table of Contents

List of Figures

Acknowledgments

These years at UCLA have been a great time for me, both personally and scientifically. The Physics and Astronomy Department, and the particle beam physics laboratory made for a lively and collaborative environment, that greatly contributed to my personal and scientific growth.

First of all, I want to acknowledge my advisor Prof. James B. Rosenzweig. There are so many reasons to thank him that listing them all would be impossible, from recommending my move to UCLA (which turned out to be the best professional choice I could possibly make), to the constant support and inspiration through these years of graduate school. His contagious excitement for science and innovation has guided my doctoral work and I hope to be able to pass along our enthusiasm to the readers of this dissertation. I am also deeply indebted to Prof. Claudio Pellegrini. Working with him in these years has been a great opportunity for my scientific career and his advice on how to live in America as an Italian have helped my adaptation and contributed to make me feel less far from home.

I am also grateful to many collaborators and teachers. Prof. Pietro Musumeci has always been there for fruitful and enjoyable discussions about physics or slightly less fruitful but equally enjoyable discussions about soccer. Prof. George J. Morales has had a fundamental part in my doctoral research, triggering my work on the kinetic theory of space-charge effects with his enlightening lectures on the physics of plasmas. I am grateful to Prof. Jianwei Miao for his invaluable guidance on the methods of phase-retrieval and coherent diffraction imaging, which have made possible the experiment on microbunching imaging that is presented here. I thank Prof. Matteo Pellegrini for agreeing to serve in my committee and reading this dissertation. Finally I want to acknowledge Prof. Luigi Palumbo of the University of Rome for introducing me to the field of free-electron lasers and particle accelerators in the early years of my research career.

My friend and colleague Erik Hemsing requires a special mention: he first taught me the fun of theoretical work and then shared with me the thrill of taking experimental data at four in the morning. He has given a valuable contribution to the development of the kinetic theory of the space-charge amplifier and helped me in setting up and performing the diffraction imaging and space-charge amplifier experiments that are presented in this dissertation. Likewise, I want to acknowledge my friend, and soon to be colleague, Daniel Ratner for many useful discussions on the dangerous areas of the microbunching instability.

I also want to thank the whole NLCTA team: Mike Dunning, Stephen Weathersby, Dao Xiang and Carsten Hast. The support of the NLCTA folks has been vital for the success of my experimental work and I am deeply grateful to them. Many thanks also to Finn O'Shea and Ivan Gadjev for their help at SLAC and Doctor Zhirong Huang, Prof. Avraham Gover and Doctor Kwang-Je Kim for many useful discussions.

On a more personal note, I want to acknowledge the people that have made my time in L.A. unforgettable. My great friends Giacomo, Isabella and Guido, with whom I have shared every bit of these four and a half years of life in the USA: from our Hawaiian adventures to our countless barbecue dinners, to our endless apartment hunts. I will treasure our memories in the years to come. Also, many thanks to my family: Mamma, Papa', Pietro, Betta, Jon, Serena and Sofia, who have kept supporting and loving me from the opposite side of the world. And, finally, Megan, who is the best gift that California could possibly give me.

Vita

Sept. 2008 to June. 2012	Physics Division Fellowship *Physics and Astronomy Department, University of California, Los Angeles*
Sept. 2008 to Oct. 2012	Graduate Student Researcher *Physics and Astronomy Department, University of California, Los Angeles*
Mar. 2008 to Aug. 2008	Visiting Scientist *Physics and Astronomy Department, University of California, Los Angeles*
Jan.2007 to Nov. 2007	Research Assistant (Undergraduate Research Fellowship) *Laboratori Nazionali di Frascati, INFN*
July 2007	2nd Level Laurea Degree (MS equivalent) Cum Laude in Engineering Science with Emphasis on Applied Physics. *University of Rome, La Sapienza (Italy)*
Jan. 2006 June 2006	Exchange Student. (Socrates Erasmus Fellowship) *Royal Institute of Technology, Stockholm, Sweden*
Feb. 2005	1st Level Laurea Degree (BS equivalent) Cum Laude in Electrical Engineering. *University of Rome, La Sapienza (Italy)*

Publications

A. Marinelli, E. Hemsing, J. B. Rosenzweig (2012) Three-Dimensional Analysis of Longitudinal Plasma Oscillations in a Thermal Relativistic Electron Beam: Application to an Initial Value Problem, *Phys. Plasmas* 19, 063108 (2012); URL: http://dx.doi.org/10.1063/1.4714639;

A. Marinelli, E. Hemsing, J. B. Rosenzweig (2011) Three-Dimensional Analysis of Longitudinal Plasma Oscillations in a Thermal Relativistic Electron Beam, *Phys. Plasmas* 18, 103105 (2011); URL: http://link.aip.org/link/doi/10.1063/1.3638139;

A. Marinelli, J. B. Rosenzweig (2010) Microscopic Kinetic Analysis of Space-Charge Induced Optical Microbunching in a Relativistic Electron Beam, *Phys. Rev. ST Accel. Beams*, 13, 110703 (2010);
URL: http://link.aps.org/doi/10.1103/PhysRevSTAB.13.110703;

A. Marinelli, C. Pellegrini, S. Reiche, L. Giannessi (2010) Comparative Study of Nonideal Beam Effects in High Gain Harmonic Generation and Self-Seeded Free Electron Lasers, *Phys. Rev. ST Accel. Beams*, 13, 070701 (2010) URL:http://link.aps.org/doi/10.1103/PhysRevSTAB.13.070701;

E. Hemsing, A. Marinelli, J. B. Rosenzweig (2011) Generating Optical Orbital Angular Momentum in a High-Gain Free-Electron Laser at the First Harmonic, *Phys. Rev. Lett.*, 106, 164803 (2011) URL: http://link.aps.org/doi/10.1103/PhysRevLett.1

P. Musumeci, R. K. Li, A. Marinelli (2011) Nonlinear Longitudinal Space Charge Oscillations in Relativistic Electron Beams, *Phys. Rev. Lett.*, 106, 184801 (2011) URL: http://link.aps.org/doi/10.1103/PhysRevLett.106.184801;

L. Giannessi et al. (2011) Self-Amplified Spontaneous Emission for a Single Pass Free-Electron Laser, *Phys. Rev. ST Accel. Beams*, 14, 060712 (2011) URL: http://link.aps.org/doi/10.1103/PhysRevSTAB.14.060712;

Y. Sakai, O. Williams, G. Andonian, A. Fukasawa, E. Hemsing, A. Marinelli, S. Barber, F. H. OShea, and J. B. Rosenzweig (2011) Harmonic Radiation of a Relativistic Nonlinear Inverse Compton Scattering Using Two Laser Wavelengths, *Phys. Rev. ST Accel. Beams*14, 120702 (2011) URL: http://link.aps.org/doi/10.1103/PhysRevSTAB.14.120702;

E. Hemsing, P. Musumeci, S. Reiche, R. Tikhoplav, A. Marinelli, J. B. Rosenzweig, and A. Gover (2011) Helical Electron-Beam Microbunching by Harmonic Coupling in a Helical Undulator, *Phys. Rev. Lett.*, 102, 174801 (2009) URL: http://link.aps.org/doi/10.1103/PhysRevLett.102.174801;

E. Hemsing, A. Marinelli, S. Reiche, and J. Rosenzweig (2008) Longitudinal Dispersion of Orbital Angular Momentum Modes in High-Gain Free-Electron Lasers, *Phys. Rev. ST Accel. Beams* 11, 070704 (2008)

URL: http://link.aps.org/doi/10.1103/PhysRevSTAB.11.070704;

A. Marinelli et al. (2012) Single Shot Coherent Diffraction Imaging of Microbunched Electron Beams for Free-Electron Laser Applications, Submitted to *Phys. Rev. Lett.* ;

A. Marinelli, E. Hemsing, P. Musumeci, J. B. Rosenzweig (2012) Using the Relativistic Two-Stream Instability for the Generation of Ultra-Short Radiation Pulses, Submitted to *Phys. Rev. Lett.*;

A. Marinelli, E. Hemsing, J. B. Rosenzweig (2012) Three-Dimensional Kinetic Theory of the Longitudinal Space-Charge Induced Microbunching Instability, To be submitted to *Phys. Rev. ST Accel. Beams*

CHAPTER 1

Introduction

1.1 The x-ray free-electron laser

Since their invention in the 1950s, lasers have risen to prominence as one of the fundamental tools for science and technology. The unique intensity and coherence properties of laser light, along with the great flexibility in temporal and spacial pulse shaping, have made lasers powerful instruments for science in a wide variety of fields, ranging from ultra-fast imaging to inertial fusion. Extending the spectral range of lasers to x-rays has long been a dream for scientists, since the wavelength associated to x-rays (on the Angstrom level) allows imaging at the characteristic spatial scale of atomic and molecular structures. However, applying the techniques of atomic lasers to x-rays has so far proven extremely difficult due to the challenges of generating a population inversion in the inner atomic shells associated with sub-nanometer wavelengths.

The generation of coherent x-rays has recently been achieved with free-electron lasers (FELs) [3]. The physics of free-electron lasers is different with respect to atomic lasers, in which coherent radiation is emitted and amplified due to the population inversion of discrete energy levels in a medium. Instead, in an FEL, the coherent radiation is emitted by relativistic electrons traveling in a periodic magnetic field and undergoing an unstable interaction process with the radiation itself. Despite the radically different physics associated with the generation of photons, the radiation pulses generated by an FEL share the same properties as conventional lasers, i.e. transverse coherence, high peak power (on the order of 10 GW), short pulse duration (on the order of 10 fsec) and narrow bandwidth (typically $\Delta\lambda/\lambda \simeq 10^{-4}$ to 10^{-3}).

Compared to other sources of x-rays for scientific research, most prominently synchrotrons, the x-ray FEL has a larger peak brilliance by 10 orders of magnitude, representing a ground-breaking advance for x-ray science. The high peak brightness of x-ray FEL pulses, combined with their short duration, allows single-shot coherent diffraction-imaging down to the Angstrom level, and enables an entirely new set of revolutionary imaging experiments. In practice, the x-ray FEL allows the imaging of samples that are either too sensitive to radiation damage (thanks to the short pulse duration that allows collection of a diffraction pattern before the sample is destroyed) or that are impossible to be grown into large crystals (thanks to the high peak power that allows the single-shot imaging of nano-crystals flowing in a gas-jet [2], see Fig. 1.1). Recent experiments at the LCLS include the imaging of protein nano-crystals and viruses [1] (see Fig. 1.1). Furthermore, the short pulse duration will allow future time-resolved investigation of atomic processes down to the femtosecond level, i.e. on the characteristic time-scale of the electron orbit around the nucleus. Other applications of the FEL are the study of matter at high energy density [5] and atomic physics [6]. A review of the physics and history of x-ray FELs can be found in Ref. [7]

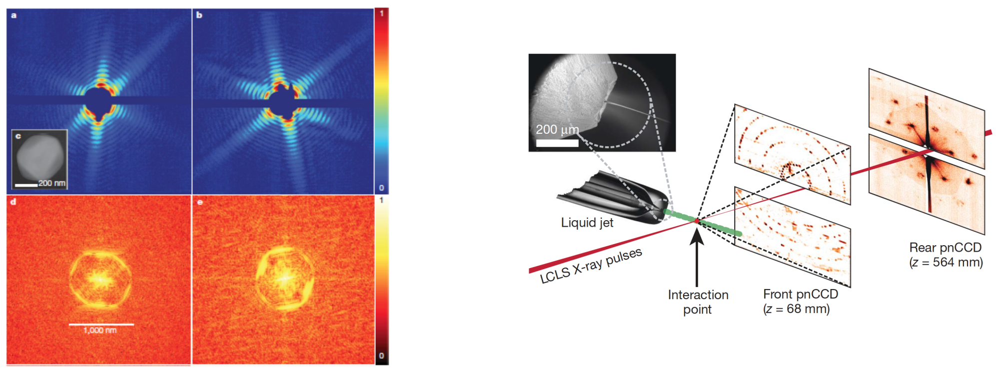

Figure 1.1: Image of the mimivirus reconstructed from an x-ray diffraction pattern at the LCLS [1] (left image) and injection scheme for nanocrystalline samples for single-shot imaging at x-ray FEL facilities [2].

1.2 High Brightness Relativistic Electron Beams for Free-Electron Laser Applications

Relativistic electron beams play an increasingly important role in science. In advanced applications such as high gain free-electron lasers, plasma wakefield accelerators or linear particle colliders the brightness of the beam, defined as the density in six-dimensional phase-space, is a key feature.

Some examples of high-brightness electron beam facilities are the the Linac Coherent Light Source electron injector at the Stanford Linear Accelerator Center (see e.g.[3]) or the Pegasus Laboratory of the University of California, Los Angeles (see [8]). In these facilities, a high intensity laser excites a photo-cathode generating an intense electron bunch which is then accelerated to relativistic energies by a series of radio-frequency cavities. The high-density in phase-space can be converted into high volume density by longitudinal compression and strong transverse focusing, thus enabling applications that require the excitation of intense electro-magnetic fields. An extensive review on the physics of high brightness injectors can be found in

This dissertation is mainly devoted to the study of instabilities in free-electron laser drive beams. To understand the connection of our work with x-ray free-electron lasers we give a brief introduction to the physics of free-electron lasers. In a free-electron laser, an intense relativistic electron beam propagates in a periodic system of permanent magnets called an undulator. The undulator excites a transverse oscillating motion which causes the beam to emit radiation. The interaction between the beam itself and the collective radiation field generated by the electrons gives rise to an unstable response, with an exponential growth of the field intensity as a function of time.

The period of the undulator is typically a few centimeters long but the emitted radiation is doppler-shifted by the relativistic electrons, with a resulting radiation wavelength of :

$$\lambda_r = \lambda_w \frac{1+K^2}{2\gamma^2} \tag{1.1}$$

where γ is the beam energy in units of mc^2 and $K = \frac{eB_0}{mck_w}$ is the undulator parameter, with e and m being respectively the electron charge and mass, B_0 the peak undulator field and $k_w = 2\pi/\lambda_w$ being the undulator wave-number. The scaling of the radiation wavelength with energy ($\propto 1/\gamma^2$) makes the free-electron laser an attractive option for the generation of coherent x-ray pulses.

The radiation power at the emission wavelength λ_r grows exponentially as a function of time as [9]:

$$P = P_0 e^{ct/L_g} \tag{1.2}$$

where the FEL power gain-length is given by $L_g = \lambda_w/2\sqrt{3}\pi\rho$, with the Pierce parameter being defined as: $\rho = (K\omega_p/4ck_w)^{2/3}$. The beam plasma frequency is

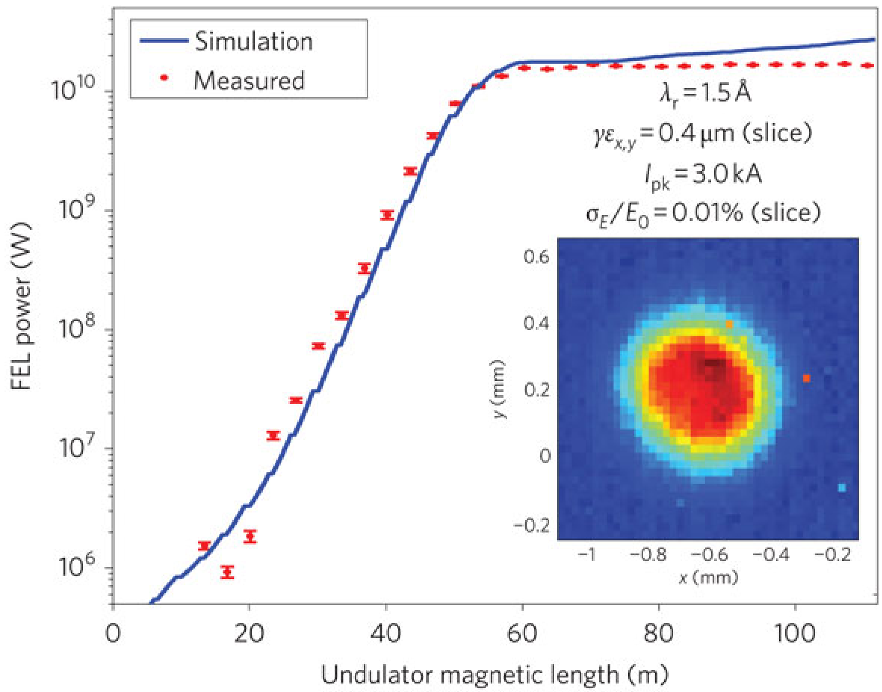

Figure 1.2: Radiation Power for the Linac Coherent Light Source as a function of the position in the undulator [3].

given by $\omega_p = \sqrt{n_0 e^2/m\gamma^3\epsilon_0}$, with n_0 being the beam volume density. Typical values for the Pierce parameters in operating FEL facilities are on the order of $\rho \simeq 10^{-4}/10^{-3}$.

Note that the FEL gain-length scales proportionally to $\gamma/n_0^{1/3}$, which means that high beam density (thus high beam brighness) is required for efficient FEL operation (i.e short gain-length) at high beam energy.

In addition to the high density, the electron beam needs to satisfy other requirements on the energy-spread and transverse emittance. The FEL physical process is based on a resonant interaction between electrons and radiation in which the velocity of the electrons is matched to the radiation frequency so that the radiation slips forward with respect to the particles by one radiation wavelength per undulator period. For an efficient FEL interaction, all the electrons have to be close to the resonant velocity to guarantee the velocity spread in the beam does not disrupt the resonant interaction.

Energy-spread and transverse emittance generate a longitudinal velocity-spread that can compromise the FEL process. From the kinetic theory of free-electron laser it can be shown that the requirements on the beam quality are given by (see e.g. Ref [10]):

$$\sigma_\gamma/\gamma \ll \rho \tag{1.3}$$

and:

$$k_r \epsilon L_g/\beta_f \ll 1. \tag{1.4}$$

where σ_γ is the energy spread of the particles in units of mc^2, ϵ is the transverse emittance, defined as the beam density in transverse phase-space, $k_r = 2\pi/\lambda_r$ and β_f being the beta-function of the electron beam.

From the above scaling laws it follows that high density, low emittance and low energy-spread (i.e. high brightness) are critical features for free-electron laser operation at short wavelengths. The generation and transport of high-quality electron beams is key in the successful operation of x-ray FELs.

1.3 The Microbunching Instability and the Longitudinal Space-Charge Amplifier

Due to their high brightness (and thus high-density) the electron beams that drive the FEL instability undergo a number of collective instabilities that can parasitically amplify shot-noise and generate an undesired density modulation (or microbunching) in the electron beam [11]. These instabilities can degrade the performance of the FEL and cause the emission of coherent radiation in diagnostic stations, making the imaging and diagnostics of high-brightness electron beams extremely challenging. This type of process is usually referred to as microbunching instability and it is caused by the coupling of collective interactions, like space-charge or coherent synchrotron radiation, to longitudinal motion in dispersive systems (for example, magnetic chicanes). The microbunching instability has been the subject of intense research in the past few years and it represents the main subject of this dissertation. The mitigation and control of this instability has proven to be a critical issue in the operation of x-ray free-electron laser [12]. Furthermore, the understanding of the collective effects associated with this instability has led to new important concepts, such as the longitudinal space-charge amplifier [13] and the suppression of shot-noise in FEL beams [14, 15, 16].

The longitudinal space-charge amplifier (LSCA) has recently been proposed to extend the capability of x-ray FEL facilities to generate broad-band coherent radiation pulses [13]. In fact, while the narrow-bandwidth is generally regarded as an attractive feature of the FEL, it ultimately limits the capability of FELs to generate ultra-short radiation pulses with duration below the cooperation length.

The LSCA exploits the longitudinal space-charge induced microbunching instability to generate and amplify strong density perturbations in the electron beam at short wavelengths. The instability is caused by the longitudinal space-charge interaction coupled to longitudinal motion in magnetic chicanes. While the microbunching instability is generally regarded as a detrimental effect, in an LSCA this process is optimized and controlled to induce the emission of coherent radiation in a downstream undulator. To achieve saturation , several amplification stages are cascaded, each composed of a focusing channel and a magnetic chicane (see Fig. 1.3).

(H)

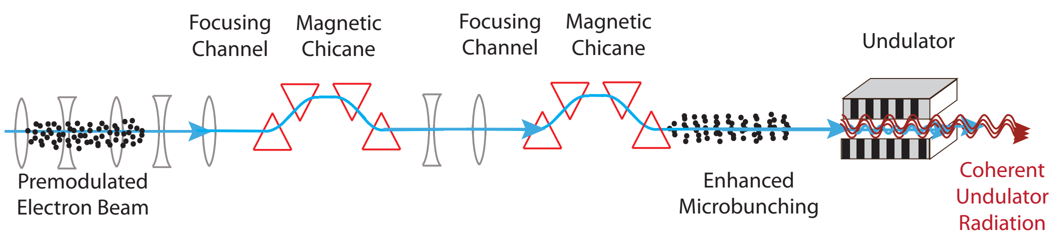

Figure 1.3: Schematics of a longitudinal space-charge amplifier: longitudinal space-charge, in combination with dispersive transport in magnetic chicanes, amplifies microbunching in the electron beam. The microbunched electron beam emits coherent radiation in a downstream undulator.

Since the longitudinal space-charge instability is a broad-band effect (i.e. it amplifies microbunching on a broad range of wavelengths), the coherent emission can happen on a broad spectral bandwidth, depending on the emission characteristics of the undulator. For typical high-brightness beam parameters, an LSCA can emit coherent radiation with power comparable to an FEL operating at the same central wavelength, with a bandwidth of $\Delta\lambda/\lambda \simeq 20\%$ 30%. This feature enables the generation of few-optical cycle radiation pulses, ranging down to the atto-second level [17]. Note that the recent ground-breaking development of few-optical cycle coherent radiation pulses [18], enables the generation of soft x-ray attosecond pulses with an LSCA either with direct seeding at 30 nm or with laser compression of electron beams in an enhanced-SASE configuration [19]. Note also that under certain optimized conditions (which will be discussed later in this dissertation), an LSCA seeded from shot-noise can generate transversely coherent radiation pulses, a property shared with the FEL.

In addition to its unique spectral properties, the LSCA is more robust than the FEL to non-ideal beam conditions and it has been proposed as an effective way to generate coherent radiation with advanced particle accelerators such as laser-wakefield and plasma-wakefield accelerators, which haven't met the beam quality requirements for FEL operation [13].

1.4 Outline and Scope of this Dissertation

The main subject of this dissertation is the collective evolution of beam microbunching and the coherent diagnostics of microbunching in high-brightness electron beams.

While the theory of longitudinal space-charge interactions has been the subject of intense research in the FEL community [20, 21, 22, 23], a fully self-consistent theory had yet to be developed, leaving the role of emittance and energy-spread in the physics of the space-charge instability unexplained. Since the control of space-charge effects has a number of important applications for the improvement of x-ray free-electron lasers, this subject needed a more rigorous theoretical foundation. For this reason we give, for the first time, a fully kinetic and self-consistent description of this process in six-dimensional phase-space. This analysis enables the study of transverse and longitudinal thermal effects, which strongly influence the formation of microbunching. In particular, *transverse* thermal effects influence the spatial distribution of the microbunching generated from shot-noise. This, in turn, determines the transverse coherence properties of a LSCA and affects the diagnostics of electron bunches with coherent transition radiation. *Longitudinal* thermal effects can suppress the gain at short wavelengths, thus limiting the operation of an LSCA in the VUV/soft x-ray spectral region. This theoretical model gives deep insight into the physics of longitudinal space-charge effects and represents a useful tool for the optimization of space-charge based experiments, such as the LSCA and the shot-noise suppression schemes proposed by Gover [14] and Ratner [15].

In addition to a fully consistent theory, the LSCA was also missing an experimental confirmation. In fact, while coherent radiation induced by the microbunching instability had been previously observed at several FEL injectors [24, 25, 26, 27], the optimization and control of the instability for the generation of transversely coherent radiation pulses had not been demonstrated experimentally. For this reason, we performed a proof of principle demonstration of this scheme at the NLCTA test accelerator at SLAC. We turned the three-chicane setup of the ECHO experiment into a cascaded space-charge amplifier and demonstrated the generation of single-mode coherent undulator radiation from the space-charge instability. This experiment paves the way for the generation of broad-band coherent radiation at FEL user facilities and represents a significant advancement in the fields of high-brightness beams and coherent light sources.

The last subject tackled in this dissertation is the coherent diagnostics of beam microbunching. We designed and experimentally demonstrated a technique for reconstruction of the spatial distribution of beam microbunching. This experiment is the first of its kind. In fact, all previous work on the subject was primarily focused on the characterization of the coherent radiation emitted by microbunched electron beams rather than the structural determination of the microbunching from the coherent radiation itself. We performed a seeded coherent transition radiation experiment at the NLCTA using the ECHO seeding beamline and used an oversampling phase-retrieval technique for the reconstruction of the laser induced microbunching. This type of technique has several applications as an advanced diagnostics for FELs and for the imaging of compressed electron beams that are affected by the microbunching instability.

The following is a detailed outline of this dissertation. In the next chapter we discuss the basic mathematical tools for the description of collective effects and coherent radiation process in relativistic electron beams. From the simple introductory analysis of the space-charge instability discussed in chapter 2, it will be clear that this type of collective process is strictly related to the physics of relativistic longitudinal plasma oscillations. With this idea in mind, in chapters 3 and 4 we develop a fully kinetic model of the evolution of space-charge waves in a relativistic electron beam. In particular, in chapter 3 we describe the theory of space-charge waves in the context of an eigenvalue-eigenmode problem. In this approach we construct a set of self-consistent solutions to the system of Vlasov-Poisson equations in the form of propagating longitudinal space-charge waves. Our analysis includes the effects of longitudinal thermal motion induced by energy-spread and transverse emittance, transverse motion due to betatron focusing, and three-dimensional effects due to the finite transverse size of the electron beam.

The plasma eigenmodes of the beam are used in chapter 4 as an expansion basis for an arbitrary initial perturbation in six-dimensional phase-space. The mode decomposition of the initial perturbation is performed by exploiting the bi-orthogonality property of the plasma eigemodes and their set of adjoint eigenmodes. The bi-orthogonal mode expansion of the initial value represents the solution to an initial value problem and describes the evolution of an arbitrary initial perturbation in six-dimensional phase-space under the effect of longitudinal space-charge forces.

The mathematical formalism developed in chapters 3 and 4 is employed in chapter 5 to give a fully kinetic description of the microbunching instability induced by longitudinal space-charge forces. This analysis allows the study of new phenomena, such as the effect of the emittance-induced Landau damping on the microbunching amplification process and the suppression of higher-order modes induced by transverse focusing.

The modal analysis derived in the first three chapters is impractical in the case of a fully degenerate beam (i.e. a transversely laminar beam with a radius that is significantly larger than the microbunching wavelength as seen in the rest frame). In this case a great number of eigenmodes should be included to correctly describe the space-charge fields of the beam. To address this problem, in chapter 6 we derive a quasi three-dimensional theory of the space-charge induced microbunching instability. In this approach the electron beam is approximated as an unmagnetized relativistic uniform plasma and the evolution of microbunching is described in terms of plane-waves.

In chapter 7 we apply the theoretical concepts developed in the first part of the dissertation to a space-charge amplification experiment. We report the first experimental demonstration of the longitudinal space-charge amplifier at the NLCTA. The experiment demonstrates cascaded amplification of microbunching through three LSCA stages starting from shot-noise, and the subsequent emission of transversely and longitudinally coherent radiation in a magnetic undulator.

In chapter 8 we describe an advanced diagnostic technique for the reconstruction of the transverse dependence of beam microbunching and report on its experimental demonstration at the NLCTA. We give a brief description of the oversampling phase-retrieval method and describe its application to the reconstruction of beam microbunching from the far-field pattern of coherent optical transition radiation. Finally, we show experimental results which confirm the use of this technique as an advanced imaging method for microbunched electron beams.

The last chapter summarizes the most relevant findings, puts them in context and suggests future research directions.

CHAPTER 2

Introduction to the Collective Theory of Beams and Coherent Radiation Processes

In this chapter we discuss the basic mathematical tools for the description of collective beam dynamics in phase-space. We will refer to this subject as the kinetic theory of particle beams. Starting from the Klimontovich equation, we will derive the Vlasov equation and discuss its coupling to the equations that describe the collective electromagnetic fields. We will then show the application of these concepts to the simple case of the microbunching instability in the one-dimensional limit. Finally, in the last section we briefly discuss coherent radiation processes from relativistic electrons and their connection to beam microbunching.

2.1 The Klimontovich Equation

A relativistic particle beam is a collection of interacting point-like masses. A collection of N particles in six-dimensional phase-space can be modeled by the Klimontovich distribution:

$$K(\vec{X},t) = \sum_{n} \delta\left(\vec{X} - \vec{X}_n(t)\right), \tag{2.1}$$

where $\vec{X}_n(t) = (\vec{x}_n(t), \vec{p}_n(t))$ is the vector representing the six-dimensional phase-space coordinate of the n_{th} particle. K can be interpreted as a beam density distribution in phase-space, i.e. the quantity $dN = K(\vec{X}, t) d^6\vec{X}$ is the number of particles contained in the infinitesimal phase-space volume $d^6\vec{X}$ at the time t.

By using the simple relationship $\partial_t f\,(x - a(t)) = -\dot{a}\partial_x f\,(x - a(t))$ we obtain that:

$$\partial_t K + \dot{\vec{x}}\partial_{\vec{x}} K + \dot{\vec{p}}\partial_{\vec{p}} K = 0, \tag{2.2}$$

where $\dot{\vec{x}}$ and $\dot{\vec{p}}$ are evaluated at the phase-space position $(\vec{x}, \vec{p})$ using the equations of motion of the system. For example, if $(\vec{x}, \vec{p})$ are a set of canonical variables, then the equations of motion can be derived by a Hamiltonian

$$\dot{\vec{x}} = \nabla_{\vec{p}} H(\vec{x}, \vec{p}) \tag{2.3}$$

$$\dot{\vec{p}} = -\nabla_{\vec{x}} H(\vec{x}, \vec{p}). \tag{2.4}$$

In general, it is not required that the phase-space coordinates be a set of canonical variables, as long as the time derivative of the phase-space vector is a direct function of the phase-space position, i.e. $\dot{\vec{x}} = \vec{D}_x(\vec{x}, \vec{p}), \dot{\vec{p}} = \vec{D}_p(\vec{x}, \vec{p})$. In fact, in this dissertation we will often use the following phase-space vector $(\vec{x}, \vec{\beta}_\perp, \gamma)$, where $\vec{x}$ is the position vector, $\vec{\beta}_\perp$ is the transverse velocity normalized to the speed of light and γ is the kinetic energy in units of mc^2. These are not a set of canonical variables, nevertheless the Klimontovich equation, as well as the Vlasov and Boltzmann equations that follow from it, still apply.

2.2 The ensemble average of the Klimontovich equation: the Boltzmann and Vlasov equations

The Klimontovich equation is of little practical value, since its solution is equivalent to the solution of the coupled equations of motion for each of the N particles in the beam (i.e. $6N$ coupled differential equations!). In fact, despite the apparent simplicity of Eq. 2.4, the term $\dot{\vec{p}}$ contains the contribution to the local force from each of the N particles in the beam, in addition to any externally applied force. A complete solution to this problem is not only impossible to pursue analytically (although it could be done numerically with highly parallelized particle tracking codes) but also of little help in understanding the underlying physics. In this dissertation we are concerned with certain averaged quantities, which can be derived from the statistically averaged particle distribution function.

Consider the initial value of the Klimontovich distribution $K_0 = K(\vec{X}, 0)$ to be randomly distributed according to a given distribution function $f_{t=0}$, i.e. the ensemble averaged number of particles in an elementary phase-space volume be such that $< dN >=< K(\vec{X}, 0)d^6\vec{X} >= f_{t=0}d^6\vec{X}$. We are interested in deriving an evolution equation for the statistically averaged distribution function $f(\vec{X}, t) =< K(\vec{X}, t) >$ at times $t > 0$. To do so, we give the following definitions:

$$K = f + \delta f \tag{2.5}$$

$$\dot{\vec{p}} =< \dot{\vec{p}} > +\delta\dot{\vec{p}}, \tag{2.6}$$

where $<>$ indicates the ensemble average, i.e. an average over all possible realizations of the initial distribution with the prescription that $< K(\vec{X}, 0)d^6\vec{X} >= f_{t=0}d^6\vec{X}$. By definition, the ensemble averages of the fluctuating terms vanish, i.e. $< \delta f >= 0$ and $< \delta\dot{\vec{p}} >= 0$. However, the cross-term $< \delta f \delta\dot{\vec{p}} >$ is, in general, non vanishing. Note also that there is no fluctuation of the $\dot{\vec{x}}$ term since the instantaneous velocity of a particle is only dependent on its position in phase-space (i.e. at any given time, the particle velocity does not depend on the position of the other particles, as opposed to the force, which is determined by the interaction with all the particles in the ensemble). By substituting the definitions in Eq. 2.6

into Eq.2.2, we obtain the following result:

$$\dot{f} + \dot{\vec{x}}\partial_{\vec{x}}f + <\dot{\vec{p}}> \partial_{\vec{p}}f = - <\delta\dot{\vec{p}}\partial_{\vec{p}}\delta f> . \tag{2.7}$$

This is the Boltzmann equation, and represents the evolution equation for a collisional collection of particles. The term on right-hand side of the equation is conventionally referred to as the collision operator and accounts for the change in the distribution function due to particle to particle collisions, whereas the $<\dot{\vec{p}}>$ term contains the contribution coming from the collective forces of the beam and any externally applied force. Leaving aside the discussion on the collision operator, which is not of direct interest in this dissertation, we now focus on the case in which collisions are negligible. In the limit of a collision-less ensemble of particles, we can neglect the right-hand side of Eq. 2.7 and we obtain the Vlasov equation:

$$\dot{f} + \dot{\vec{x}}\partial_{\vec{x}}f + <\dot{\vec{p}}> \partial_{\vec{p}}f = 0. \tag{2.8}$$

The Vlasov equation (as well as the Klimontovich equation), is formally equivalent to the evolution equation of an incompressible fluid in phase-space. Note that from the Vlasov, not only it follows that the particles are conserved, which would be expressed by a more general continuity equation of the type:

$$\partial_t f + \nabla_{\vec{X}}(\dot{\vec{X}}f) \tag{2.9}$$

but also that the phase-space distribution function computed along a particle trajectory is constant. This can be understood by noting that the left-hand side of the equation contains the total time derivative of the distribution function along the particle trajectories $df/dt|_{traj.} = 0$. One consequence of this is that, given the initial distribution function $f(\vec{X}, t = 0)$, the distribution function at any given time is given by $f(\vec{X}_0(\vec{X},t), t=0)$, where $\vec{X}_0(\vec{X},t)$ is an operator that reverts the trajectory of a particle in $\vec{X}$ at the time t to its starting phase-space position. To clarify this point, let's consider a set of relativistic non-interacting particles traveling in a uniform focusing channel. We choose the following phase-space variables: $\vec{X} = (\vec{x}_\perp, z, \vec{v}_\perp, v_z)$, where $\vec{x}_\perp, z$ are the spatial coordinates and $\vec{v}_\perp, v_z$ are the transverse and longitudinal velocity. The equations of motion of the particles are:

$$\dot{\vec{x}}_\perp = \vec{v}_\perp \tag{2.10}$$

$$\dot{\vec{v}}_\perp = -\omega_\beta^2 \vec{x}_\perp \tag{2.11}$$

$$\dot{z} = v_z \tag{2.12}$$

$$\dot{v}_z = 0, \tag{2.13}$$

where ω_β is the oscillation frequency of the focusing channel[1]. The Vlasov equation for this system reads:

$$\dot{f} + \dot{\vec{x}}_\perp \partial_{\vec{x}_\perp} f + v_z \partial_z f - \omega_\beta^2 \vec{x}_\perp \partial_{\vec{v}_\perp} f = 0. \tag{2.14}$$

The particle trajectories are given by:

$$\vec{x}_\perp = \vec{x}_{\perp,0} \cos\omega_\beta t + \tfrac{\vec{v}_{\perp,0}}{\omega_\beta} \sin\omega_\beta t \tag{2.15}$$

$$\vec{v}_\perp = \vec{v}_{\perp,0} \cos\omega_\beta t - \omega_\beta \vec{x}_{\perp,0} \sin\omega_\beta t \tag{2.16}$$

$$z = z_0 + v_{z,0} t \tag{2.17}$$

$$v_z = v_{z,0}, \tag{2.18}$$

[1]Note that Eq.2.13 is only true when averaged over an oscillation period. This approximation is reasonable for highly directional particles in which the transverse momentum is much smaller than the longitudinal one, as is the case of interest for relativistic particle beams.

which can be easily inverted as:

$$\vec{x}_{\perp,0} = \vec{x}_\perp \cos\omega_\beta t - \tfrac{\vec{v}_\perp}{\omega_\beta} \sin\omega_\beta t \tag{2.19}$$

$$\vec{v}_{\perp,0} = \vec{v}_\perp \cos\omega_\beta t + \omega_\beta \vec{x}_\perp \sin\omega_\beta t \tag{2.20}$$

$$z_0 = z - v_z t \tag{2.21}$$

$$v_{z,0} = v_z. \tag{2.22}$$

If the initial distribution function is given by $f(\vec{X},0) = g(x_{\perp,0}, z_0, \beta_{\perp,0}, v_{z,0})$, then the distribution function at any given time is given by:

$$f(\vec{X},t) = g(\vec{x}_\perp \cos\omega_\beta t - \frac{\vec{v}_\perp}{\omega_\beta} \sin\omega_\beta t, z - v_z t, \vec{v}_\perp \cos\omega_\beta t + \omega_\beta \vec{v}_\perp \sin\omega_\beta t, v_z), \tag{2.23}$$

which can be easily verified by direct substitution of this solution into Eq. 2.14

Note also that, in general, if the system has some constants of the motion, any distribution function that only depends on any of these constants is stationary. For example, in the case we have just discussed, any function of the two quantities $\omega_\beta^2 \vec{x}_\perp^2 + \vec{v}_\perp^2$, v_z is a stationary distribution.

For systems of interacting particles, the explicit inversion of the equations of motion for each single particle is, in general, not possible. In this case the Vlasov equation has to be solved directly, coupled to the equations that describe the the collective interaction. We use the phase-space vector $(\vec{x}, \vec{p})$, where $\vec{x}$ is the position vector and $\vec{p} = \gamma m \vec{v}$ is the mechanical momentum vector, where $\gamma = 1/\sqrt{1 - \vec{v}^2/c^2}$ is the Lorentz factor, m is the particle mass and c is the speed of light. The Vlasov equation, is given by:

$$\dot{f} + \dot{\vec{x}} \partial_{\vec{x}} f + (\vec{F}_{ext} + \vec{F}_{coll}) \partial_{\vec{p}} f = 0, \tag{2.24}$$

where $\vec{F}_{ext}$ is an externally applied force and the collective force $\vec{F}_{coll} = e(\vec{E} + \vec{v} \times \vec{B})$ is given by computing the ensemble averaged electric and magnetic fields generated by the particles. Note that in the case of electromagnetic interactions, since the Maxwell equations are linear, the collective part of $< \dot{\vec{p}} >$ can be obtained by computing the electromagnetic fields generated by the average charge distribution $\rho = q \int f d^3\vec{p}$ and by the average current distribution $\vec{j} = q \int \vec{v} f d^3\vec{p}$, where $\vec{v} = \vec{p}c/\sqrt{m^2c^2 + \vec{p}^2}$ gives the velocity of the particles in terms of the phase-space momentum coordinates $\vec{p}$ and q is the particle charge. The resulting equations are:

$$\vec{\nabla} \cdot \vec{E} = \epsilon_0 q \int f d^3\vec{p} \tag{2.25}$$

$$\vec{\nabla} \times \vec{E} = -\partial_t B \tag{2.26}$$

$$\vec{\nabla} \cdot \vec{B} = 0 \tag{2.27}$$

$$\vec{\nabla} \times \vec{B} = \mu_0 q \int \vec{v}(\vec{p}) f d^3\vec{p} + \frac{1}{c^2}\partial_t \vec{E}, \tag{2.28}$$

where ϵ_0 and μ_0 are, respectively, the vacuum permittivity and the vacuum magnetic permeability. Equations 2.24 and 2.28, represent a system of non-linear coupled partial differential equations which cannot be solved analytically, in general. These equations are generally termed the Vlasov-Maxwell system. This set of equations fully describes the collective evolution of a set of interacting particles, such as an intense relativistic electron beam. In the remainder of the dissertation we will discuss the applications of the collective theory of beams that we have introduced here as applied to the physics of longitudinal space-charge interaction and the collective evolution of beam microbunching.

2.3 Beam Microbunching

A periodic density perturbation in a particle beam is denominated beam microbunching. The beam microbunching is described by the so-called bunching factor, defined as the Fourier transform of the beam's longitudinal profile normalized to the number of particles:

$$b = \frac{1}{N} \sum_n e^{-ikz_n} \tag{2.29}$$

where N is the number of particles in the beam and z_n is the longitudinal position of the n_{th} particle in the beam. The bunching factor is minimum and equal to $b = 0$ if the electrons are uniformly distributed along the z-axis and it is maximum and equal to $b = 1$ if the electrons are periodically distributed in packets much smaller than the wavelength $\lambda = 2\pi/k$ and separated by a wavelength. Figure 2.1 shows three examples of beams with a finite microbunching.

Note that if the particles are randomly distributed in z, the density has random fluctuations that are normally identified as shot-noise fluctuations. Shot-noise generates a random bunching factor that has a zero statistical average but a finite root-mean square value. This can be seen by noting that the phase-factor associated with each electron $e^{-ik_z z_n}$ averages out to zero if the position of the electron is a stochastic variable with a uniform distribution. The absolute value squared of the bunching factor, instead, can be expressed as:

$$|b|^2 = \frac{1}{N^2} \sum_{n,m} e^{-ik(z_n - z_m)} = \frac{1}{N} + \frac{1}{N^2} \sum_{n \neq m} e^{-ik(z_n - z_m)}. \tag{2.30}$$

The second term in equation 2.30 averages to zero, leaving a finite value for the average shot-noise power of $\overline{|b|^2} = \frac{1}{N}$.

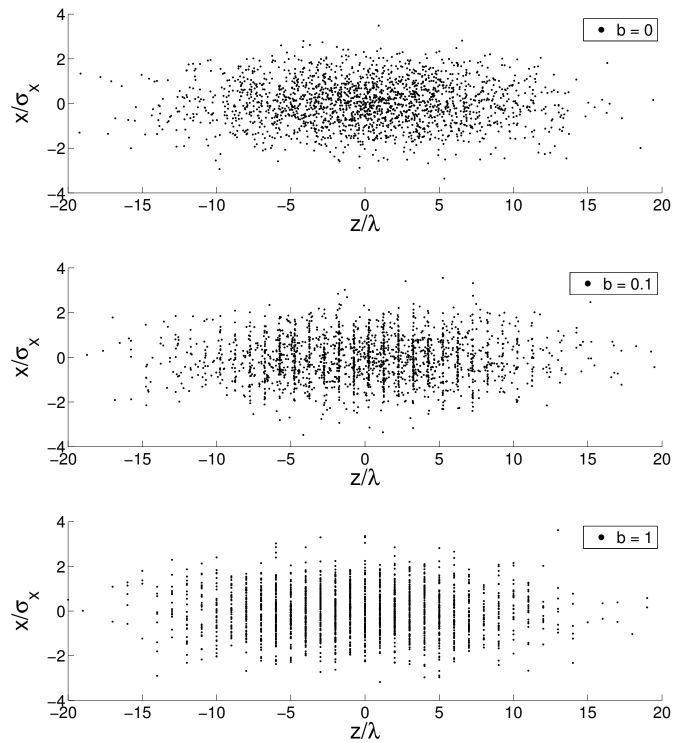

Figure 2.1: Examples of beams with finite different values of the bunching factor: b = 0 (top figure), b= 0.1 (middle figure) and b=1 (bottom figure).

Beam microbunching is a key feature in the emission of radiation from electron beams. To understand the role of microbunching in cooperative emission processes we examine a simplified scenario in which each electron emits a plane wave of the form: $E_n = Ee^{i(k(z-z_n)-\omega t)}$. The field emitted by the entire electron bunch is then given by the superposition of the fields from each individual electron:

$$E_b = \sum_n Ee^{i(k(z-z_n)-\omega t)} = NbEe^{i(kz-\omega t)} \tag{2.31}$$

It follows that the emitted radiation power is proportional to $P \propto |b|^2 N^2$. If the beam has a finite density modulation, the radiated power is proportional to the number of particles squared. Such radiative process is denominated cooperative emission or coherent emission. If the beam microbunching is only due to shot-noise, then the radiation power scales proportionally to the number of particles and the emission process is defined as spontaneous emission. This is a general property of radiation emitted from relativistic electrons that holds for any type of emission process like transition radiation or undulator radiation. This point will be discussed more rigorously later in this chapter.

Beam microbunching can be generated by inducing an energy modulation in the particle beam and let the particles travel through a beamline element with a finite longitudinal dispersion, like for example, a magnetic chicane. To understand this consider a beam with a Gaussian energy spread and a uniform volume density, which can be described by the following longitudinal phase-space distribution: $f(z_0, \eta_0) = n_\lambda \frac{e^{-\frac{\eta_0^2}{2\sigma_\eta^2}}}{\sqrt{2\pi}\sigma_\eta}$. If we introduce an energy modulation the longitudinal phase-space coordinates become:

$$z' = z_0 \tag{2.32}$$
$$\eta' = \Delta \sin(k_z z_0) + \eta_0.$$

The effect of longitudinal dispersion can be modeled with the following coordinate transformation $z'' \to z' + R_{56}\eta'$. Figure 2.2 shows the scheme of a magnetic chicane. Four dipole magnets bend the electrons on an off-axis trajectory, whose length is dependent on the particle energy. For a simple four dipole chicane we have $R_{56} = \frac{2}{3}L_{mag}\theta^2 + 2L_d\theta^2$, where θ is the bending angle, L_{mag} is the length of the dipole magnets and L_d is the separation length between the first and second magnet and the third and fourth ones.

The bunching factor after the magnetic chicane is given by:

$$b(k) = \int dz_0 d\eta_0 f(z_0, \eta_0) e^{-ik(z_0 + R_{56}(\eta_0 + \Delta \sin(k_z z_0)))}. \tag{2.33}$$

The z-integral selects the harmonics of the energy modulation, giving a discrete microbunching spectrum at the harmonics of k_z:

$$b(nk_z) = J_n(nk_z R_{56}\Delta) e^{-\frac{(nk_z \sigma_\eta R_{56})^2}{2}}, \tag{2.34}$$

where J_n is the n_{th} order Bessel function of the first kind.

Figure 2.3 shows the longitudinal phase-space and the x-z trace space for a beam with an energy modulation $\Delta = 4 \times 10^{-4}$ and a relative energy-spread of $\sigma_\eta = 1 \times 10^{-4}$ for several values of the longitudinal dispersion R_{56}. Note that the microbunching is maximized when the longitudinal phase-space is vertical (third

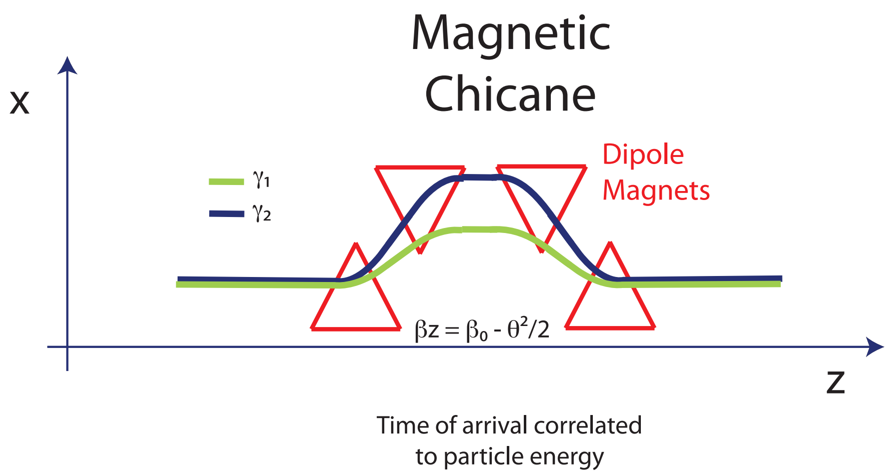

Figure 2.2: Schematics of a magnetic chicane. The bending angle is correlated to energy, introducing a correlation between the time of arrival and particle energy.

case in Fig.2.3) and it diminishes for bigger values of R_{56} due to the overbunching of the particles. Note that for small values of the longitudinal dispersion we have $b_1 \simeq \frac{1}{2} k_z R_{56} \Delta e^{-\frac{(nk_z \sigma_\eta R_{56})^2}{2}}$ and the bunching factor is proportional to the amplitude of the density modulation. We refer to the latter case as linear microbunching regime.

2.4 The Microbunching Instability

In the previous section we have defined the concept of beam microbunching and discussed how a density modulation can arise from an energy modulation combined with the effect of longitudinal dispersion. This mechanism is general and independent of the type of physical effect that generates the energy modulation. An energy modulation in the electron beam, could be generated by a great number of physical effects, such as the interaction of the electrons with a laser pulse in a magnetic undulator or by collective beam interactions. The topic of interest for

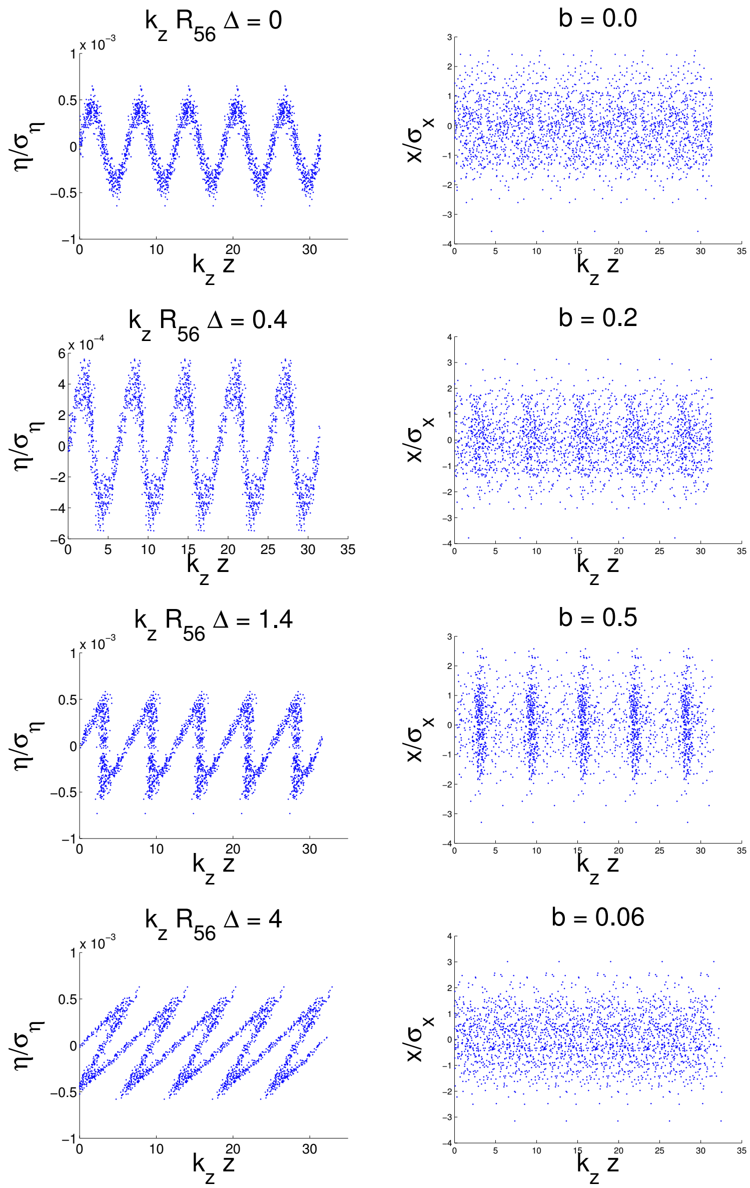

Figure 2.3: Longitudinal phase-space (left column) and x-z trace space (right column) for a beam with an energy modulation for different values of the longitudinal dispersion R_{56}.

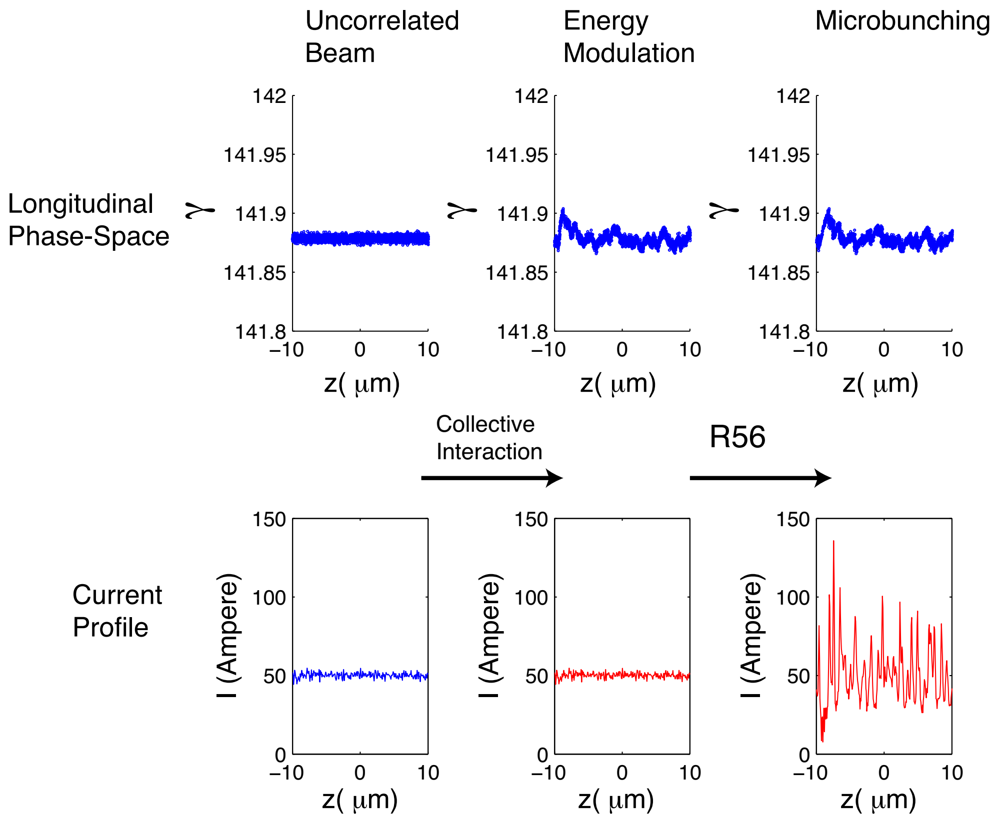

Figure 2.4: Example of a microbunching instability process. An electron beam with randomly distributed electrons develops a broadband energy modulation as a consequence of collective interactions. Longitudinal dispersion transforms the energy modulation into microbunching.

this dissertation is the microbunching instability, in which the energy modulation that generates the microbunching, is induced by collective fields [11].

The mechanism of the microbunching instability can be explained as follows: a beam with a finite microbunching at some spatial frequency k excites a collective electro-magnetic field (like, for example, a periodic Coulomb field or an electromagnetic wave). The interaction of the electrons in the beam with the collective fields, in turn, generates an energy modulation at the frequency k. The longitudinal dispersion induced by certain systems of permanent magnets (typically a magnetic chicane) transforms the induced energy modulation into density modulation, generating a bunching factor higher than the starting value[2]. This instability can start up from noise (which has a white microbunching spectrum) and generate beams with significant perturbations to the density and energy profiles. Figure 2.4 shows a schematic of this process, in which a beam with a pure random longitudinal distribution develops a density modulation as a consequence of the collective longitudinal space-charge interaction followed by a finite R_{56}. In general, systems with significant longitudinal dispersion, like magnetic chicanes, are used in cases in which strong beam compression is needed to enhance the beam current. This is particularly true for x-ray free-electron laser injectors, in which one or two magnetic compression devices are typically employed to generate a high-density beam for an efficient FEL process. In this case, the shot-noise enhancement due to the microbunching instability can pose serious limitations to the beam quality and needs to be understood in order to optimize the operation of short wavelength FELs.

Some of the most important detrimental effects caused by the microbunching instability are:

1) the emission of coherent radiation at beam diagnostic stations, which affects beam diagnostic techniques based on the emission of incoherent radiation (i.e. optical transition radiation screens).

2) The increase of the beam energy-spread and the generation of perturbations in the beam energy and density profile. These can both lower the gain of the free-electron laser and broaden its bandwidth when an external seed is used to start-up the FEL interaction.

[2] Note that this type of process is the basis of the FEL interaction, in which the exponential amplification of the radiation is accompanied by an exponential growth of the bunching factor at the resonant wavelength λ_r due to the interaction between electrons and radiation in combination with the finite dispersion of the magnetic undulator

3) Increase of the beam emittance in beamline systems with a finite x-z coupling (e.g. the central plane of a magnetic chicane).

Microbunching instabilities can be generated by different types of electromagnetic interactions like wake-fields in accelerating structures, coherent synchrotron radiation fields [28, 29] in systems of bending magnets or longitudinal space-charge fields [20, 21, 30]. The latter case is the main subject of this dissertation. In the remainder of this chapter we derive a simplified theory of the microbunching instabiltiy for a general electro-magnetic interaction. We will then describe a one-dimensional model of the space-charge instability and illustrate its connection to the physics of plasma oscillations.

2.5 One-Dimensional Model of the Microbunching Instability

In this section we give a brief one-dimensional description of the microbunching instability. We assume a parallel, quasi mono-energetic beam of central energy γmc^2. For a one-dimensional system, the electron beam can be described by a distribution function in longitudinal phase-space $f(z,\eta)$, where z is the longitudinal position along the electron beam and $\eta = \delta\gamma/\gamma$ is the relative energy deviation. The meaning of f is that $dN = f(z,\eta)dzd\eta$ is the number of particles in the unit phase-space area $dzd\eta$.

Neglecting binary interactions, the time evolution of the distribution function f is described by the Vlasov equation:

$$\frac{\partial f}{\partial \tau} + \dot{z}\frac{\partial f}{\partial z} + \dot{\eta}\frac{\partial f}{\partial \eta} = 0 \tag{2.35}$$

where $\dot{z}$ and $\dot{\eta}$ are, respectively, the time derivatives of the longitudinal position and relative energy deviation. For a relativistic beam, neglecting the transverse emittance, the longitudinal velocity in the beam coordinate system is given by $\dot{z} \simeq \frac{\eta}{\gamma^2}$.

Since we are interested in the evolution of small perturbations of the distribution function, the distribution function f can be expanded to first order in perturbation theory: $f = f_0 + f_1 e^{ik_z z}$, where $f_0 = n_0 \frac{e^{-\frac{\eta^2}{2\sigma_\eta^2}}}{\sqrt{2\pi}\sigma_\eta}$ is a stationary distribution function, with n_0 being the beam volume density and σ_η the relative energy-spread, and $f_1 \ll f_0$ is a periodic perturbation. Due to the effect of some collective field generated by the perturbation $f_1 e^{ik_z z}$, the electrons receive an energy kick with a periodic dependence in z: $\dot{\eta} = Z(k_z, f_1)e^{ik_z z}$. Substituting this form for the collective interaction term and neglecting the second order term $Z\frac{\partial f_1}{\partial \eta}$, the Vlasov equation reduces to:

$$\frac{\partial f_1}{\partial \tau} + ik_z \dot{z} f_1 + Z(k_z, f_1)\frac{\partial f_0}{\partial \eta} = 0. \tag{2.36}$$

For a cold beam, i.e. for $\frac{k_z \tau_c \sigma_\eta}{\gamma^2} \ll 1$, where τ_c is the interaction time, the second term in the linearized Vlasov equation can be neglected and we get:

$$f_1 = f_{1,0} - \tau_c Z(k_z)\frac{\partial f_0}{\partial \eta} \tag{2.37}$$

where $f_{1,0}$ is the initial value of the perturbation. After the interaction, the beam goes through a magnetic chicane with a finite longitudinal dispersion R_{56}. The effect of the chicane is that of shifting the longitudinal position of each electron by an amount proportional to the energy deviation $z \to z + \eta R_{56}$. The effect of this transformation on the phase-space perturbation is that of introducing a phase-shift proportional to the longitudinal displacement: $f_1 \to f_1 e^{-ik_z \eta R_{56}}$. The bunching factor $b = \int d\eta f_1/N$ is then given by:

$$b = b_0 - ik_z\tau_c R_{56} Z(k_z, f_1) n_0 e^{-(k_z\sigma_\eta R_{56})^2} \tag{2.38}$$

where $b_0 = \int d\eta f_{1,0}/N$ is the initial bunching factor.

For the example of the longitudinal space-charge interaction the energy kick is given by $\dot{\eta} = \frac{eE_z}{\gamma mc^2} = \frac{e^2}{ik_z\epsilon_0\gamma mc^2}\int f_{1,0}d\eta$ and the density modulation due to the microbunching instability is given by:

$$b = b_0 - b_0\gamma^2 R_{56}\tau_c\frac{\omega_p^2}{c^2}e^{-(k_z\sigma_\eta R_{56})^2/2}, \tag{2.39}$$

where $\omega_p^2 = e^2 n_0/\epsilon_0 m\gamma^3$

Just to get an idea of the orders of magnitude involved in this problem, consider the example of the LCLS beam at 135 MeV [21]. The beam goes through a tight waist for a length of $\tau_c = 2m$ right before the injection in the main accelerator through a dog-leg chicane with $R_{56} = -5mm$. The beam parameters at this point in the beamline yield: $\frac{\omega_p}{c} \simeq 2\pi/20m$, $\gamma \simeq 270$, and $\sigma_\eta \simeq 2\times 10^{-5}$. The resulting gain at $\lambda = 2\pi/k_z = 800nm$ is roughly $b/b_0 \simeq -80$.

Note that the uncorrelated energy-spread appears in the exponential damping factor in Eq. 2.38. This means that energy-spread can significantly damp the microbunching amplification. This effect is employed in advanced FEL injectors, in which the energy-spread of the electron beam is increased with an external laser to limit the effect of the microbunching instability [3].

This model lacks self-consistency since it has been assumed that $\dot{\eta}$ is independent of time, whereas the collective fields are affected by the time evolution of the distribution function. In the next section we will give a more accurate description of this process, including the self-consistent evolution of the distribution function during the beam interaction.

2.6 Self-Consistent Model of the Space-Charge Instability and its Connection to the Physics of Plasma Oscillations

In this section we discuss a self-consistent model of the microbunching instability induced by longitudinal space-charge forces. In the self-consistent approach, we will not assume that $\dot{\eta}$ is constant but we will compute it from the space-charge fields generated by the distribution function as it evolves in time. The linearized Vlasov equation for this system is:

$$\frac{\partial f_1}{\partial \tau} + \frac{\eta}{\gamma^2}\frac{\partial f_1}{\partial z} + \frac{eE_z}{\gamma mc^2}\frac{\partial f_0}{\partial \eta} = 0. \tag{2.40}$$

E_z is the longitudinal electric field which can be computed by solving the one-dimensional Poisson equation:

$$\frac{\partial}{\partial z}E_z = -\frac{e}{\epsilon_0}\int f_1 d\eta. \tag{2.41}$$

It is convenient to solve equations (2.40) and (2.41) using the Laplace-Fourier transforms, defined as:

$$\hat{f}_1 = \int f_1 e^{-ikz} dz \tag{2.42}$$

$$\tilde{\hat{f}}_1 = \int_0^\infty \hat{f}_1 e^{i\frac{\omega}{c}\tau} d\tau. \tag{2.43}$$

With these definitions, the Fourier-Laplace transforms of Eqs.(2.40,2.41) yield:

$$-i\frac{\omega}{c}\tilde{\hat{f}}_1 - \hat{f}_1\Big|_{\tau=0} + \frac{ik\eta}{\gamma^2}\tilde{\hat{f}}_1 + \frac{e}{\gamma mc^2}n_0\tilde{\hat{E}}_z\frac{\partial f_v}{\partial p} = 0 \tag{2.44}$$

and

$$\tilde{\hat{E}}_z = -\frac{i}{k}\frac{e}{\epsilon_0}\int \tilde{\hat{f}}_1 d\eta. \tag{2.45}$$

After some algebraic manipulation, it can be shown that the phase-space perturbation f_1 can be expressed as:

$$\tilde{\hat{f}}_1 = \frac{1}{-i\frac{\omega}{c} + \frac{ik\eta}{\gamma^2}}\left(\hat{f}_1\Big|_{\tau=0} - \frac{1}{\epsilon_p}\frac{\omega_p^2}{c^2}\frac{\partial f_v}{\partial \eta}\frac{\gamma^2}{ik}\int \frac{\hat{f}_1\Big|_{\tau=0}}{-i\frac{\omega}{c} + ik\frac{\eta'}{\gamma^2}}d\eta'\right) \tag{2.46}$$

where ϵ_p is the beam's plasma dielectric function given by:

$$\epsilon_p = 1 + \frac{\omega_p^2}{c^2}\frac{\gamma^2}{ik}\int \frac{\frac{\partial f_v}{\partial \eta}}{-i\frac{\omega}{c} + \frac{ik\eta}{\gamma^2}}d\eta. \tag{2.47}$$

The Laplace transform in Eq. 2.46 can be inverted using the residue theorem. By doing so, we only consider the poles corresponding to the zeros of the plasma dielectric function, since these poles are associated with the collective response of the electrons. The equation $\epsilon_p = 0$, whose solutions are the collective poles of the system, is defined as the dispersion relation.

For the moment we will be concerned with the cold beam limit, i.e. the limit for $k_z/k_D = k_z c\sigma_\eta/\omega_p\gamma^2 << 1$, where k_D is defined as the Debye wave-number. This condition means that the longitudinal displacement in a plasma-period of a particle with a relative energy deviation $\eta = \sigma_\eta$ is much smaller than the wavelength λ.

In the cold beam limit, the plasma dielectric function can be computed in closed form and yields:

$$\epsilon_p = 1 - \frac{\omega_p^2}{\omega^2} \tag{2.48}$$

which has the following zeros $\omega_\pm = \pm\omega_p$. With this result, the Laplace transform can be inverted, resulting in the following expression for the time evolution of the phase-space perturbation:

$$\hat{f}_1 = \sum_\pm \frac{e^{-i\frac{\omega_\pm \tau}{c}}}{-i\frac{\omega_\pm}{c} + \frac{ik\eta}{\gamma^2}} \Big(- \frac{1}{\frac{d\epsilon_p}{d\omega}|_{\omega_\pm}} \frac{\omega_p^2}{c^2} \frac{\partial f_v}{\partial \eta} \frac{\gamma^2}{ik} \int \frac{\hat{f}_1\Big|_{\tau=0}}{-i\frac{\omega_\pm}{c} + ik\frac{\eta'}{\gamma^2}} d\eta' \Big). \tag{2.49}$$

By multiplying Eq.(2.49) by the phase-factor $e^{-ik_z\eta R_{56}}$, which is introduced by the longitudinal dispersion, and integrating by parts in η we obtain the following value for the final microbunching:

$$b_{R_{56}} = \Big(b_0 \cos\frac{\omega_p \tau_c}{c} - b_0\gamma^2 R_{56} \frac{\omega_p}{c} \sin\frac{\omega_p\tau_c}{c} \Big) e^{-\frac{(k_z\sigma_\eta R_{56})^2}{2}}. \tag{2.50}$$

Equation 2.50 has an interesting physical interpretation. The bunching factor in the drift evolves, according to the plasma oscillation mechanism, as $b = b_0 \cos\frac{\omega_p\tau}{c}$. Note that the self-consistent gain formula depends on the time derivative of the bunching factor at the drift exit. Neglecting the effect of energy spread the bunching factor after the chicane is: $b_{R_{56}} = b(\tau_c) + \gamma^2 R_{56} db/d\tau|_{\tau=\tau_c}$. It follows that the gain mechanism can be interpreted as a fraction of plasma oscillation of duration τ_c followed by a space-charge free drift of length[3] $\gamma^2 R_{56}$, during which the microbunching evolves ballistically (see Fig. 2.5). The same interpretation holds for a finite energy spread, with the inclusion of the phase-mixing term $e^{-\frac{(k_z R_{56}\sigma_\eta)^2}{2}}$.

From this simplified one-dimensional model, it is clear that the physics of the

[3]Note that since the R_{56} of a drift space of length L is given by $R_{56} = L/\gamma^2$, the equivalent drift-length of a dispersive section is analogously defined $L_{eq} = \gamma^2 R_{56}$.

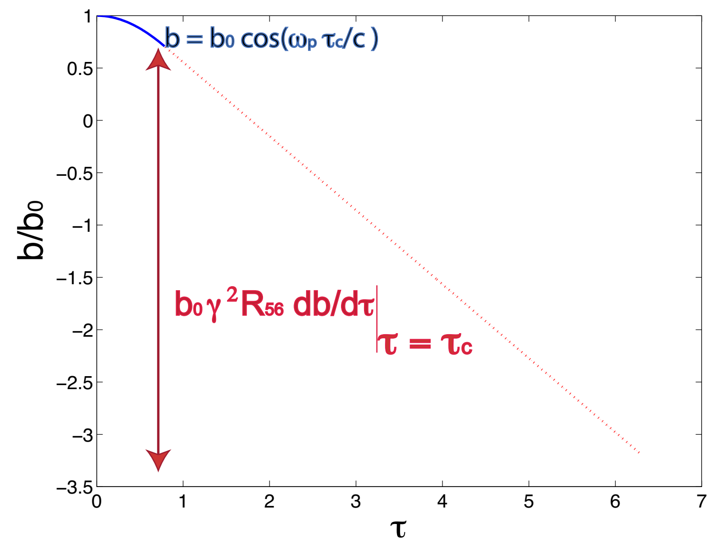

Figure 2.5: Physical interpretation of the space-charge induced microbunching instability: the microbunching evolution consists of a plasma oscillation followed by a free-drift in which the bunching factor evolves ballistically following the time derivative of the oscillation at the exit of the interaction zone.

space-charge microbunching instability is closely related to that of relativistic longitudinal plasma oscillations. The extension of this one-dimensional model to a full three-dimensional kinetic model will require a more general approach, with the inclusion of three-dimensional effects in the field equation (i.e. a full 3-D Poisson equations with a transverse Laplacian) and longitudinal and transverse electron motion with a thermal velocity spread. This generalized 3-D treatment will be the subject of the following chapters. We also want to note that the term microbunching instability might be confusing in the context of plasma oscillations, that are a stable process with and exponential damping induced by thermal effects. The microbunching amplification does not arise from the collective interaction alone, but from the combination of the collective interaction with the longitudinal dispersion in a magnetic chicane.

2.7 Radiation Processes from Relativistic Electrons

In this section we will discuss the emission of electromagnetic radiation from relativistic electrons. We will focus on two radiation processes that are relevant to this work: undulator radiation and transition radiation. These processes will be a key part of the experiments discussed in this dissertation both as part of advanced beam diagnostics and as radiators for the generation of coherent photons.

It is well known that an accelerating particle emits energy in the form of electromagnetic radiation. The differential energy-spectrum $dI/d\omega d\Omega$ is defined as the energy radiated per unit solid angle $d\Omega$ and unit frequency $d\omega$. In this dissertation we will be mostly concerned with coherent emission from a collection of particles. To compute the coherent radiation differential spectrum one must first compute the differential spectrum from a single particle and then sum the contributions from each individual particle with the correct phase. The computation of the radiation properties from a given process is particularly convenient in the so-called far-field zone. The far-field zone is defined by the condition $L > \lambda\gamma^2$, where L is the distance between the observation point and the radiator, λ is the wavelength of interest and γ is the Lorentz factor of the particle. In the far-field zone, the differential spectrum only depends on the observation angle and it's independent of the distance L. Under these conditions it can be shown (see [31]) that the single-particle differential spectrum is given by:

$$\frac{dI}{d\omega d\Omega} = \frac{e^2\omega^2}{16\pi^3\epsilon_0 c^2} |\int_{-\infty}^{+\infty} \hat{n} \times (\hat{n} \times \vec{\beta}) \exp\left(i\omega(t - \frac{\hat{n} \cdot r\vec{(t)}}{c})\right) dt|^2, \tag{2.51}$$

where $\hat{n}$ is the unit vector that identifies the observation angle of the radiation, $\vec{r}(t)$ is the particle position at the time t and $\vec{\beta} = \frac{d\vec{r}}{cdt}$. is the particle's velocity.

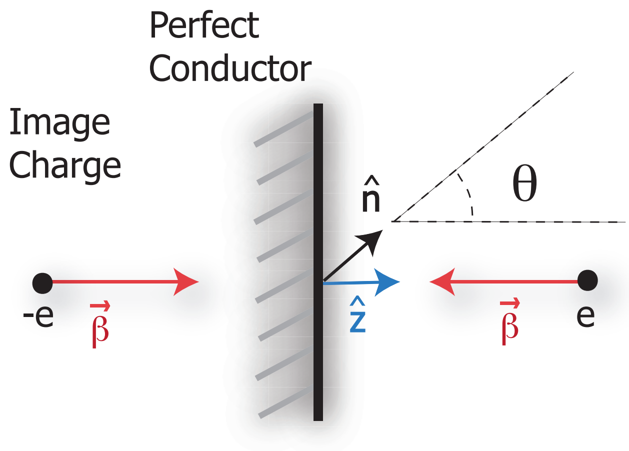

Figure 2.6: Schematics of the transition radiation process.

In the following sub-sections we will discuss the computation of the differential spectrum for some of the cases of interest in this work.

2.7.1 Transition Radiation

Transition radiation is emitted when a particle crosses an interface between two different media. The case of interest in this dissertation is the interface between vacuum and a conducting medium. Consider the following physical scenario: a particle travels in vacuum at a constant velocity $\vec{\beta} = \hat{z}\beta$ (see Fig. 2.6) in the z direction in the presence of an infinite conducting medium that occupies the region $z < 0$. The effect of the conductive wall can be taken into account by introducing an image charge of opposite sign that travels with the same velocity but in the opposite direction. . At the time $t = 0$ the particle hits a perfectly conducting wall and both the particle and the image particle are "annihilated". The fields from the two charges have to be added coherently and the differential spectrum is given by:

$$\frac{dI}{d\omega d\Omega} = \frac{e^2\omega^2}{4\pi^2c^2}\left|\beta\sin\theta\int_{-\infty}^{0}\exp\big(i\omega t(1-\beta\cos\theta)\big)+\exp\big(i\omega t(1+\beta\cos\theta)\big)dt\right|^2. \tag{2.52}$$

The time integral in Eq. 2.52 can be computed explicitly and yields [32]:

$$\frac{dI}{d\omega d\Omega} = \frac{e^2}{4\pi^3\epsilon_0 c^2}\frac{\beta^2\sin^2\theta}{(1-\beta^2\cos^2\theta)^2}. \tag{2.53}$$

For a relativistic electron $\gamma = \sqrt{\frac{1}{1-\beta^2}} \gg 1$ and Eq. 2.53 can be simplified as:

$$\frac{dI}{d\omega d\Omega} = \frac{e^2}{4\pi^3\epsilon_0 c^2}\frac{\gamma^2\theta^2}{(1+\gamma^2\theta^2)^2}. \tag{2.54}$$

The transition radiation differential spectrum is equal to 0 on axis, has a peak at $\theta = 1/\gamma$ and rolls off as $1/\theta^2$ for large angles. Due to its slow roll-off at large angles, the transition radiation angular spectrum has strong high-frequency components which result in high spatial resolution (on the order of the wavelength) in the near-field [33]. For this reason, incoherent transition radiation is commonly used as a high-resolution beam profile monitor (see e.g. [34]). Also, transition radiation is a rather simple and inexpensive way to extract coherent radiation from a particle beam [35] and it is often used for the coherent diagnostic of microbunched beams [36].

2.7.2 Undulator Radiation

An undulator is a periodic array of dipole magnets that are arranged with alternating polarity. The periodic magnetic field excites transverse periodic oscillations in the trajectory of an electron traveling across the undulator. We will here discuss the case of a circularly polarized undulator, also called helical undulator.

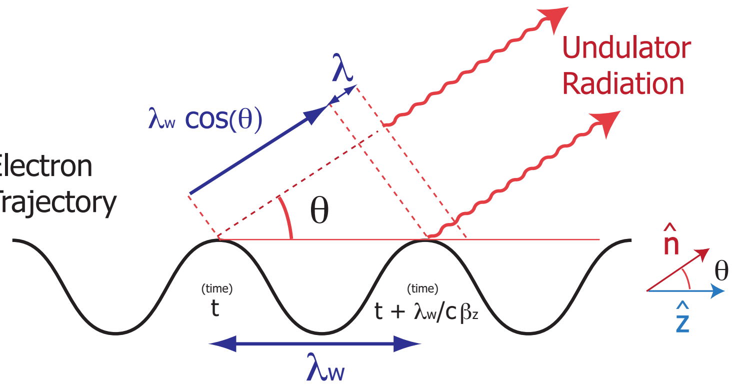

Figure 2.7: Schematics of the undulator radiation process, illustrating the angle-frequency correlation.

The field of a helical undulator can be expressed as:

$$\vec{B} = B_0 \hat{x} \cos(k_w z) \cosh(k_w x) + B_0 \hat{y} \sin(k_w z) \cosh(k_w y), \tag{2.55}$$

where B_0 is the field amplitude, $k_w = 2\pi/\lambda_w$ is the undulator frequency and $\hat{x}, \hat{y}$ are the unit vectors in the transverse plane. For a relativistic electron traveling in the z direction, the trajectories in the undulator are given by:

$$\begin{aligned} \vec{\beta}_\perp &= -\frac{K}{\gamma} \left(\hat{x} \cos k_w z + \hat{y} \sin k_w z \right) \\ \vec{r}_\perp &= \frac{K}{k_w \gamma} \left(\hat{x} \sin k_w z - \hat{y} \cos k_w z \right), \end{aligned} \tag{2.56}$$

where $K = eB_0/k_w mc$ is the undulator parameter. Note that the electron trajectory is a helix with a helicity that is opposite to that of the magnetic fields.

Due to the periodicity of the electron motion, the radiation will be emitted around a discrete set of resonant frequencies. While the emission frequencies could be computed by substituting the electron trajectories in Eq. 2.51, it is more instructive to give an intuitive picture of how the discrete undulator radiation frequencies arise. With reference to Fig. 2.7, consider an electron traveling in a periodic trajectory in the transverse plane. The wave-fronts emitted at each oscillation period interfere coherently only if they are emitted with a phase-difference that is a multiple of 2π. For a given observation angle, such condition is achieved only at a discrete set of wavelengths:

$$\lambda = \lambda_w(1/\beta_z - \cos\theta)/n \simeq \lambda_w \frac{1 + K^2 + \gamma^2\theta^2}{2n\gamma^2}. \tag{2.57}$$

where n is a positive integer. The emission wavelengths correspond to the harmonics undulator wavelength doppler-shifted twice: to the beam's rest frame and back to the laboratory frame (hence the factor $1/\gamma_z^2 = (1+K^2)/\gamma^2$). This means that the undulator radiation can be seen as a scattering process of a virtual photon field.

The differential spectrum is [37]:

$$\frac{dI}{d\omega d\Omega} = \frac{e^2\omega^2K^2}{4\pi^3\epsilon_0 c\omega_0^2\gamma^2}\sum_{n=1}^{\infty}\left(J_n'^2(x) + (\frac{\gamma\theta}{K} - \frac{n}{x})^2\right) J_n^2(x)\frac{\sin^2\left(N\pi(\frac{\omega}{\omega_1} - n)\right)}{(\frac{\omega}{\omega_1} - n)^2}. \tag{2.58}$$

where N is the number of undulator periods, $\omega_0 = k_w/c$, $\omega_1 = 2\gamma^2\omega_0/1 + K^2$ and $x = K\omega\theta/\gamma\omega_0$. For each angle, the frequency bandwidth is $\delta\omega/\omega \simeq 1/N$ (which can be rather narrow for a large number of periods), while the integrated spectrum has a broad frequency bandwidth due to the angle/frequency correlation. Note that, unlike transition radiation, undulator radiation has a non-zero emission on axis.

2.7.3 Radiation from a Collection of Particles: Coherent vs. Incoherent Emission

When computing the differential spectrum for a bunch of particles, one needs to sum the contributions from each particle coherently. The position of each particle in the bunch can be expressed as $\vec{r}_j = \vec{r}_b(t) + \vec{x}_j$, where it was assumed that the relative positions of the particles (identified by the vectors $\vec{x}_j$) are frozen during the emission process. The differential spectrum for the entire bunch is then given by:

$$\frac{dI}{d\omega d\Omega} = \frac{e^2\omega^2}{16\pi^3\epsilon_0 c^2} \left| \sum_j \int_{-\infty}^{+\infty} \hat{n} \times (\hat{n} \times \vec{\beta}) \exp\left(i\omega \left(t - \frac{\hat{n} \cdot (\vec{r}_b(t) + \vec{x}_j)}{c} \right) \right) dt \right|^2 . \tag{2.59}$$

The term $\exp(-i\omega\frac{\hat{n}\vec{x}_j}{c})$ can be factored out from the time integral, leaving the following expression for the differential spectrum:

$$\frac{dI}{d\omega d\Omega} = N^2 \left|B(\hat{n},\omega)\right|^2 \frac{dI}{d\omega d\Omega}|_{sp}, \tag{2.60}$$

where $B(\hat{n},\omega) = \frac{1}{N}\sum_j exp(-i\omega\frac{\hat{n}\vec{x}_j}{c})$ is defined as the beam's form factor. In the remainder of the dissertation we will express the form factor as a function of the wave-vector $\vec{k} = \hat{n}\omega/c$. With the latter notation, it is clear that the form factor B is the three-dimensional Fourier transform of the beam's charge distribution normalized to the number of particles. B is the three-dimensional extension of the bunching factor b defined in Subsection 2.3. The form factor B has a maximum absolute value of 1, which is realized when the particles are arranged periodically in thin microbunches oriented along the direction of $\vec{k}$. For a finite value of the form factor, the emission scales as $I \propto N^2$ and it said to be coherent or superradiant. Following the same line of reasoning as Subsection 2.3

(in particular the derivation of Eq.2.30), if the particles position are randomly distributed, then the form factor has a vanishing statistical average but a non-vanishing average power: $< |B|^2_{random} >= 1/N$. In the latter case the emitted energy scales like $I \propto N$ and it is defined incoherent or spontaneous emission.

CHAPTER 3

Six-Dimensional Theory of Space-Charge Waves in a Thermal Relativistic Electron Beam: Eigenvalue/Eigenmode Analysis

The subject of this chapter is the eigenvalue problem of longitudinal plasma oscillations in six-dimensional phase space. The aim of this analysis is that of finding self-consistent solutions to the set of Vlasov-Poisson equations that describe the dynamics of a relativistic electron beam under the combined effects of longitudinal space-charge forces and transverse focusing. This analysis represents the basis of our theory of collective longitudinal space-charge effects since it provides a basis of propagating eigenmodes which will be employed in the following chapters to describe collective beam effects such as microbunching amplification or suppression.

As mentioned in the previous chapters, the theory of plasma oscillations in non-relativistic plasmas is well established and dates back to the seminal work of Landau [38] and Jackson [4]. The problem of plasma oscillations in the context of high brightness electron beams has been treated previously with one-dimensional [14] and three-dimensional theoretical models [22] in the cold, laminar beam approximation. In a recent experiment [39], relativistic plasma oscillations in high-brightness electron beams were directly observed at the Pegasus laboratory of UCLA.

In this chapter we study the plasma oscillation eigenvalue problem for a thermal non-laminar electron beam in three dimensions, i.e., with the inclusion, for the first time, of the effects of finite emittance, transverse focusing, energy spread and edge effects due to the finite size of the beam. Our analysis is based on the formalism developed by Kim, Yu, Xie et al. (see [40, 10, 41]) for the three-dimensional free-electron laser dispersion relation. This approach has been highly successful in describing three-dimensional and kinetic effects in free-electron lasers and its extension to the study of plasma oscillations will provide a special insight into the physics of this problem and, at the same time, be an efficient tool for a quantitative description of the phenomena involved.

The primary focus of this chapter is the study of propagating space-charge eigenmodes. We find solutions to the electric field equations in the form of waves that propagate in the forward or backward z-direction with a given complex frequency ω and a characteristic transverse structure $E_z(\vec{x})$. We reduce the system of equations describing the motion of the electrons under the effect of collective longitudinal space-charge forces, to an integro-differential equation, which we denote the dispersion relation. The complex frequency ω and the spatial dependence $E_z(\vec{x})$, deduced by solving the dispersion relation, define the eigenvalue and field eigenmode of the oscillation.

This analysis has been published in [42]. In this dissertation we will give a more detailed explanation of the mathematics involved.

This chapter is organized as follows: in section 3.1 we derive the dispersion equation for the plasma eigenmodes and define the dimensionless scaling parameters and variables that describe the problem; in section 3.2 we show how our three-dimensional approach reduces to a one-dimensional (1-D) problem when finite beam effects and transverse focusing are negligible and the well known

1-dimensional dispersion relation for a thermal plasma is derived in the limit for negligible emittance; in section 3.3 a variational approximation for the dispersion relation is derived and employed to find closed form expressions for the plasma oscillation frequency for a cold beam, as well as numerical solutions for a warm beam describing the Landau damping due to the longitudinal thermal motion induced by energy-spread and emittance; in chapter 3.4 the dispersion relation is expressed in the spatial frequency domain by means of a transverse two-dimensional Fourier transform and show how the effect of plasma-betatron beat-waves arises from this form of the equation; finally in section 3.5 we compute numerical solutions to the exact dispersion relation using a discretization method.

3.1 Three-dimensional dispersion relation with energy spread, emittance and betatron focusing

In this section the dispersion relation for the plasma oscillation modes is derived. We assume a coasting, non-accelerating relativistic beam, which propagates in a uniform focusing channel. The electron beam is described by a distribution function in six-dimensional phase space $f(\vec{x}, \vec{\beta}_\perp, z, \eta, \tau)$, where $\vec{x}$ is the transverse position, $\vec{\beta_\perp}$ is the transverse velocity normalized to the speed of light, η is the relative energy deviation with respect to the central beam energy γmc^2, z is the longitudinal position along the electron beam relative to a reference particle traveling at $\beta_z = \sqrt{1 - 1/\gamma^2}$ and $\tau = ct$.

The evolution of the six-dimensional distribution function is governed by the

Vlasov equation:

$$\partial_\tau f + \vec{\beta}_\perp \cdot \vec{\nabla}_{\vec{x}} f + \dot{\vec{\beta}}_\perp \cdot \vec{\nabla}_{\vec{\beta}_\perp} f + \dot{z}\partial_z f + \dot{\eta}\partial_\eta f = 0. \tag{3.1}$$

The Vlasov equation describes the phase-space evolution of a collisionless plasma. As discussed in chapter 2, the Vlasov equation can be derived from first principles and can be interpreted as the evolution equation of an incompressible fluid in six-dimensional phase-space. The obvious physical interpretation is that the time evolution of an electron beam is such that the overall phase-space volume occupied by the particles is a constant of the motion. Another way of stating this concept is that the distribution function f computed along the particle phase-space trajectories is constant in time. It follows that for a set of constants of the motion $(c_1, c_2, ...c_n)$ any function of the type $f(c_1, c_2, ...c_n)$ is a stationary solution to the Vlasov equation.

We expand the distribution function to first order in perturbation theory: $f = f_0 + f_1 e^{ik_z z}$, where f_0 is a stationary solution to the Vlasov equation and $|f_1| << |f_0|$. We also assume that the electron beam is matched to the focusing channel. The unperturbed trajectories of the electrons are:

$$\begin{aligned}
&\vec{x} = \vec{x}_0 \cos k_\beta \tau + \frac{\vec{\beta}_{\perp 0}}{k_\beta} \sin k_\beta \tau \\
&\vec{\beta}_\perp = -k_\beta \vec{x}_0 \sin k_\beta \tau + \vec{\beta}_{\perp 0} \cos k_\beta \tau \\
&\eta = \eta_0 \\
&z = z_0 - \int_0^\tau \frac{\vec{\beta}_\perp^2}{2} d\tau' + \tau \left(\frac{\eta}{\gamma^2}\right)
\end{aligned} \tag{3.2}$$

where $(\vec{x}_0, \vec{\beta}_{\perp 0}, z_0, \eta_0)$ is the phase space position at $\tau = 0$ and ck_β is the betatron frequency of the focusing channel. Since η and $\vec{x}^2 + \frac{\vec{\beta}_\perp^2}{k_\beta^2}$ are constants of the motion, it follows that any function of the type $f_0(\vec{x}^2 + \frac{\vec{\beta}_\perp^2}{k_\beta^2}, \eta)$ is a stationary solution to the Vlasov equation.

With these underlying assumptions, expanding Eq.(3.1) to first order we obtain the linearized Vlasov equation for the system:

$$\partial_\tau f_1 + \vec{\beta}_\perp \cdot \vec{\nabla}_{\vec{x}} f_1 - k_\beta^2 \vec{x} \cdot \vec{\nabla}_{\vec{\beta}_\perp} f_1 + i k_z \dot{z} f_1 + \frac{e\mathscr{E}_z}{\gamma m c^2} \partial_\eta f_0 = 0 \tag{3.3}$$

where $\dot{z} = \eta/\gamma^2 - (k_\beta^2 \vec{x}^2 + \vec{\beta}_\perp^2)/4$ and, for the sake of simplicity, the $\vec{\beta}_\perp^2/2$ term in the longitudinal velocity $\dot{z}$ has been replaced with its average over a betatron period. Equation 3.3 can be rewritten in a form that is both more simple and physically more intuitive:

$$\frac{D}{D\tau} f_1(\vec{x}_+, \vec{\beta}_+) + i k_z \dot{z} f_1(\vec{x}_+, \vec{\beta}_+) = -\frac{e\mathscr{E}_z(\vec{x}_+)}{\gamma m c^2} \partial_\eta f_0 \tag{3.4}$$

where $\vec{x}_+(\tau) = \vec{x}_0 \cos k_\beta \tau + \frac{\vec{\beta}_{\perp 0}}{k_\beta} \sin k_\beta \tau$, $\vec{\beta}_+(\tau) = -k_\beta \vec{x_0} \sin k_\beta \tau + \vec{\beta}_{\perp 0} \cos k_\beta \tau$ and $\frac{D}{D\tau}$ is the total derivative computed along the unperturbed trajectories $(\vec{x}_+, \vec{\beta}_+)$.In this form, the linearized Vlasov equation has a simple physical interpretation: if we turn off the longitudinal space-charge field, the evolution of the perturbed distribution is ballistic and it's just given by the initial phase-space perturbation transported along the 0-th order particle trajectories $f_1 = f_{1,0}\left(\vec{x} \cos k_\beta \tau - \frac{\vec{\beta}_\perp}{k_\beta} \sin k_\beta \tau, k_\beta \vec{x} \sin k_\beta \tau + \vec{\beta}_\perp \cos k_\beta \tau\right) e^{-i k_z \dot{z} \tau}$, where $f_{1,0}$ is the the phase-space perturbation at $\tau = 0$. If we include a finite space-charge field $\mathscr{E}_z$, the distribution function f_1 receives an energy kick that is proportional to the electric field at the local position in phase-space, which corresponds to the right hand side of Eq. 3.4.

Since we are looking for steady-state solutions to the space-charge wave problem, we can assume that the interaction between the electron beam and the space-charge field takes place from $\tau = -\infty$. With this above assumption, Eq.(3.3) can be solved as:

$$f_1 = -\frac{e}{\gamma mc^2}\int_{-\infty}^{0} e^{ik_z\dot{z}\tau'}\mathscr{E}_z(\vec{x}\cos k_\beta\tau' + \frac{\vec{\beta}_\perp}{k_\beta}\sin k_\beta\tau', \tau'+\tau)\partial_\eta f_0 d\tau'. \tag{3.5}$$

The longitudinal space-charge field $\mathscr{E}_z$ can be derived by solving Poisson's equation in the beam's rest frame, where self-magnetic fields can be neglected [43, 30]:

$$(\nabla_\perp^2 - \frac{k_z^2}{\gamma^2})\frac{\mathscr{E}_z}{-\frac{ik_z}{\gamma}} = -\frac{e}{\gamma\epsilon_0}\int f_1 e^{ik_z z} d\eta d^2\vec{\beta}_\perp. \tag{3.6}$$

Assuming that $\mathscr{E}_z = E_z(\vec{x})e^{ik_z z - i\frac{\omega\tau}{c}}$ and substituting Eq.(3.5) into Eq.(3.6), we obtain the following integral equation for the plasma oscillation modes:

$$(\nabla_\perp^2 - \frac{k_z^2}{\gamma^2})E_z = -\frac{ik_z e^2}{\gamma^3 mc^2\epsilon_0}\int\int_{-\infty}^{0} e^{ik_z\dot{z}\tau - i\frac{\omega\tau}{c}}E_z(\vec{x}\cos k_\beta\tau + \frac{\vec{\beta}_\perp}{k_\beta}\sin k_\beta\tau)\partial_\eta f_0 d\tau d\eta d^2\vec{\beta}_\perp. \tag{3.7}$$

Note that, so far, no assumption has been made on the explicit form of f_0 and Eq.(3.7) applies to any stationary distribution. In what follows we will assume the following form for the zeroth order distribution: $f_0 = n_0 e^{-\frac{\vec{x}^2}{2\sigma_x^2} - \frac{\vec{\beta}_\perp^2}{2\sigma_x^2 k_\beta^2} - \frac{\eta^2}{2\sigma_\eta^2}}/(2\pi)^{3/2}\sigma_x^2 k_\beta^2\sigma_\eta$ where n_0 is the beam volume density on axis and σ_x is the root mean square size of the matched charge distribution.

Performing the integral in $d\eta$ by parts one obtains:

$$\begin{aligned}(\nabla_\perp^2 - \frac{k_z^2}{\gamma^2})E_z = -\frac{k_z^2\omega_p^2}{\gamma^2 c^2}\int\int_{-\infty}^{0} \tau e^{-\frac{(k_z\sigma_\eta\tau)^2}{2\gamma^4} - ik_z\frac{k_\beta^2\vec{x}^2 + \vec{\beta}_\perp^2}{4}\tau - i\frac{\omega\tau}{c}} \\ \times E_z(\vec{x}\cos k_\beta\tau + \frac{\vec{\beta}_\perp}{k_\beta}\sin k_\beta\tau)f_{0\perp}d\tau d^2\vec{\beta}_\perp\end{aligned} \tag{3.8}$$

where $\omega_p^2 = n_0 e^2/\gamma^3 m\epsilon_0$ is the relativistic beam plasma frequency and $f_{0\perp} = e^{-\frac{\vec{x}^2}{2\sigma_x^2}-\frac{\vec{\beta}_\perp^2}{2\sigma_x^2 k_\beta^2}}/2\pi\sigma_x^2 k_\beta^2$. Equation (3.8) is an eigenvalue integral equation which has to be solved in ω and $E_z(\vec{x})$, its solutions are the eigenvalues and eigenmodes of the plasma oscillation problem. The resulting electric field $\mathscr{E}_z = E_z(\vec{x})e^{ik_z z - i\frac{\omega\tau}{c}}$ describes a wave that propagates in the longitudinal direction (either backwards or forward depending on the relative signs of ω and k_z) with a fixed transverse profile.

3.1.1 Universally scaled dispersion equation

The dispersion relation in Eq.(3.8) can be expressed in terms of four dimensionless scaling parameters. We give the following definitions:

$D = k_z\sigma_x/\gamma$ is the 3-D parameter, which accounts for edge effects due to the finite size of the beam. To understand intuititively how edge effects affect the plasma dynamics, we recall that the single-particle longitudinal electric field, in the frequency domain, can be expressed as: $E_{sp}(\vec{x}) = \frac{-ik_z e}{2\pi\gamma^2\epsilon_0}K_0\left(\frac{k_z|\vec{x}|}{\gamma}\right)$. The single particle field tends to zero exponentially as a function of $k|\vec{x}|/\gamma$ for $k|\vec{x}|/\gamma > 1$. For $D >> 1$, then, edge effects can be neglected since the electrons in the center of the beam are not affected by the field generated by those at the edges, whereas for $D << 1$ the system is dominated by edge effects;

$K_\gamma = k_z c\sigma_\eta/\omega_p\gamma^2$ is the energy spread parameter and corresponds to the ratio of the longitudinal wave-number k_z to the Debye wave-number associated with energy spread. This parameter can be interpreted as the ratio of the longitudinal thermal displacement in a plasma period to the wavelength $2\pi/k$. If $K_\gamma << 1$ thermal motion due to energy spread is negligible on the time-scale of a plasma oscillation and the effects of energy spread can be neglected;

$K_\epsilon = k_z c(k_\beta \sigma_x)^2/2\omega_p$ is the emittance parameter and it corresponds to the ratio of k_z to the Debye wave-number associated with emittance. K_ϵ has a similar physical meaning as K_γ, with longitudinal thermal motion being induced by transverse emittance instead of energy spread;

$K_\beta = k_\beta c/\omega_p$ is the focusing parameter. If $K_\beta << 1$ transverse motion due to focusing is negligible on the time-scale of a plasma oscillation and the electron dynamics can be considered transversely laminar, we will thus refer to this limit as the laminar beam limit. In the opposite limit ($K_\beta >> 1$) particles perform several betatron oscillations in a plasma period and transverse motion cannot be neglected, we will denote this condition the high betatron frequency limit.

Finally the mode oscillation frequency is normalized to the plasma frequency as $\Omega = \omega/\omega_p$. The resulting universally scaled dispersion relation is then:

$$\begin{aligned}\left(\frac{1}{D^2}\nabla_\perp^2 - 1\right) E_z = -\int\int_{-\infty}^{0} T e^{-\frac{(K_\gamma T)^2}{2} - \frac{\left(\vec{X}^2+\vec{B}^2\right) iK_\epsilon T}{2} - i\Omega T} \\ \times E_z(\vec{X}\cos K_\beta T + \vec{B}\sin K_\beta T) F_{0\perp} dT d^2\vec{B}\end{aligned} \tag{3.9}$$

where $F_{0\perp} = (k_\beta \sigma_x)^2 f_{0\perp}$ and we have introduced the following scaled variables: $T = \frac{\omega_p \tau}{c}$, $\vec{X} = \vec{x}/\sigma_x$, $\vec{B} = \vec{\beta}_\perp / k_\beta \sigma_x$.

Finally by changing the integration variable in the $d^2\vec{B}$ integral to $\vec{X}' = \vec{B}\sin K_\beta T + \vec{X}\cos K_\beta T$, we get:

$$\left(\frac{1}{D^2}\nabla_\perp^2 - 1\right) E_z = -\int E_z(\vec{X}')\Pi(\vec{X},\vec{X}') d^2\vec{X}' \tag{3.10}$$

with:

$$\Pi(\vec{X},\vec{X}') = \int_{-\infty}^{0} \frac{T e^{-\frac{(K_\gamma T)^2}{2} - i\Omega T} e^{-\left(\vec{X}^2+\vec{X}'^2 - 2\vec{X}\cdot\vec{X}'\cos K_\beta T\right)\frac{(1+iK_\epsilon T)}{2\sin^2 K_\beta T}}}{2\pi \sin^2 K_\beta T} dT. \tag{3.11}$$

Solution of Eq.(3.11) gives the eigenmode E_z and the scaled oscillation frequency Ω in terms of the four scaling paramters D, K_β, K_γ and K_ϵ. In the following sections we will find solutions to the dispersion relation and derive some of its relevant limiting forms.

3.2 The one-dimensional limit: transverse mode degeneracy and degeneracy breaking

A particularly important limiting form of the dispersion relation is found in the 1-dimensional (1-D) limit, i.e. the limit for $D \to \infty$ and $K_\beta \to 0$. Mathematically, this limit is obtained by using the following identity: $\lim_{K_\beta\to 0} \frac{1}{2\pi\sin^2 K_\beta T} e^{-\frac{\left(\vec{X}^2+\vec{X}'^2-2\vec{X}\cdot\vec{X}'\cos K_\beta T\right)(1+iK_\epsilon T)}{2\sin^2 K_\beta T}} = \frac{1}{1+iK_\epsilon T}\delta(\vec{X}'-\vec{X})$ and by noting that, for $D \to \infty$ the transverse Laplacian in Eq.(3.10) is negligible. In the one-dimensional (1-D) limit , all the modes are degenerate (i.e. they all have the same eigenvalue) and the dispersion relation reduces to:

$$1 - \int_{-\infty}^{0} \frac{T}{1+iK_\epsilon T} e^{-\frac{(K_\gamma T)^2}{2} - i\Omega T} dT = 0. \tag{3.12}$$

Finally, taking $K_\epsilon \to 0$, Eq.(3.12) reduces to the well-known one-dimensional dispersion relation for a thermal plasma derived in [4]:

$$1 - \frac{1}{2K_\gamma^2} Z'\left(\frac{\Omega}{\sqrt{2}K_\gamma}\right) = 0 \tag{3.13}$$

where Z' is the complex derivative of the plasma dispersion function [4] defined as $Z(\zeta) = 2ie^{-\zeta^2}\int_{-\infty}^{i\zeta} e^{-x^2}dx$ (see the derivation in the Appendix). For $K_\gamma = 0$, Eq.(3.13) has two solutions $\Omega = \pm 1$ (or $\omega = \pm\omega_p$) which are the one-dimensional oscillation frequencies for a cold relativistic plasma.

Mode degeneracy in the one-dimensional limit can be explained by examining the system in its rest frame. In the rest frame, for $D >> 1$ (or $\frac{k\sigma_x}{\gamma} >> 1$) the wavelength is much smaller than the transverse size of the beam. In this case, if the transverse motion is laminar, the beam can be considered as a uniform infinite plasma, in which different regions of the transverse plane evolve independently, thus allowing plasma oscillations with an arbitrary transverse profile. Mode degeneracy is broken when the electric field phase information is transferred across the beam's transverse distribution and the electrons at the center of the beam are affected by those at the edges. This can happen either by geometrical or kinetic effects. Namely if $D >> 1$ does not apply, the single particle electric field establishes a transverse correlation across the whole beam (see the discussion on the D parameter in section 3.1.1), whereas if $K_\beta << 1$ does not apply the phase information is carried by the electron betatron motion across the transverse plane.

Degeneracy breaking of the plasma eigenmodes induced by transverse focusing is an important new result of our kinetic analysis with respect to previous models based on the laminar beam approximation. This effect has experimental relevance since mode degeneracy in the 1-D limit has immediate applications in shot-noise reduction experiments. Noise reduction can be achieved on a broad angular spectrum only if all the modes have the same oscillation frequency and, thus, reach the one-quarter plasma oscillation point at the same time (note that shot-noise will couple to several transverse modes due to its broad angular distribution).This can only be obtained in the $D >> 1$ limit for $K_\beta << 1$. If this is not the case, shot-noise reduction may be obtained only on one transverse mode, which can still be of interest in applications such as seeded free-electron lasers, in which the main contribution from shot-noise comes from the fundamental transverse mode.

3.3 Variational Solution for the Fundamental Mode

A good approximation for the eigenvalues of the plasma oscillation dispersion relation can be obtained with a variational method. The variational method for the fundamental mode can be implemented by projecting the dispersion equation in Eqs.(3.10,3.11) on a pure gaussian mode $E_z = e^{-w|\vec{X}|^2}$[1] and imposing the condition that the eigenvalue be stationary as a function of w: $d\Omega/dw = 0$[41, 10]. This procedure is equivalent to approximating the fundamental plasma eigenmode with a gaussian shaped mode and finding the value of w for which the gaussian best approximates the exact mode.

This results in two coupled equations that need to be solved for Ω and w:

$$\frac{1}{4w} + \frac{1}{2D^2} = \int_{-\infty}^{0} \frac{Te^{-\frac{(K_\gamma T)^2}{2} - i\Omega T}}{(1+iK_\epsilon T)^2 + 4w(1+iK_\epsilon T) + 4w^2 \sin^2 K_\beta T} dT \qquad (3.14)$$

$$\frac{1}{4w^2} = \int_{-\infty}^{0} \frac{4(1+iK_\epsilon T) + 8w \sin^2 K_\beta T}{\left((1+iK_\epsilon T)^2 + 4w(1+iK_\epsilon T) + 4w^2 \sin^2 K_\beta T\right)^2} Te^{-\frac{(K_\gamma T)^2}{2} - i\Omega T} dT. \qquad (3.15)$$

Simultaneous solutions of Eqs. (3.14,3.15) provide an approximate solution to the eigenvalue problem of Eqs.(3.10, 3.11) in terms of the dimensionless scaling parameters.

[1] The choice of a Gaussian distribution allows the analytical computation of the spatial and velocity integrals, thus giving simple solutions for the integro-differential dispersion relation.

3.3.1 Variational solutions in the cold beam limit

The cold beam limit is identified by the conditions of vanishing energy spread ($K_\gamma << 1$) and vanishing emittance ($K_\epsilon << 1$). The laminar beam limit is identified by the condition $K_\beta << 1$, in which the transverse position of the electrons can be considered fixed for the relevant time scale. In the cold, laminar beam limit the time integrals in Eqs. (3.14, 3.15) can be solved analytically and yield:

$$\frac{1}{4w} + \frac{1}{2D^2} = \frac{1}{1+4w}\frac{1}{\Omega^2} \tag{3.16}$$

$$\frac{1}{4w^2} = \frac{4}{(1+4w)^2}\frac{1}{\Omega^2} \tag{3.17}$$

which have the following solutions:

$$\Omega = \pm\frac{\sqrt{2}D}{1+\sqrt{2}D} \tag{3.18}$$

with $w = D/2\sqrt{2}$. This result can be identified as the fundamental mode plasma frequency reduction factor in the variational approximation and accounts for edge effects due to the finite size of the beam. Note that in the $D >> 1$ limit we recover the 1-D oscillation frequency whereas for $D << 1$ the oscillation frequency is significantly reduced. This effect is due to the suppression of longitudinal fields caused by the geometry of the electron beam in its rest frame. In the $D << 1$ limit (or $k_z\sigma_x/\gamma << 1$), the transverse size of the beam is smaller than the wavelength in the rest frame and the collective longitudinal electric field (which is Lorentz-invariant) is strongly reduced.

Another relevant limit, from the experimental point of view, is the high betatron frequency limit for a cold beam, i.e. the limit for $K_\beta >> 1$, $K_\gamma << 1$ and

$K_\epsilon << 1$ (the condition on K_β can actually be relaxed, as we will see in Section 3.4: in most practical cases the high betatron frequency condition can be identified as $K_\beta > 1$). In many experiments related to high frequency space-charge phenomena, in fact, the beta-function is very small to enhance the collective response of the electrons (thus fulfilling the high betatron frequency condition) but the brightness of the electron beam is high enough that the low emittance approximation is still valid. The case in which the latter condition is not verified will be discussed in the next subsection.

For $K_\beta >> 1$, the $\sin^2 K_\beta T$ term in the time integral in Eqs. (3.14,3.15) can be substituted with its average value. With this approximation the time integral can be solved analytically and the two resulting variational equations are:

$$\frac{1}{4w} + \frac{1}{2D^2} = \frac{1}{1+4w+2w^2}\frac{1}{\Omega^2} \tag{3.19}$$

$$\frac{1}{4w^2} = \frac{4+4w}{(1+4w+2w^2)^2}\frac{1}{\Omega^2}. \tag{3.20}$$

For $D >> 1$, Eqs. (3.19,3.20) yeld: $\Omega \approx \pm\sqrt{\frac{1}{1+\frac{1}{\sqrt{2}}}} \approx \pm 0.765$ and $w \approx \frac{1}{\sqrt{2}}$. In the opposite limit ($D << 1$) we have $\Omega \approx \pm\sqrt{2}D(1-\sqrt{2}D)$ and $w \approx \frac{D}{2\sqrt{2}}(1-\frac{D}{4\sqrt{2}})$.

Note that for $D << 1$ the eigenvalues in the laminar beam limit and in the high betatron frequency limit agree to second order in D. This can be understood by noting that, for $D << 1$, the transverse profile of the electric field extends well beyond the transverse beam distribution. In this case, the field can be considered uniform within the electron beam and betatron motion makes little difference since an electron oscillating transversely samples no field variation across the transverse plane. For $D >> 1$, instead, the collective response is reduced for $K_\beta >> 1$ with respect to the laminar beam limit ($K_\beta << 1$). This can be explained as follows: in the cold, laminar beam limit, for $D >> 1$, we found that the fundamental plasma eigenmode tends to be confined close to the center of the beam ($w = D/2 >> 1$); betatron motion in the $K_\beta >> 1$ limit, however, tends to spread out transversely the perturbed charge distribution, reducing the intensity of the space-charge field. The resulting steady state situation is that of a mode with a transverse size comparable to the beam size ($w = 1/\sqrt{2}$) and a weaker collective response from the electrons. The following heuristic formula is valid within 5% of the numerical solution for $D > 0.01$:

$$\Omega = \frac{\sqrt{2}D}{e^{-\alpha D} + \beta D} \tag{3.21}$$

with $\beta = \sqrt{2}/0.763$ and $\alpha = \beta - \sqrt{2}$. Note that this formula approaches asymptotically the exact solution in both the $D \gg 1$ and $D \ll 1$ limits.

3.3.2 Energy-spread and emittance effects: the Landau damping constant

In the case of a beam with finite emittance ($K_\epsilon \neq 0$) and/or finite energy spread ($K_\gamma \neq 0$), the collective response is exponentially damped due to the longitudinal thermal motion of the electrons, i.e. the oscillation frequency Ω has a finite negative imaginary part. This collisionless damping process is usually denoted Landau damping. The variational equations, in this case, have to be solved numerically. Figure 3.1 shows the oscillation frequency and the Landau damping constant, defined as $-\Im\{\Omega\}$, as a function of K_ϵ and K_γ for $D = \sqrt{2}$ and $K_\beta >> 1$. Note that the response is radically different depending on the sign of K_ϵ. For positive K_ϵ, which corresponds to a forward propagating wave, the damping constant has a very weak dependence on the emittance parameter whereas for $K_\epsilon < 0$, corresponding to a backward propagating wave, it grows rapidly, reaching values of order 1 for $K_\epsilon \simeq -0.5$. This feature is quite general and does not depend on one particular choice of D or K_β.

The physical explanation of this anisotropy is the following: the electron longitudinal velocity shift due to emittance is always negative, or, in other words, the spread in longitudinal velocity in the beam is larger for negative velocities than for positive velocities, where negative and positive velocities are defined relatively to the reference particle traveling at $\beta_z = \sqrt{1 - 1/\gamma^2}$. Since Landau damping becomes important when the phase velocity of the plasma wave is comparable to the thermal velocity spread, waves that propagate in the forward direction (again, relatively to the reference particle) are less attenuated than waves that propagate in the backward direction. One consequence of this is that a sinusoidal density perturbation in z (which contains both a positive and a negative wavenumber k_z) gives rise to a stationary plasma wave for small values of K_ϵ and to a forward propagating plasma wave for $|K_\epsilon| \simeq 1$.

Emittance induced Landau damping can be an important parasitic effect in space-charge based experiments. In fact, in these scenarios, it is generally desirable to focus the beam to a tight spot in order to increase the beam density and enhance the collective response of the electrons (namely to increase the plasma oscillation frequency). However, in a non-accelerating beam, the geometrical emittance $\epsilon = k_\beta \sigma_x^2 = \sigma_x \sigma_\beta$ is a constant of the motion. This means that increasing the beam density comes at the cost of increasing the longitudinal velocity spread due to emittance, thus inducing Landau damping (since $K_\epsilon \propto \epsilon^2/\sigma_x$). It follows that, for a given beam emittance, the beam density has an optimum value for achieving the strongest plasma response, which is ultimately determined by the emittance parameter K_ϵ. Beam optimization for space-charge based experiments is currently under intense investigation and the application of the present

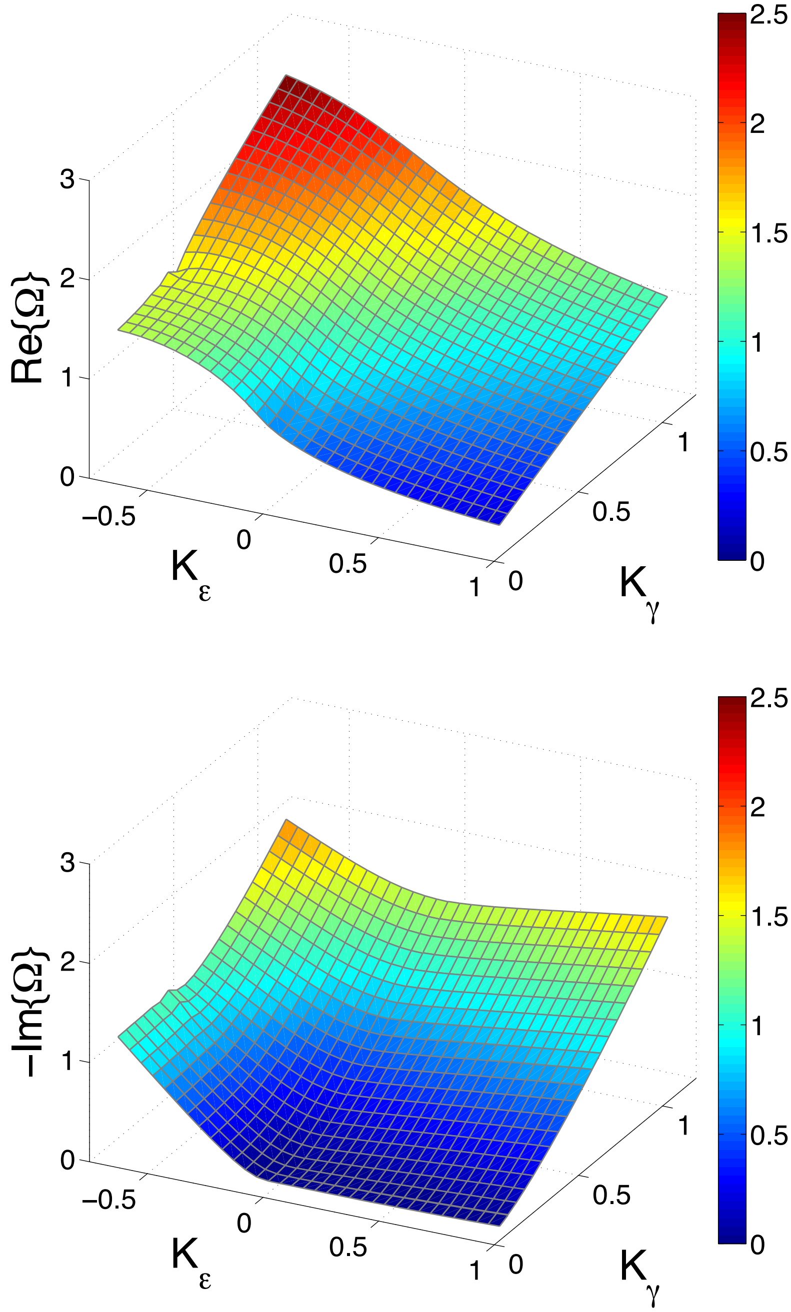

Figure 3.1: Oscillation frequency (upper plot) and Landau damping constant (bottom plot) as a function of the energy spread (K_γ) and emittance parameter (K_ϵ) for $D = \sqrt{2}$ and $K_\beta >> 1$.

theory to this topic will be the subject of a subsequent publication.

3.4 The exact dispersion relation in the spatial frequency domain: limiting forms and physical interpretation

The plasma oscillation eigenmodes can be found, in principle, by solving Eq.(3.10) for Ω and E_z. In the previous section we have found approximate solutions to the dispersion equation using a variational approach. To find solutions to the exact dispersion relation, however, it is more convenient to write Eq.(3.10) in a different form, which is more fit for a numerical solution with a discretization method. For this purpose we first expand the electric field in a series of azimuthal modes, i.e. we find solutions in the form $E_z = E_m(R)e^{im\phi}$, where R and ϕ represent the position in the transverse plane in polar coordinates. Finally we perform a Hankel transform of the resulting expression, defined as $H_m(F) = \int_0^\infty F(R)J_m(QR)RdR$, where J_m is the m-th order Bessel function of the first kind. The details of the derivation are contained in the Appendix, the resulting dispersion relation is:

$$\hat{E}_m(Q) = \int_0^\infty T_m(Q,Q')\hat{E}_m(Q')Q'dQ' \tag{3.22}$$

where the integration kernel T_m is:

$$T_m(Q,Q') = \frac{1}{1+\frac{Q^2}{D^2}} \int_{-\infty}^0 \frac{T}{(1+iK_\epsilon T)^2} I_m\left(\frac{QQ'\cos K_\beta T}{1+iK_\epsilon T}\right) e^{-\frac{(K_\gamma T)^2}{2} - i\Omega T - \frac{Q^2+Q'^2}{2(1+iK_\epsilon T)}} dT \tag{3.23}$$

where I_m is the m-th order modified Bessel function of the first kind. The solutions to Eq.(3.22) provide the eigenvalue Ω and the eigenmode $\hat{E}_m$ in the frequency domain. The eigenmode in the space domain can be recovered by inverting the Hankel transform as: $E_m(R) = \int_0^\infty \hat{E}_m(Q) J_m(QR) Q dQ$.

To explain some important physical aspects of the problem we derive the limiting forms of Eq.(3.22) in the case of a cold beam ($K_\gamma << 1, K_\epsilon << 1$) for both the laminar beam ($K_\beta << 1$) and the high betatron frequency ($K_\beta >> 1$) limits.

For the laminar beam limit $K_\beta << 1$ the dispersion relation reduces to:

$$\hat{E}_{m,r}(Q) = \frac{1}{\Omega^2(1+\frac{Q^2}{D^2})} \int_0^\infty I_m(QQ')\, e^{-\frac{Q^2+Q'^2}{2}} \hat{E}_{m,r}(Q') Q' dQ'. \tag{3.24}$$

Note that for a given eigenmode $\hat{E}_m(Q)$ there are two associated eigenvalues $\pm\Omega$ which means that the general response in this limit is that of a stationary oscillation.

In the case of a cold beam in the high betatron frequency limit $K_\beta >> 1$, it is convenient to perform a Fourier expansion of the integration kernel in the betatron phase $K_\beta T$. The resulting integration kernel is:

$$T_m(Q,Q') = \frac{e^{-\frac{Q^2+Q'^2}{2}}}{\left(1+\frac{Q^2}{D^2}\right)} \sum_n I_{\frac{m+n}{2}}\left(\frac{QQ'}{2}\right) I_{\frac{m-n}{2}}\left(\frac{QQ'}{2}\right) \frac{1}{(\Omega - nK_\beta)^2} \tag{3.25}$$

where the sum is performed over all even/odd integers n for an even/odd azimuthal number m (see the derivation in the Appendix).

Note that each term in the summation in Eq.(3.25) is associated to a harmonic of the betatron frequency nK_β. In particular, for an even/odd value of m, the dispersion relation couples to all even/odd harmonics of K_β and the integration kernel T_m is strongly peaked around $\Omega \approx nK_\beta$ irrespective of its dependence on (Q, Q'). This has an interesting physical interpretation: as the beam goes

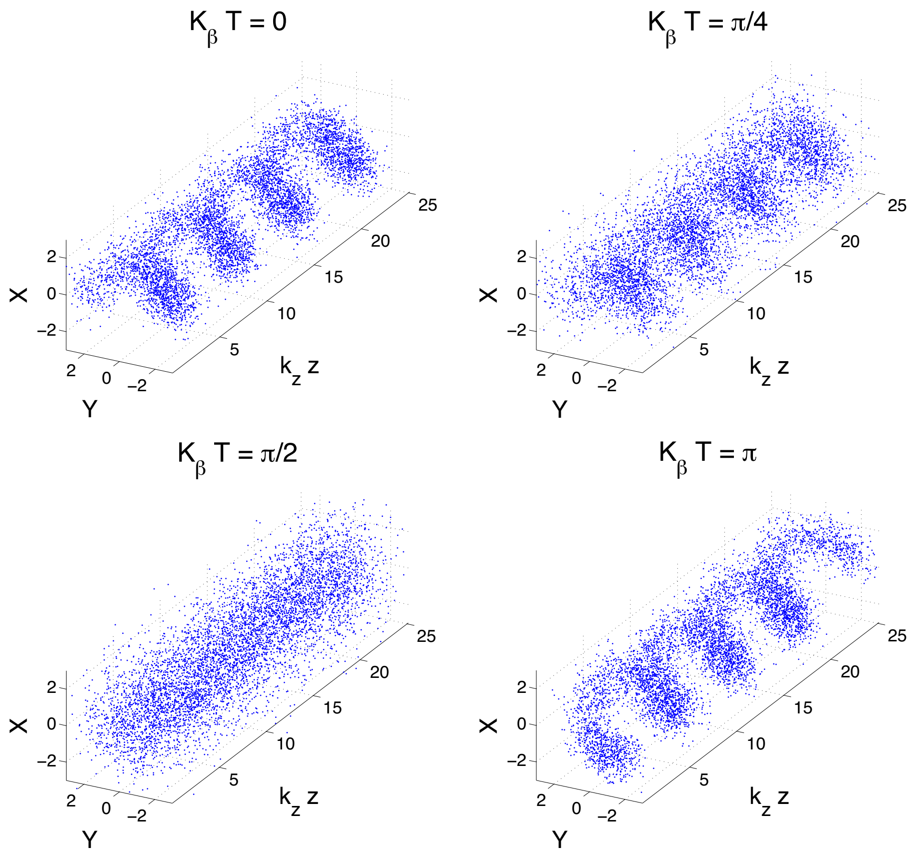

Figure 3.2: Ballistic evolution of a helical charge density perturbation corresponding to an $m = 1$ transverse mode.

through half a betatron oscillation period, the transverse positions of all the electrons are mirrored in x and y across the z-axis. For a charge perturbation of the form $\propto e^{im\phi}$, mirroring the positions of all the electrons results in a new charge perturbation with the same radial and azimuthal dependence multiplied by a factor $e^{im\pi}$. This means that the density perturbation replicates itself every half betatron oscillation period, unchanged for even m and with a negative sign for odd m (see Fig. 3.2 for a visual example of this effect). It follows that, under the effect of transverse focusing, the evolution of an even/odd m mode is periodic and composed of even/odd harmonics of the betatron frequency K_β. Recall that in our linear analysis, the particle's response to the collective field is computed as a small perturbation to the zeroth order trajectories. Since the zeroth order motion of the electrons drives an oscillation of the field at the even/odd harmonics of K_β (for an even/odd value of m), it follows that only these harmonics will couple to an even/odd m plasma eigenmode through the dispersion relation.

Since the integration kernel in Eq.(3.25) is highly peaked around the harmonics of the betatron frequency, we will look for solutions in the form $\Omega = hK_\beta + \delta\Omega$ with $\delta\Omega << K_\beta$, where h is either an even integer (for even m) or an odd integer (for odd m). With this ansatz, we neglect all the terms corresponding to harmonics different than h and the dispersion relation is further simplified:

$$\hat{E}_{m,h,r}(Q) = \frac{1}{\delta\Omega^2\left(1+\frac{Q^2}{D^2}\right)} \int_0^{+\infty} e^{-\frac{Q^2+Q'^2}{2}} I_{\frac{m+h}{2}}\left(\frac{QQ'}{2}\right) I_{\frac{m-h}{2}}\left(\frac{QQ'}{2}\right) \times \hat{E}_{m,h,r}(Q')Q'dQ'. \tag{3.26}$$

In this case, for the same eigenfunction, the corresponding oscillation frequencies are: $\Omega = \pm(hK_\beta \pm \delta\Omega)$. For $h = 0$ the plasma oscillation frequency contains the collective response of the electrons averaged over the betatron motion. For $h \neq 0$, instead, this set of solutions corresponds to a beatwave, with a fast betatron oscillation modulated by the slow collective response described by the eigenvalue $\delta\Omega$ and we will denote it Plasma-Betatron Beatwave (PBW). Figure 3.3 shows a schematic representation of the evolution of a PBW mode.

Mathematically, the beat happens between the two eigenfrequencies of the system $hK_\beta \pm \delta\Omega$ which, for $K_\beta >> 1$, differ by a small value $2\delta\Omega$. Physically this effect can be explained as follows: consider for simplicity an odd m mode. The ballistic evolution (i.e. with no collective fields) of the mode is periodic and composed of odd harmonics of the betatron oscillation frequency. In the $K_\beta >> 1$ limit, the time-scale associated with the plasma oscillation is much larger than the betatron oscillation period and the exchange between energy and density modulation, which causes the plasma oscillation, happens in several betatron periods. Since betatron motion drives a fast oscillation of the electric field at the odd harmonics of the betatron frequency and the plasma oscillation has a time scale that is larger than the betatron period, the mode evolution is composed of the fast ballistic evolution driven by betatron motion (at the characteristic frequency hK_β), modulated in time by the slow collective plasma oscillation (with frequency $\delta\Omega$). The same argument can be used for even m modes for harmonics of the betatron frequency different than zero.

It is very important to emphasize that, in the $K_\beta >> 1$ limit, the collective physics is contained in the reduced eigenvalue $\delta\Omega$. We will thus denote $\delta\Omega$ the effective plasma frequency. The eigenfrequency $\Omega = hK_\beta + \delta\Omega$, instead, describes the combined effects of zeroth order motion and collective response. In light of this, it is convenient to classify the modes differently in the two limits of laminar motion and high betatron frequency. In the first case, $K_\beta << 1$, the modes are

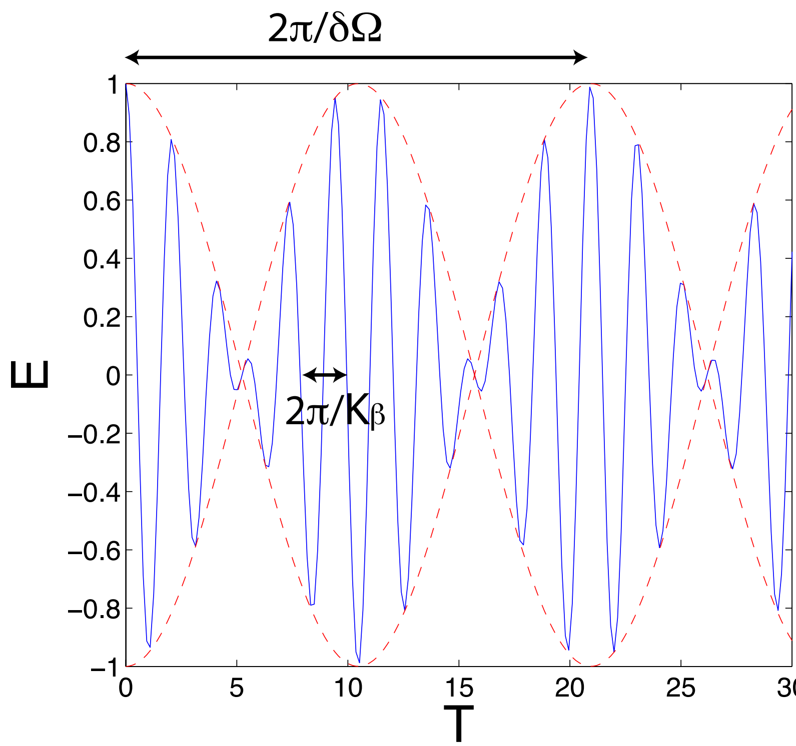

Figure 3.3: Schematics of the plasma-betatron beatwave mechanism. The blue line represents the time evolution of the electric field, the red dashed line shows the envelope of the beatwave, evolving according to the effective oscillation frequency $\delta\Omega$.

denoted as $E_{m,r}$ where m is the azimuthal number and r is the radial number, with the modes ordered in r by decreasing oscillation frequency Ω (i.e. the lowest order mode is the one with the highest space-charge oscillation frequency). In the $K_\beta >> 1$ case, instead, the modes are naturally identified by their relationship to the discrete harmonic of the betatron oscillation frequency. The modes are then denoted $E_{m,h,r}$ where h is the associated harmonic number and the modes are ordered in the radial index r by decreasing $\delta\Omega$. The fundamental mode discussed in Section 3.3, for example, is identified as the $E_{0,0}$ mode for $K_\beta << 1$ or the $E_{0,0,0}$ mode for $K_\beta >> 1$. Note that for even m modes, $h = 0$ is a valid harmonic number whereas for odd m, the lowest possible harmonic number is $h = 1$, which means that in the $K_\beta >> 1$ limit odd m modes only exist in the form of PBWs.

Finally we observe that, by comparing Eq.(3.26) and Eq.(3.25), follows that the condition under which the high betatron frequency limit is approached can be relaxed. For a given value of $\delta\Omega$, the condition for having a PBW is that $\delta\Omega^2 << 4K_\beta^2$ which, in many cases, holds even for values of K_β of order 1.

3.5 Eigenvalues and eigenmodes of the exact dispersion relation

In this section we find numerical solutions to the exact dispersion relation to give a quantitative description of the effects described in the previous section. We will be concerned with the cold beam limit ($K_\gamma << 1$, $K_\epsilon << 1$). In this limit, the two parameters of interest are the 3-D parameter D and the normalized betatron frequency K_β, we will thus explore the behavior of the plasma oscillation as a function of D in the two important cases of laminar motion $K_\beta << 1$ and high betatron frequency $K_\beta >> 1$.

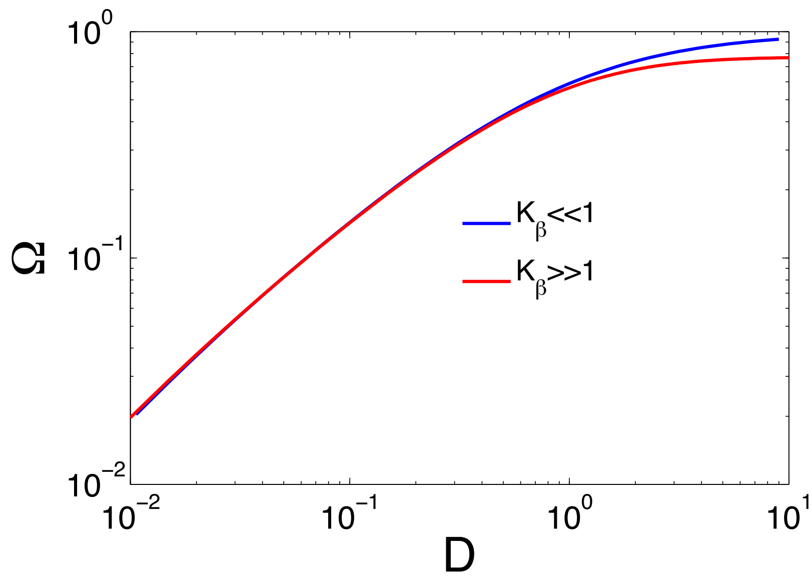

Figure 3.4: Fundamental mode oscillation frequency as a function of D for the laminar beam limit (blue curve) and for the high betatron frequency limit (red curve) as found with the matrix method for a cold beam.

Eq.(3.22) can be solved numerically by discretizing Q and Q'. Upon discretization, the integral equation becomes a matrix equation[10]:

$$M_{q,q'}(\Omega)\hat{E}_{q'} = 0. \tag{3.27}$$

Eq.(3.27) has non-trivial solutions only if $\det(M_{q,q'}(\Omega)) = 0$. The zeroes of the determinant and the matrix eigenvectors represent the eigenvalue/eigenmode pairs for the plasma oscillation modes.

Figure 3.4 shows the solutions to the exact dispersion relation for the cold beam case in the laminar beam limit and the high betatron frequency limit as a function of D for the fundamental $m = 0$ mode, compared to solutions from the variational approach (shown as dashed lines). The solutions to the exact dispersion relation confirm, with a good approximation, the results from the variational method: in the laminar beam case, the oscillation frequency approaches the 1-D limit $\Omega = \pm 1$ as $D \to \infty$, whereas, for $K_\beta >> 1$ the oscillation frequency reaches a smaller value $\Omega \simeq \pm 0.756$ due to the effect of betatron motion. As D decreases the oscillation frequency decreases monotonically, asymptotically approaching 0 as $D \to 0$ in both cases.

Figure 3.5 shows the mode profile for the fundamental $m = 0$ mode for several values of the 3-D parameter. For $D = 0.1$ the mode profile extends well beyond the beam distribution, while for $D = 10$ it is confined within the beam. This can be understood by considering the field distribution as a convolution between the perturbed charged distribution (which is typically confined within the beam) and the single particle longitudinal electric field. Since for $D << 1$ the single particle field extends well beyond the 0-th order charge distribution (see the discussion on the D parameter in Section 3.1.1), its convolution with the perturbed charge distribution has a transverse profile which is significantly broader than the beam size. Figure 3.5 also shows the transverse profile of three higher order radial modes for $D = 1$ and $K_\beta >> 1$.

Finally, we illustrate the effect of betatron oscillations on the higher order modes. Fig. 3.6 shows the effective oscillation frequency for the lowest order $m = 1$ and $m = 2$ modes in both the laminar beam limit ($K_\beta << 1$) and the high betatron frequency limit ($K_\beta >> 1$) as a function of the 3-D parameter D. Note that in the $D >> 1$ limit, for $K_\beta << 1$, all the eigenvalues tend to the one-dimensional limit $\Omega = 1$, as predicted in section 3.1 by taking the one-dimensional limit of the dispersion relation. For $K_\beta >> 1$, instead, transverse focusing breaks the degeneracy of the different azimuthal modes for $D >> 1$. Also, comparing the solutions for the laminar beam to the ones for the high betatron frequency limit, we conclude that the suppression of the collective response due to betatron

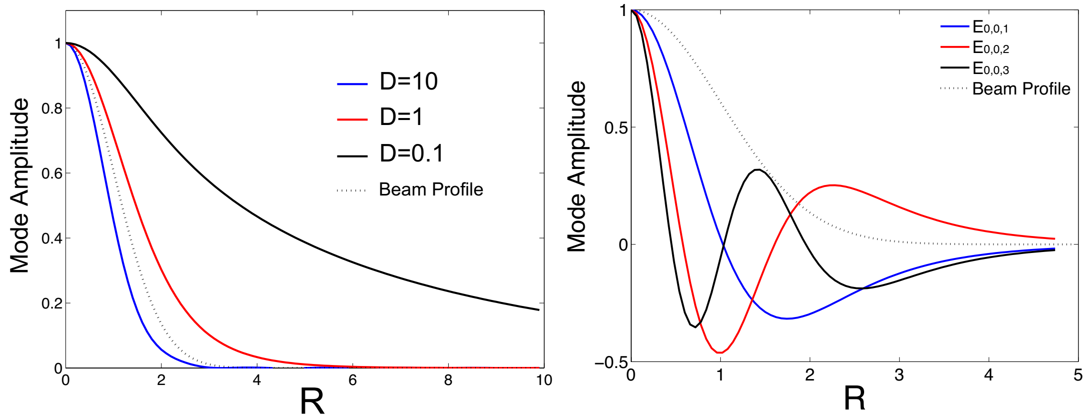

Figure 3.5: Left figure: Mode profile for the fundamental $m = 0$ mode, for $K_\beta >> 1$ and $D = 10$ (blue curve), $D = 1$ (red curve), $D = 0.1$ (black curve). Right figure: Mode profile for the three higher order radial modes for $D = 1$ and $K_\beta >> 1$. For comparison, the beam density profile is plotted as a black dotted line.

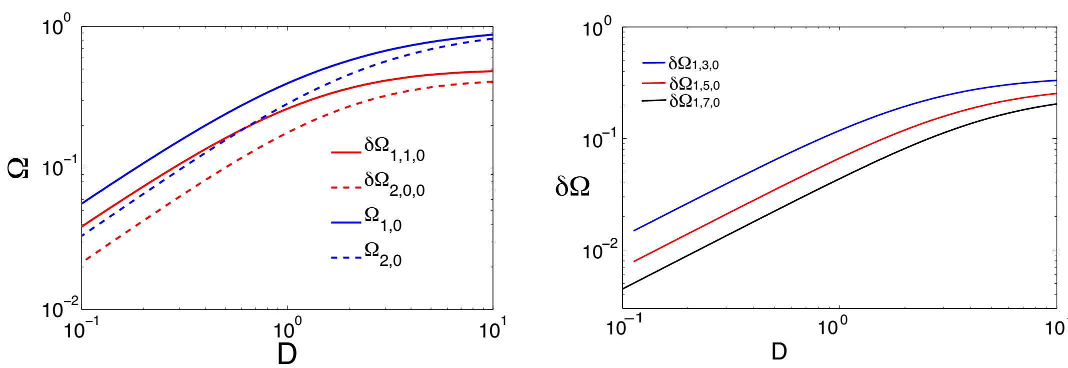

Figure 3.6: Lef figure: Effective plasma oscillation frequency $\delta\Omega$ as a function of D for the $E_{1,1,0}$ (red solid line) and $E_{2,0,0}$ (red dashed line) modes for $K_\beta >> 1$. The blue lines show the oscillation frequency Ω for the corresponding eigenmodes in the laminar beam limit ($K_\beta << 1$), i.e. the $E_{1,0}$ (blue solid line) and $E_{2,0}$ (blue dashed line) modes. Right figure: Effective plasma oscillation frequency for the plasma-betatron beatwave modes associated with the 3rd 5th and 7th harmonic for m=1 and for the lowest order of radial mode.

motion is much stronger for the higher order modes compared to the fundamental $m = 0$ mode (compare Figs. 3.4 and 3.6). Also, suppression of the higher order modes due to transverse focusing happens over a broad range of values of D, including the limit for $D << 1$, in which the fundamental mode is unaffected by transverse motion. Figure 3.6 also shows the effective oscillation frequency $\delta\Omega$ for the third, fifth and seventh harmonics of the betatron frequency K_β for $m = 1$, indicating that the collective response is slower for higher harmonics.

This has strong implications from the experimental point of view. Space-charge based amplifiers [13] can benefit from the suppression of higher order modes in terms of increased transverse coherence when starting from shot-noise. In addition to that, the strong separation in oscillation frequency of the different eigenmodes could be used as a tool for selective microbunching amplification. In fact, since microbunching amplification is maximized when the beam drifts for one-quarter plasma oscillation, optimum amplification happens at different points along the beamline for different transverse modes. This effect could be used, for example, as a low noise preamplifier in a High Gain High Mode Generation free-electron laser scheme for the production of orbital angular momentum modes[44].

3.6 Conclusions

In this chapter we have studied the properties of longitudinal plasma waves in a thermal relativistic electron beam. This analysis addresses an eigenmode/eigenvalue problem and provides a set of propagating space-charge modes and their associated oscillation frequencies.

We have derived a three-dimensional dispersion relation for the longitudinal plasma oscillation modes. The dispersion relation can be expressed in terms of four dimensionless scaling parameters and includes the effects of energy spread, finite emittance and betatron motion as well as edge effects due to the finite size of the beam.

The dispersion relation has been solved for a broad range of values of the dimensionless scaling parameters using both a variational approach and a discretization method. The results have been used to describe several novel physical effects.

We have studied geometrical effects for the fundamental mode as well as for few higher order modes, showing how the plasma oscillation frequency is reduced with respect to the one-dimensional limit when the 3-D parameter $D = k\sigma_x/\gamma$ is of order 1 or smaller.

We demonstrate how the longitudinal velocity spread due to emittance induces an anisotropy between forward and backward propagating plasma waves, with a stronger Landau damping of backward propagating modes with respect to the forward propagating ones.

The effects of transverse focusing are also of great importance. We show how betatron motion breaks the degeneracy of the plasma modes in the infinite beam limit ($k\sigma_x/\gamma >> 1$) introducing a phase correlation of the electric field across the whole transverse plane, an effect that has practical consequences for shot-noise reduction schemes. Transverse focusing, coupled to the transverse structure of the plasma eigen-modes, also gives rise to a beatwave between plasma and betatron oscillations. This effect is denoted Plasma-Betatron Beatwave and consists of a fast oscillation of the electric field driven by betatron oscillations, superimposed to the slow collective response of the electrons. Finally, betatron oscillations are shown to suppress the collective response of the beam, an effect that is particularly noticeable for higher order modes, with important consequences for space-charge based amplifiers.

3.A Mathematical derivations and useful formulas

In this appendix we derive some of the formulas discussed in the text.

3.A.1 Relationship to the plasma dispersion function

We start by casting the following relationship, which should clarify the connection of our approach to some of the previous literature:

$$\int_{-\infty}^{0} T e^{-i\Omega T - \frac{K^2 T^2}{2}} dT = i\frac{d}{d\Omega}\int_{-\infty}^{0} e^{-i\Omega T - \frac{K^2 T^2}{2}} dT = \frac{1}{2K^2} Z'\left(\frac{\Omega}{\sqrt{2}K}\right) \tag{3.28}$$

where Z' is the complex derivative of the plasma dispersion function Z. The plasma dispersion function can be defined in two equivalent ways:

$$Z(\zeta) = \frac{1}{\sqrt{\pi}}\int_{\tilde{c}} dx \frac{e^{-x^2}}{x-\zeta} = 2ie^{-\zeta^2}\int_{-\infty}^{i\zeta} e^{-x^2} dx \tag{3.29}$$

where $\tilde{c}$ stands for the Landau contour which runs in the complex plane from $-\infty$ to $+\infty$ and below the singularity at $x = \zeta$. The equivalence between the two formulas is derived in [4]. For $|\zeta| >> 1$ we have $Z'(\zeta) \approx 1/\zeta^2$. It follows that for $K_\gamma << 1$ the time integral in Eq.(3.28) reduces to:

$$\int_{-\infty}^{0} T e^{-i\Omega T - \frac{K^2 T^2}{2}} dT \approx \frac{1}{\Omega^2} \tag{3.30}$$

3.A.2 Azimuthal mode expansion and Hankel transform

To derive Eq.(3.22) we start by performing the azimuthal mode expansion of the dispersion relation. Using the relation $e^{\zeta cos(\phi)} = \sum_{m=-\infty}^{\infty} I_m(\zeta) e^{im\phi}$ we get:

$$\left(\frac{d}{D^2RdR}(R\frac{d}{dR})-\frac{m^2}{D^2R^2}-1\right)E_m=-\int_0^\infty E_m(R')G_m(R,R')R'dR' \qquad (3.31)$$

with:

$$G_m(R,R')=\int_{-\infty}^0 e^{-\frac{(K_\gamma T)^2}{2}-i\Omega T}e^{-\frac{\left(R^2+R'^2\right)(1+iK_\epsilon T)}{2\sin^2 K_\beta T}}I_m\left(\frac{RR'(1+iK_\epsilon T)\cos K_\beta T}{2\sin^2 K_\beta T}\right)\frac{T}{\sin^2 K_\beta T}dT. \qquad (3.32)$$

Finally, the Hankel transform of Eq.(3.31) can be performed using the following formulas: $\int_0^\infty xe^{-\alpha x^2}I_\nu(\beta x)J_\nu(\gamma x)dx=\frac{1}{2\alpha}e^{\frac{\beta^2-\gamma^2}{4\alpha}}J_\nu(\frac{\beta\gamma}{2\alpha})$ and $\int_0^\infty xe^{-\alpha x^2}J_\nu(\beta x)J_\nu(\gamma x)dx=\frac{1}{2\alpha}e^{-\frac{\beta^2+\gamma^2}{4\alpha}}I_\nu(\frac{\beta\gamma}{2\alpha})$.

3.A.3 Limiting forms of the dispersion relation

Eq.(3.24), which represents the limiting form of Eq.(3.22) for a cold, laminar beam can be obtained by setting $K_\beta\to 0$ and $K_\epsilon\to 0$ and using Eq.(3.28) to compute the integral in T:

$$\hat{E}_{m,r}(Q)=\frac{Z'(\frac{\Omega}{\sqrt{2}K_\gamma})}{2K_\gamma^2(1+\frac{Q^2}{D^2})}\int_0^\infty I_m\left(QQ'\right)e^{-\frac{Q^2+Q'^2}{2}}\hat{E}_{m,r}(Q')Q'dQ' \qquad (3.33)$$

and finally using Eq.(3.30) to take the limit for $K_\gamma\to 0$.

Eq.(3.25) can be derived by using the formula $\int_0^{\pi/2}I_{\mu+\nu}(2a\cos x)cos[(\mu-\nu)x]dx=\frac{\pi}{2}I_\mu(a)I_\nu(a)$. We obtain the following Fourier expansion:

$$I_m(QQ'\cos K_\beta T) = \sum_{n=-\infty}^{+\infty} e^{+2inK_\beta T} I_{\frac{m}{2}+n}\left(\frac{QQ'}{2}\right) I_{\frac{m}{2}-n}\left(\frac{QQ'}{2}\right) \tag{3.34}$$

for even m and:

$$I_m(QQ'\cos K_\beta T) = \sum_{n=-\infty}^{+\infty} e^{+i(2n+1)K_\beta T} I_{\frac{m+1}{2}+n}\left(\frac{QQ'}{2}\right) I_{\frac{m-1}{2}-n}\left(\frac{QQ'}{2}\right) \tag{3.35}$$

for odd m.

The resulting integration kernel is:

$$T_m(Q,Q') = \frac{e^{-\frac{Q^2+Q'^2}{2}}}{2K_\gamma^2\left(1+\frac{Q^2}{D^2}\right)} \sum_{n=-\infty}^{+\infty} I_{\frac{m}{2}+n}\left(\frac{QQ'}{2}\right) I_{\frac{m}{2}-n}\left(\frac{QQ'}{2}\right) Z'\left(\frac{\Omega - 2nK_\beta}{\sqrt{2}K_\gamma}\right) \tag{3.36}$$

for even m and:

$$T_m(Q,Q') = \frac{e^{-\frac{Q^2+Q'^2}{2}}}{2K_\gamma^2\left(1+\frac{Q^2}{D^2}\right)} \sum_{n=-\infty}^{+\infty} I_{\frac{m+1}{2}+n}\left(\frac{QQ'}{2}\right) I_{\frac{m-1}{2}-n}\left(\frac{QQ'}{2}\right) Z'\left(\frac{\Omega - (2n+1)K_\beta}{\sqrt{2}K_\gamma}\right) \tag{3.37}$$

for odd m. Eqs. (3.36,3.37) reduce to (3.25) for $K_\gamma \to 0$.

CHAPTER 4

Initial value problem of space-charge waves in six-dimensional phase-space

In chapter 3, the propagation of plasma waves in a relativistic electron beam was tackled in the context of and eigenvalue problem. While the solution to the eigenvalue problem provides a set of steady-state solutions to the coupled Vlasov/Poisson equations, the self-consistent evolution of an arbitrary initial phase-space perturbation under the effects of longitudinal space-charge forces is yet to be addressed. The latter problem is defined as the initial value problem (IVP) of space-charge waves and this chapter is devoted to its solution.

The IVP of longitudinal plasma oscillations in high brightness electron beams was previously solved in [22] for the case of a cold laminar beam whereas the effects of transverse and longitudinal velocity spread were discussed in [30] with a quasi-three-dimensional approach. In both cases the analysis was based on the Laplace transform method. However, when transverse betatron oscillations and finite beam emittance are included, the coupling of the plasma eigenmodes to the initial perturbation is challenging and the methods based on the Laplace/Fourier transforms become highly impractical. In this chapter, the IVP is solved by means of a bi-orthogonal mode expansion in six-dimensional phase space. Our analysis follows the approach of Kim [40], Xie [45] and Huang [46] for the grand initial value problem of free electron lasers in three-dimensions.We develop a general formalism for the solution of the plasma oscillation problem in terms of the eigenmodes of a Schrödinger-like equation in six-dimensional phase space. The difficulty of the problem lies in the non-orthogonality of the plasma eigenmodes. The IVP is solved by projecting the initial value onto the plasma eigenmodes with the aid of the property of bi-orthogonality with respect to the set of adjoint eigenmodes, a method which is generally referred to as Van Kampen mode expansion.

The chapter is organized as follows: in section 4.1 we develop the general formalism for the IVP in terms of phase-space eigenmodes. In section 4.2 we find explicit analytic solutions for the coupling of an initial coherent perturbation to the dominant fundamental plasma eigenmodes which we use to describe the time evolution of a coherent density modulation. In section 4.3 we discuss the coupling of the fundamental mode to shot-noise. Finally we discuss the application of this model to an experimental scenario and the implications of our theory for shot-noise reduction experiments.

This analysis was published in Ref. [47].

4.1 General formulation of the initial value problem

In this section we derive a general solution for the IVP of plasma oscillations. We work under the same assumptions as chapter 3: we assume a coasting, non-accelerating electron beam of energy γmc^2, matched to a uniform focusing channel of betatron frequency k_β/c. The electron beam is described in the six-dimensional phase-space by a distribution function $f(\vec{x}, \vec{\beta}_\perp, z, \eta, \tau)$ where $\vec{x}$ is the transverse position with respect to the propagation axis, $\vec{\beta}_\perp$ is the transverse velocity normalized to the speed of light, $\eta = \frac{\delta\gamma}{\gamma}$ is the relative energy deviation, z is the longitudinal position along the beam and $\tau = ct$ where t is the time variable and c is the speed of light. The distribution function is expanded to first order in perturbation theory: $f = f_0 + f_1 e^{ik_z z}$ where f_0 is a stationary distribution function and $|f_1| \ll f_0$. We assume the following form for the 0-th order distribution function $f_0 = n_0 e^{-\frac{\vec{x}^2}{2\sigma_x^2} - \frac{\vec{\beta}_\perp^2}{2\sigma_x^2 k_\beta^2} - \frac{\eta^2}{2\sigma_\eta^2}} / (2\pi)^{3/2} \sigma_x^2 k_\beta^2 \sigma_\eta$ where n_0 is the beam volume density on axis and σ_x is the root mean square (RMS) size of the matched charge distribution. The perturbed distribution function evolves according to the linearized Vlasov equation coupled to the Poisson equation:

$$\partial_\tau f_1 + \vec{\beta}_\perp \cdot \vec{\nabla}_{\vec{x}} f_1 - k_\beta^2 \vec{x} \cdot \vec{\nabla}_{\vec{\beta}_\perp} f_1 + i k_z \dot{z} f_1 + \frac{e\mathscr{E}_z}{\gamma m c^2} \partial_\eta f_0 = 0 \tag{4.1}$$

$$(\nabla_\perp^2 - \frac{k_z^2}{\gamma^2}) \frac{\mathscr{E}_z}{-\frac{ik_z}{\gamma}} = -\frac{e}{\gamma \epsilon_0} \int f_1 e^{ik_z z} d\eta d^2 \vec{\beta}_\perp \tag{4.2}$$

where $\dot{z} = \eta/\gamma^2 - (k_\beta^2 \vec{x}^2 + \vec{\beta}_\perp^2)/4$.

The initial value problem of plasma oscillations can be addressed by casting the system of equations that describe the plasma eigenvalue problem in the form of a Schrödinger-like equation:

$$\partial_\tau f_1 = L(f_1) \tag{4.3}$$

where L is a linear operator defined as:

$$L(f_1) = -(\vec{\beta}_\perp \cdot \vec{\nabla}_{\vec{x}} f_1 - k_\beta^2 \vec{x} \cdot \vec{\nabla}_{\vec{\beta}_\perp} f_1 + i k_z \dot{z} f_1 + \frac{e\tilde{\mathscr{E}}_z(f_1)}{\gamma m c^2} \partial_\eta f_0). \tag{4.4}$$

and $\tilde{\mathscr{E}}_z(f_1)$ is a linear operator which acts on f_1 to give the implicit solution to

Eqn. (4.2) via the Green's function method:

$$\tilde{\mathscr{E}}_z(f_1) = \int d\eta d^2\vec{\beta}_\perp d^2\vec{x}' f_1(\vec{x}', \vec{\beta}_\perp, \eta, \tau) E_{sp}(\vec{x} - \vec{x}') \tag{4.5}$$

with $E_{sp}(\vec{x}) = \frac{-ik_z e}{2\pi\gamma^2\epsilon_0} K_0\left(\frac{k_z|\vec{x}|}{\gamma}\right)$ being the single particle longitudinal electric field in the longitudinal frequency domain (see, for example [31]).

The eigenvalues and eigenfunctions of the L operator represent a set of solutions to the system of Vlasov-Maxwell's equations for the plasma oscillation problem. Namely, if $L(\hat{f}_n) = -i\frac{\omega_n}{c}\hat{f}_n$, then $\hat{f}_n e^{-i\frac{\omega_n\tau}{c}}$ is a solution to the plasma oscillation problem. The eigenmode of L associated with an eigenvalue ω_n is:

$$\hat{f}_n = -\frac{e}{\gamma mc^2}\partial_\eta f_0 \int_{-\infty}^{0} e^{-i\frac{\omega_n\tau}{c}+ik_z\dot{z}\tau} E_n\left(\vec{x}_+(\tau)\right) d\tau \tag{4.6}$$

where $\vec{x}_+(\tau) = \vec{x}\cos k_\beta\tau + \frac{\vec{\beta}_\perp}{k_\beta}\sin k_\beta\tau$ and E_n, ω_n are the solutions to the eigenvalue equation derived in chapter 3:

$$(\nabla_\perp^2 - \frac{k_z^2}{\gamma^2})E_n = -\frac{k_z^2\omega_p^2}{\gamma^2c^2}\int\int_{-\infty}^{0} \tau e^{-\frac{(k_z\sigma_\eta\tau)^2}{2\gamma^4} - ik_z\frac{k_\beta^2\vec{x}^2+\vec{\beta}_\perp^2}{4}\tau - i\frac{\omega_n\tau}{c}} E_n(\vec{x}_+(\tau)) f_{0\perp} d\tau d^2\vec{\beta}_\perp \tag{4.7}$$

with $f_{0\perp} = e^{-\frac{\vec{x}^2}{2\sigma_x^2} - \frac{\vec{\beta}_\perp^2}{2\sigma_x^2 k_\beta^2}}/2\pi\sigma_x^2 k_\beta^2$ and $\omega_p^2 = \frac{n_0e^2}{\epsilon_0\gamma^3 m}$ being the one-dimensional plasma oscillation frequency. We will denote $\hat{f}_n(\vec{x}, \vec{\beta}_\perp, \eta)$ the phase-space eigenmodes and $E_n(\vec{x})$ the field eigenmodes.

The initial value problem can be addressed by decomposing the initial perturbation $f_{1,0}$ in a sum of eigenmodes of L. For this purpose it is useful to define a scalar product in 5-dimensional phase space as:

$$\langle g, f\rangle = \int d\eta d^2\vec{\beta}_\perp d^2\vec{x} f(\vec{x}, \vec{\beta}_\perp, \eta, \tau) g(\vec{x}, \vec{\beta}_\perp, \eta, \tau). \tag{4.8}$$

With the above definitions, we can define an adjoint operator $L^\dagger$ associated with L as the operator that fulfills the following condition:

$$\langle g, L(f)\rangle = \langle L^\dagger(g), f\rangle. \tag{4.9}$$

Using elementary properties of the convolution operator, it is possible to show that $L^\dagger$ is given by:

$$L^\dagger(f_1) = -(-\vec{\beta}_\perp \cdot \vec{\nabla}_{\vec{x}} f_1 + k_\beta^2 \vec{x} \cdot \vec{\nabla}_{\vec{\beta}_\perp} f_1 + ik_z \dot{z} f_1 + \frac{e\tilde{\mathscr{E}}_z(f_1 \partial_\eta f_0)}{\gamma mc^2}). \tag{4.10}$$

The L operator is not self-adjoint, as a result its eigenvectors are not mutually orthogonal. However, it is a general property that the eigenvectors of a linear operator are mutually orthogonal to the eigenvectors of its adjoint operator. In our case we have: $\langle \hat{f}_m^\dagger, \hat{f}_n\rangle = \langle \hat{f}_n^\dagger, \hat{f}_n\rangle \delta_{n,m}$. It follows that, given an initial perturbation of the distribution function $f_{1,0}$, assuming that $\hat{f}_n$ is a complete set of eigenmodes [1], we have:

$$f_1(\tau) = \sum_n \hat{f}_n e^{-i\frac{\omega_n \tau}{c}} \frac{\langle \hat{f}_n^\dagger, f_{1,0}\rangle}{\langle \hat{f}_n^\dagger, \hat{f}_n\rangle}. \tag{4.11}$$

Eq. (4.11) describes the time evolution of a given initial perturbation $f_{1,0}$ in phase space under the effect of collective longitudinal space-charge forces. Note that for a cold beam, one field eigenmode can correspond to several eigenvalues [42]. For example, in the laminar beam limit there are two eigenvalues $\omega_\pm = \pm\omega$ for each field eigenmode E. In this case, the phase-space eigenmodes corresponding

[1]The completeness of this type of eigenmodes has not been demonstrated. However, it can be demonstrated from basic principles that a bi-orthogonal expansion minimizes the distance of the expanded solution to the real solution. We believe that this type of mode expansion gives an accurate description of collective effects but it misses some features due to single-particle poles, which become important in the evolution of shot-noise fluctuuations for warm beams.

to each eigenvalue

$$\hat{f}_{\pm} = -\frac{e}{\gamma mc^2}\partial_\eta f_0 \int_{-\infty}^{0} e^{-i\frac{\omega_{\pm}\tau}{c}+ik_z\dot{z}\tau} E\left(\vec{x}_{+}(\tau)\right) d\tau \tag{4.12}$$

are to be considered as distinct eigenmodes of the L operator and have to be accounted for individually in the eigenmode expansion of Eq.(4.11)

We now find explicit expressions for $\hat{f}_n^\dagger$ in terms of the LSC eigenmodes. Multiplying by $\partial_\eta f_0$ both sides of Eq. 4.10 we obtain that the eigenvalues of $L^\dagger$ correspond to those of L and that the eigenmodes are given by:

$$\hat{f}_n^\dagger = -\frac{e}{\gamma mc^2} \int_{-\infty}^{0} e^{-i\frac{\omega_n\tau}{c}+ik_z\dot{z}\tau} E_n^\dagger\left(\vec{x}_{-}(\tau)\right) d\tau, \tag{4.13}$$

where $\vec{x}_{-}(\tau) = \vec{x}\cos k_\beta\tau - \frac{\vec{\beta}_\perp}{k_\beta}\sin k_\beta\tau$ and $E_n^\dagger$ is a solution to the field dispersion relation in Eq.(3.8), corresponding to the eigenvalue ω_n. If ω_n is a non-degenerate eigenvalue then $E_n^\dagger = E_n$, as is the case for modes with radial symmetry. Modes with with azimuthal dependence of the type $E_z(\vec{x}) = R_{m,r}(|\vec{x}|)e^{im\phi}$ (where ϕ is the azimuthal angle in the transverse plane) are degenerate since the mode with opposite azimuthal dependence ($E_z(\vec{x}) = R_{m,r}(|\vec{x}|)e^{-im\phi}$) is also a solution to the field dispersion relation associated with the same eigenvalue. In this case the bi-orthogonality property is fulfilled by choosing: $E_n = R_{m,r}(|\vec{x}|)e^{im\phi} \leftrightarrow E_n^\dagger = R_{m,r}(|\vec{x}|)e^{-im\phi}$.

In what follows we will use the dimensionless variables and scaling parameters defined in [42]. We give the following definitions: $T = \frac{\omega_p\tau}{c}$, $\vec{X} = \vec{x}/\sigma_x$, $\vec{B} = \vec{\beta}_\perp/k_\beta\sigma_x$. We define the following independent dimensionless scaling parameters: $D = k_z\sigma_x/\gamma$ is the 3-D parameter and accounts for edge effects due to the finite size of the beam; $K_\gamma = k_z c\sigma_\eta/\omega_p\gamma^2$ is the energy spread parameter and corresponds to the ratio of the longitudinal wave-number k_z to the Debye wave-number associated with energy spread; $K_\epsilon = k_z c(k_\beta \sigma_x)^2/2\omega_p$ is the emittance parameter and it corresponds to the ratio of k_z to the Debye wave-number associated with emittance; $K_\beta = k_\beta c/\omega_p$ is the focusing parameter. Finally the mode oscillation frequency is normalized to the one-dimensional plasma frequency as $\Omega = \omega/\omega_p$.

4.2 Time evolution of a coherent density modulation

Equation (4.11), combined with Eqs. (4.6,4.13), formally solves the IVP of plasma oscillations. However, to develop an intuition on the physical processes involved, it is useful to study the evolution of some specific forms of the initial perturbation.

In particular we will study the evolution of the fundamental mode starting from a coherent density modulation. In what follows we will make use of the dominant pole approximation, i.e., we will only retain the two solutions to the dispersion equation with the lowest Landau damping constant $\hat{f}_\pm$, $\Omega_\pm$. The notation $\pm$ refers to the sign of the real part of the eigenvalue, corresponding to a forward or backward propagating wave depending on the sign of k_z (in particular, for positive k_z, Ω_+ corresponds to the forward propagating mode while Ω_- corresponds to the backward one). As was shown in [42], emittance induces an anisotropy between $f_\pm$, with the forward propagating mode having a smaller damping constant.

With the above definitions and assumptions, the fundamental mode phase-space perturbation generated by an initial perturbation $f_{1,0}$ is given by:

$$f_1(T) = \hat{f}_+ \frac{\langle \hat{f}_+^\dagger, f_{1,0}\rangle}{\langle \hat{f}_+^\dagger, \hat{f}_+\rangle} e^{-i\Omega_+ T} + \hat{f}_- \frac{\langle \hat{f}_-^\dagger, f_{1,0}\rangle}{\langle \hat{f}_-^\dagger, \hat{f}_-\rangle} e^{-i\Omega_- T}. \tag{4.14}$$

In [42], an approximate variational method for the plasma oscillation eigenvalue problem was developed. In the variational approach, the fundamental mode is approximated with a pure gaussian mode $E_z = e^{-w\vec{X}^2}$. The eigenvalue Ω and the variational parameter w are then computed by projecting the dispersion relation (3.8) on the gaussian mode and imposing the condition that the eigenvalue be stationary as a function of w, i.e. $\frac{d\Omega}{dw} = 0$. Note that, in general, the field eigenmodes corresponding to the forward and backward propagating waves are different (except for the case of a cold beam, as discussed in section 4.1). Consequently the variational condition has to be applied separately for the two modes: $\frac{d\Omega_\pm}{dw_\pm} = 0$

The normalization coefficient for the fundamental mode can be computed explicitly in the variational approximation. With this simple form for the electric field the normalization coefficient $\langle \hat{f}^\dagger_\pm, \hat{f}_\pm \rangle$ can be expressed, in dimensionless units, as (see the derivation in the Appendix)):

$$\langle \hat{f}^\dagger_\pm, \hat{f}_\pm \rangle = \frac{ikn_\lambda c^3}{\gamma^2 \omega_p^3} \int_{-\infty}^{0} dT \frac{T^2 e^{-i\Omega_\pm T - \frac{(K_\gamma T)^2}{2}}}{(1 + iK_\epsilon T)^2 + 4w_\pm(1 + iK_\epsilon T) + 4w_\pm^2 \sin^2 K_\beta T} \tag{4.15}$$

where $n_\lambda = n_0 2\pi\sigma_x^2$ is the average linear beam density and we have omitted the factor $-e/\gamma mc^2$ from $\hat{f}_\pm$ and $\hat{f}^\dagger_\pm$, since it appears in both the numerator and the denominator of all the terms in Eq.(4.14).

To find a closed form expression for the coupling coefficient $\langle \hat{f}^\dagger_\pm, f_{1,0} \rangle$, one has to make some assumptions on the initial phase space perturbation. In this section we will discuss the case of a coherent density modulation, which can be generated, for example, through the interaction of the electrons with a resonant external radiation source in an undulator or by illuminating a photo-cathode with a laser pulse with an amplitude modulation [39]. For a coherent density modulation we have: $f_{1,0} = \tilde{\rho}(\vec{x}) f_0(\vec{x}, \vec{\beta}_\perp, \eta)$. We will also assume that the input bunching factor has a gaussian shape: $\tilde{\rho} = \frac{\tilde{n}_0}{n_\lambda}(1+2\nu)e^{-\nu \vec{X}^2}$, where $\tilde{n}_0 = \int d\eta d^2\vec{\beta}_\perp d^2\vec{x} f_{1,0}$ is the amplitude of the initial density perturbation and $\nu = \sigma_x^2/\sigma_b^2$ with σ_b equal to the RMS transverse size of the charge perturbation $\tilde{\rho}$. The resulting coupling coefficient is:

$$\langle \hat{f}_\pm^\dagger, f_{1,0} \rangle = \tilde{n}_0(1+2\nu)\frac{c}{\omega_p}\int_{-\infty}^{0} dT \frac{e^{-i\Omega_\pm T - \frac{(K_\gamma T)^2}{2}}}{(1+iK_\epsilon T)^2 + 2(w_\pm + \nu)(1+iK_\epsilon T) + 4w_\pm \nu \sin^2 K_\beta T}. \tag{4.16}$$

Equations (4.15) and (4.16), solve the initial value problem for the fundamental mode in the variational approximation, starting from a transversely gaussian density perturbation. To quantitatively describe the evolution of the plasma eigenmode we define the density modulation corresponding to the fundamental mode as:

$$\tilde{n} = \int d\eta d^2\vec{\beta}_\perp d^2\vec{x} f_1. \tag{4.17}$$

Note that, up to a factor $\frac{1}{n_\lambda}$ this definition is equivalent to that of the bunching factor commonly used in free-electron laser theory. Following this definition and using the results in Eqs.(4.15,4.16), the time evolution of the fundamental mode longitudinal density modulation, starting from a coherent seed, is given by:

$$\begin{aligned} \tilde{n} = -\frac{ik_z n_\lambda c^2}{\gamma^2\omega_p^2}\Bigg(& e^{-i\Omega_+ T}\frac{\langle \hat{f}_+^\dagger, f_{1,0}\rangle}{\langle \hat{f}_+^\dagger, \hat{f}_+\rangle}\int_{-\infty}^{0} dT' \frac{T' e^{-i\Omega_+ T' - \frac{(K_\gamma T')^2}{2}}}{(1+iK_\epsilon T')^2 + 2w_+(1+iK_\epsilon T')} \\ & + e^{-i\Omega_- T}\frac{\langle \hat{f}_-^\dagger, \hat{f}_{1,0}\rangle}{\langle \hat{f}_-^\dagger, \hat{f}_-\rangle}\int_{-\infty}^{0} dT' \frac{T' e^{-i\Omega_- T' - \frac{(K_\gamma T')^2}{2}}}{(1+iK_\epsilon T')^2 + 2w_-(1+iK_\epsilon T')}\Bigg) \end{aligned} \tag{4.18}$$

In the cold beam limit ($K_\gamma \ll 1, K_\epsilon \ll 1$) we have $\Omega_\pm = \pm\Omega$, $w_\pm = w$,

$\Im\{\Omega\} = 0$ and $\Im\{w\} = 0$ and Eq. (4.18) reduces to:

$$\tilde{n} = \tilde{n}_0 \Gamma \cos \Omega T \tag{4.19}$$

where $\tilde{n}_0$ is the initial value of the density perturbation and the geometrical coupling factor is $\Gamma = \frac{1+2\nu}{1+2(w+\nu)} \frac{1+4w}{1+2w}$ for $K_\beta \ll 1$ and $\Gamma = \frac{(1+2\nu)(1+4w+2w^2)}{(1+2(w+\nu)+2w\nu)(1+2w)}$ for $K_\beta \gg 1$.

Note that Eq.(4.18) only contains the response of the electrons coupled to the fundamental mode. A more realistic description of the system should take into account several transverse modes. For many applications, however, we are mostly concerned with the evolution of the fundamental mode since it is the one with the strongest collective response from the electrons.

Figure 4.1 shows the geometrical coupling coefficient Γ as a function of D and ν for both the laminar beam limit ($K_\beta \ll 1$) and the high betatron frequency limit ($K_\beta \gg 1$). Note how $\Gamma \neq 1$, which means that this type of initial perturbation excites several higher order radial modes other than the fundamental one.

4.3 Plasma dynamics of shot-noise

In a relativistic electron beam, the intrinsic discreteness of the particle distribution gives rise to a density perturbation commonly referred to as shot-noise. The density modulation induced by shot-noise can be expressed as:

$$\tilde{n}_{sn} = \frac{1}{L} \sum_j e^{-ik_z z_j} \tag{4.20}$$

where z_j is the longitudinal position of the j-th electron and the sum is performed over the N particles in the region $0 < z < L$. If the electrons are randomly

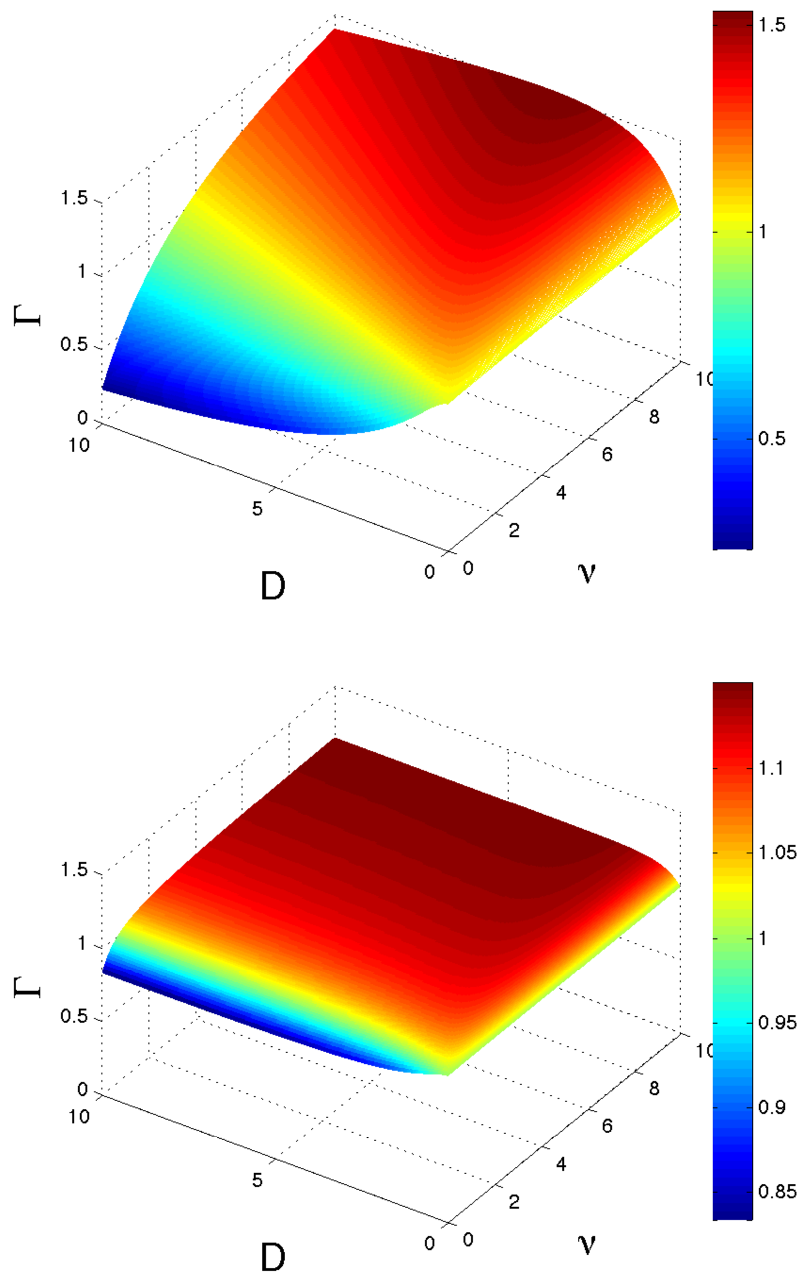

Figure 4.1: Geometrical coupling coefficient for a coherent gaussian density perturbation Γ for the laminar beam limit (upper plot) and the high betatron frequency limit (bottom plot) as a function of D and ν.

distributed the statistical average of $\tilde{n}_{sn}$ vanishes but the absolute value squared has a non vanishing average value $\overline{|\tilde{n}_{sn}|^2} = \frac{n_\lambda}{L}$ which we denote as average shot-noise power.

Density perturbations due to shot-noise excite fluctuations in the LSC fields which, in turn, can give rise to collective plasma oscillations. It is then important to compute the coupling of shot-noise to the plasma eigenmodes in order to study the evolution of shot-noise microbunching under the effect of LSC self-fields. Note that, by construction, our analysis only includes the coupling to the collective space-charge modes. As shown by Kim et al., when thermal motion due to the finite energy spread of the electrons is significant (namely a non-negligible value of K_γ), single-particle effects can suppress the plasma behavior of shot-noise. We will thus limit our shot-noise analysis to small values of the energy spread parameter.

In the case of coupling to shot-noise the IVP must be treated statistically. Namely, the coupling coefficients $\langle f_\pm^\dagger, f_{1,0}\rangle$ have to be modified to take into account density fluctuations due to the intrinsic discrete nature of the six-dimensional particle distribution. Expressing the initial particle distribution as a sum of δ-functions in six-dimensional phase space we get:

$$\langle \hat{f}_\pm^\dagger, f_{1,0}\rangle = \frac{1}{L}\sum_j e^{-ik_z z_j}\int_{-\infty}^{0} e^{-i\frac{\omega_\pm \tau}{c}+ik_z\dot{z}_j\tau} E_\pm\left(\vec{x}_{j-}(\tau)\right) d\tau \qquad (4.21)$$

where $(\vec{x}_j, \vec{\beta}_{\perp j}, z_j, \eta_j)$ is the position in phase-space of the j-th particle and $\vec{x}_{j-}(\tau) = \vec{x}_j \cos k_\beta \tau - \frac{\vec{\beta}_{\perp,j}}{k_\beta}\sin k_\beta\tau$. The sum is performed over the N particles in the region $0 < z < L$. For an uncorrelated initial distribution, in which the initial phase-space perturbation is only due to shot-noise, the statistical average of the coupling coefficient vanishes but its average absolute value squared is different than zero. We shall thus compute the average microbunching power as:

$$\begin{aligned}\overline{|\tilde{n}|^2} =& e^{2\Im\{\Omega_+\}T}|c_+|^2\overline{|\langle\hat{f}_+^\dagger, f_{1,0}\rangle|^2} + e^{2\Im\{\Omega_-\}T}|c_-|^2\overline{|\langle\hat{f}_-^\dagger, f_{1,0}\rangle|^2} \\ &+ 2\Re\Big\{e^{-i(\Omega_+-\Omega_-^*)T}c_+c_-^*\overline{\langle f_+^\dagger, f_{1,0}\rangle\langle f_-^\dagger, f_{1,0}\rangle^*}\Big\}\end{aligned} \tag{4.22}$$

with:

$$c_\pm = -\frac{\omega_p}{c}\frac{\int_{-\infty}^0 dT'T'\frac{e^{-i\Omega_\pm T'-\frac{(K_\gamma T')^2}{2}}}{(1+iK_\epsilon T')^2+4w_\pm(1+iK_\epsilon T')}}{\int_{-\infty}^0 dT'\frac{T'^2e^{-i\Omega_\pm T'-\frac{(K_\gamma T')^2}{2}}}{(1+iK_\epsilon T')^2+4w_\pm(1+iK_\epsilon T')+4w_\pm^2\sin^2 K_\beta T'}} \tag{4.23}$$

It can be shown that the statistically averaged coupling coefficients are given by (see the derivation in the appendix):

$$\begin{aligned}\overline{|\langle\hat{f}_\pm^\dagger, f_{1,0}\rangle|^2} =& \frac{n_\lambda^2c^2}{N\omega_p^2}\int_{-\infty}^0 dT'\frac{e^{-i\Omega_\pm T'}-e^{-i\Omega_\pm^*T'}}{-i(\Omega_\pm-\Omega_\pm^*)} \\ &\frac{e^{-\frac{K_\gamma^2T'^2}{2}}}{(1+iK_\epsilon T')^2+4\Re\{w_\pm\}(1+iK_\epsilon T')+4|w_\pm|^2\sin^2 K_\beta T'},\end{aligned} \tag{4.24}$$

while the cross-term $\overline{\langle f_+^\dagger, f_{1,0}\rangle\langle f_-^\dagger, f_{1,0}\rangle^*}$ can be computed as:

$$\begin{aligned}\overline{\langle\hat{f}_+^\dagger, f_{1,0}\rangle\langle\hat{f}_-^\dagger, f_{1,0}\rangle^*} =& \frac{n_\lambda^2c^2}{N\omega_p^2}\int_{-\infty}^0 dT'\frac{e^{-i\Omega_+T'}-e^{-i\Omega_-^*T'}}{-i(\Omega_+-\Omega_-^*)} \\ &\frac{e^{-\frac{K_\gamma^2T'^2}{2}}}{(1+iK_\epsilon T')^2+2(w_++w_-^*)(1+iK_\epsilon T')+4w_+w_-^*\sin^2 K_\beta T'}.\end{aligned} \tag{4.25}$$

We recall that in the cold beam limit ($K_\gamma \ll 1, K_\epsilon \ll 1$) we have $\Omega_\pm = \pm\Omega$, $w_\pm = w$, $\Im\{\Omega\} = 0$ and $\Im\{w\} = 0$. In this limit Eq.(4.22) reduces to:

$$\overline{|\tilde{n}|^2} = \overline{|\tilde{n}_{sn}|^2}\Gamma_{sn}^2\cos^2\Omega T \tag{4.26}$$

where the shot noise geometrical coupling coefficient is $\Gamma_{sn}^2 = \frac{1+4w}{(1+2w)^2}$ for $K_\beta \ll 1$ and $\Gamma_{sn}^2 = \frac{1+4w+2w^2}{(1+2w)^2}$ for $K_\beta \gg 1$. Note that $\Gamma_{sn} < 1$, which means that the density modulation associated with the fundamental mode at $T = 0$ is smaller than the shot-noise density perturbation $|\tilde{n}_{sn}|^2$. This inconsistency arises because shot-noise couples to a great number of plasma eigenmodes while here we are only considering the fundamental one. As mentioned before, in many practical cases we are mostly concerned with the dominant mode since it is the one with the strongest response from the beam. For example, for shot-noise suppression experiments, we are interested in studying the evolution of the fundamental mode since it is the mode that mostly contributes to the noise contamination of seeded free-electron lasers.

Figure 4.2 shows the shot-noise geometrical coupling coefficient Γ_{sn} as a function of D. Note that, for $D \ll 1$ the coupling coefficient tends to one, which indicates that in this limit excitation of higher order radial modes from shot-noise is strongly suppressed. In the opposite limit ($D \gg 1$), for $K_\beta \gg 1$ the fundamental mode is strongly coupled to shot-noise whereas, for $K_\beta \ll 1$, the coupling coefficient decreases monotonically as $\frac{1}{\sqrt{2D}}$. The latter condition ($D \gg 1$, $K_\beta \ll 1$) is identified as the one-dimensional limit, in which the plasma eigenmodes are fully degenerate [42]. In this limit, our three-dimensional modal description should take into account a great number of radial modes and a one-dimensional or quasi-three dimensional theory (as the one found in [30]) would be more suited for the description of the IVP.

Note that the different behavior of Γ_{sn} for large values of D in the two opposite limits of laminar motion ($K_\beta \ll 1$) and high betatron frequency ($K_\beta \gg 1$) is a direct consequence of the degeneracy breaking induced by transverse focusing, which was discussed in [42].

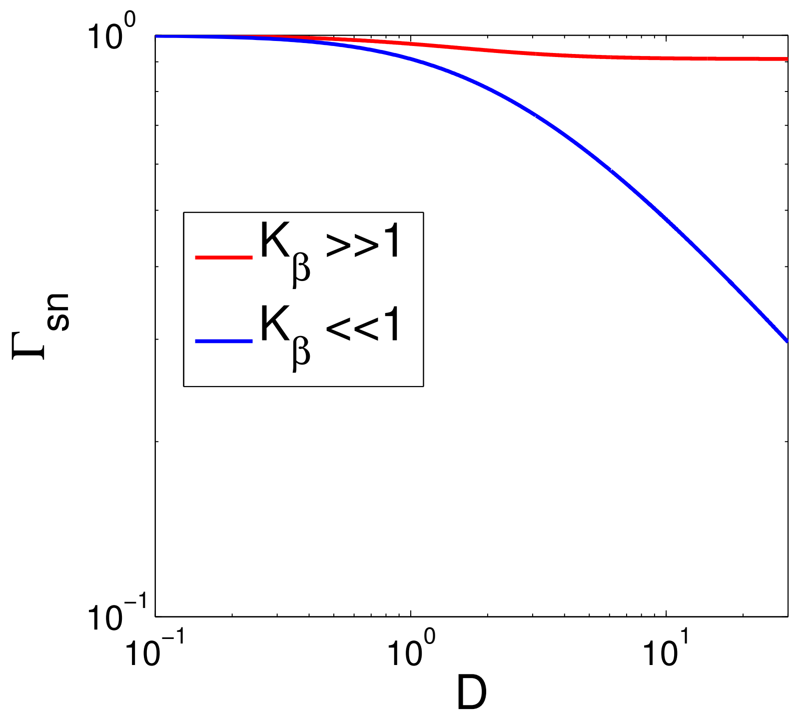

Figure 4.2: Shot noise geometrical coupling coefficient as a function of the 3-D parameter for the laminar beam limit (blue curve) and the high betatron frequency limit (red curve)

4.4 Numerical Examples

In this section we describe some specific application of the theory described in this chapter. We will refer to the following beam parameters, roughly corresponding to the compressed mode of operation of the Next Linear Collider Test Accelerator (NLCTA):

- beam energy: $E_b = 120MeV$;
- beam current: $I_b = 350A$;
- normalized transverse emittance: $\epsilon = 3mm \times mrad$;
- slice energy spread: $\sigma_\eta = 5 \times 10^{-5}$.

We will study the evolution of an initial coherent density perturbation under the effect of longitudinal space-charge forces to show how three-dimensional and thermal effects affect the plasma dynamic of the beam.

Note that for a non-accelerating beam the transverse emittance is a conserved quantity. The transverse beam size is related to the normalized emittance as: $\sigma_x = \sqrt{\frac{\beta_f \epsilon}{\gamma}}$ where the β function is defined as $\beta_f = 1/k_\beta$. In space-charge based experiments (such as microbunching reduction or amplification) it is generally desirable to increase the intensity of the longitudinal space-charge forces by increasing the density of the beam (namely by matching the beam to a small value of β_f). However, for a given transverse emittance, we have: $K_\epsilon \propto 1/\sigma_x \propto 1/\beta_f^{1/2}$ which means that increasing the collective response by strongly focusing the beam comes at the expense of increasing the longitudinal velocity spread due to emittance, which leads to damping of the microbunching structure. Figure 4.3 shows the time evolution of the fundamental mode excited by an initial coherent density perturbation at a wavelength of $\lambda = 2\pi/k_z = 800nm$. The initial density

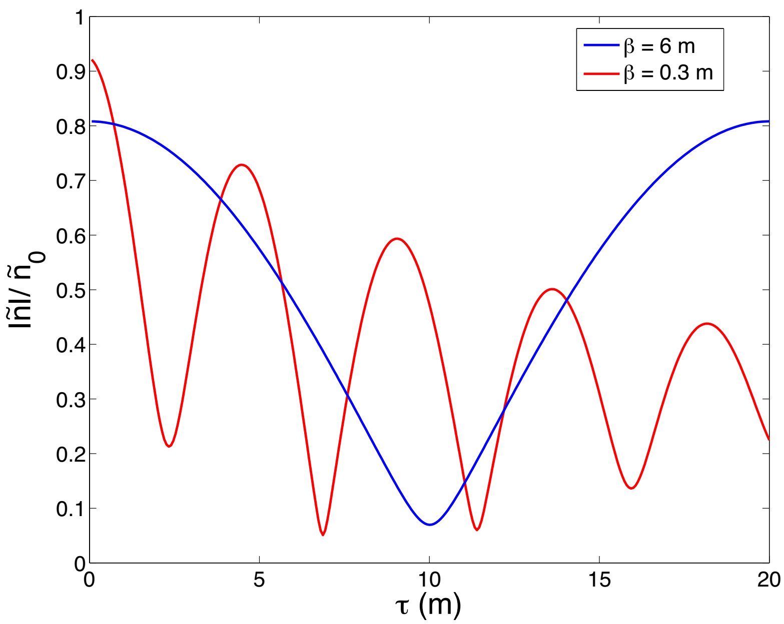

Figure 4.3: Time evolution of a coherent density modulation for the NLCTA beam parameters and $\beta_f = 6m$ (blue line) and $\beta_f = 0.3m$ (red line)

perturbation is given by: $f_{1,0} = b_0 f_0$, with $b_0 \ll 1$ (corresponding to $\nu = 0$ with reference to section 4.2) for several values of the beta function. As expected the microbunching plasma dynamic is faster for stronger focusing. For small values of the beta function, emittance induced Landau damping becomes important, exponentially suppressing the backward propagating mode.

Note that the bunching factor in Fig.4.3 does not go to zero after a quarter of plasma period since the backward and forward modes have different frequencies and different coupling coefficients. This effect is particularly noticeable for smaller values of β_f (which correspond to higher values of the emittance parameter K_ϵ). This can be an important limitation in noise reduction schemes, where the shot-noise microbunching of an electron beam is suppressed by letting the beam perform a quarter plasma oscillation [14]

To better understand this effect we study the effect of emittance on the amplitude of the shot-noise bunching factor after one quarter plasma period. Fig.4.4 shows the amplitude of the first minimum of the shot-noise microbunching $\sqrt{\overline{|\tilde{n}|^2}}$ as a function of β_f for several values of the beam emittance. Ideally, for a cold beam, the shot-noise bunching factor is suppressed after one quarter plasma oscillation. However when emittance is included, the first minimum of the shot-noise amplitude is different than zero and its amplitude increases with decreasing β_f (i.e. increasing K_ϵ). This limits the amount of suppression achievable in a noise-suppression experiment. A similar effect can be caused by energy spread, as discussed by Kim.

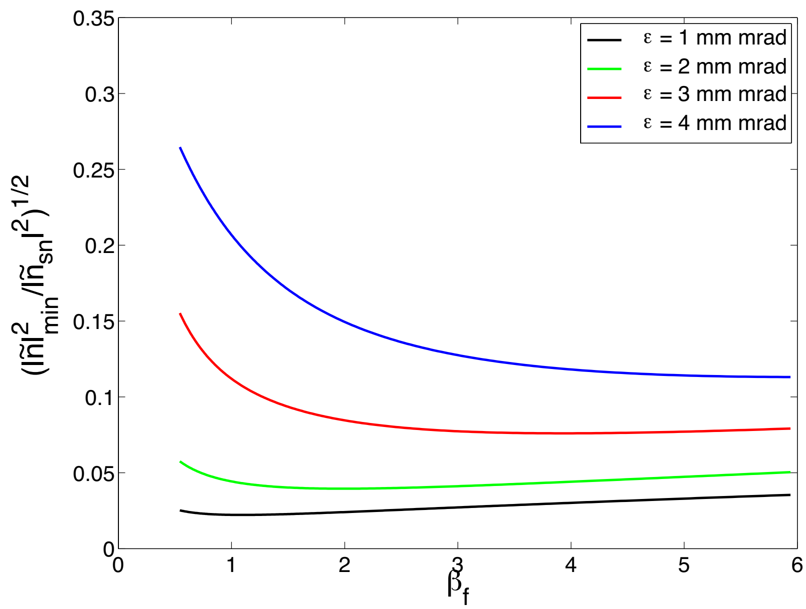

Figure 4.4: Amplitude of the first minimum of the RMS shot-noise microbunching normalized to the starting shot-noise level $\overline{|\tilde{n}_{sn}|^2}$ as a function of the β_f function for several values of the normalized transverse emittance.

4.5 Conclusions

In this chapter we have analyzed the initial value problem of longitudinal plasma oscillations for a thermal relativistic electron beam. Our analysis is based on an eigenmode expansion of the initial perturbation in six-dimensional phase-space and includes the effects of energy-spread, finite emittance, betatron motion and edge effects due to the finite size of the beam. The eigenmode expansion relies on the solutions of the plasma oscillation eigenvalue problem discussed in [42] and takes advantage of the bi-othogonality property of the phase-space plasma eigenmodes and their set of adjoint eigenmodes.

We have derived a general formalism for the IVP which describes the evolution of an arbitrary initial perturbation under the effect of longitudinal space-charge forces for a beam matched to a focusing channel. Later on we have derived closed form expressions for the evolution of the fundamental plasma eigen-mode starting from a coherent density perturbation as well as from density fluctuations due to shot-noise. Explicit solutions for the coupling coefficient of the initial perturbation to the fundamental mode have been derived in the cold beam limit and used to describe how three-dimensional effects and betatron motion affect the physics of this problem .

Finally, the mathematical formalism of the IVP, and its implementation for the fundamental mode have been used to describe the time evolution of beam microbunching for a specific example corresponding the the NLCTA beam parameters.

4.A Derivation of the normalization coefficients for a coherent density modulation

In this section we derive some of the expressions reported in section 4.2. Following the definitions given in Section 4.1, the normalization coefficient for a transversely Gaussian field can be expressed as:

$$\begin{aligned}\langle f_{\pm}^{\dagger}, f_{\pm}\rangle =&\frac{ikn_{\lambda}c^3}{\gamma^2\omega_p^3}\int_{-\infty}^{0} dT\int_{-\infty}^{0} dT'\int d^2\vec{B}d^2\vec{X}F_{0,\perp}E_z\big(X_+(T)\big)E_z\big(X_-(T')\big)\\ &(T+T')e^{-i\Omega_{\pm}(T+T')-\frac{(K_{\gamma}(T+T'))^2}{2}-\frac{(\vec{X}^2+\vec{B}^2)iK_{\epsilon}(T+T')}{2}}\end{aligned} \tag{4.27}$$

where $\Omega_{\pm}$ and $f_{\pm}$ are, respectively, the two dominant roots (with positive/negative real part) of the dispersion relation and the two associated eigenfunctions in the variational approximation, $n_{\lambda} = n_0 2\pi\sigma_x^2$ is the average linear beam density and we have omitted the inessential factor $-e/\gamma mc^2$ from both $f_{\pm}$ and $f_{\pm}^{\dagger}$.

The $d^2\vec{X}d^2\vec{B}$ integral yields:

$$\begin{aligned}\langle f_{\pm}^{\dagger}, f_{\pm}\rangle = -\frac{ikn_{\lambda}c^3}{\gamma^2\omega_p^3}\int_{-\infty}^{0} dT\int_{-\infty}^{0} dT'(T+T')e^{-i\Omega_{\pm}(T+T')-\frac{(K_{\gamma}(T+T'))^2}{2}}\\ \frac{1}{(1+iK_{\epsilon}(T+T'))^2+4w_{\pm}(1+iK_{\epsilon}(T+T'))+4w_{\pm}^2\sin^2 K_{\beta}(T+T')}\end{aligned} \tag{4.28}$$

By performing the change of variables $T+T' = T''$ and integrating by parts in dT we finally obtain

$$\langle f_{\pm}^{\dagger}, f_{\pm}\rangle = \frac{ikn_{\lambda}c^3}{\gamma^2\omega_p^3}\int_{-\infty}^{0} dT\frac{T^2e^{-i\Omega_{\pm}T-\frac{(K_{\gamma}T)^2}{2}}}{(1+iK_{\epsilon}T)^2+4w_{\pm}(1+iK_{\epsilon}T)+4w_{\pm}^2\sin^2 K_{\beta}T} \tag{4.29}$$

4.B Derivation of the statistically averaged coupling coefficients of shot-noise to the fundamental plasma eigen-mode

By taking the absolute value squared of Eq.(4.21), recalling that $\overline{e^{ik_z(z_j-z_l)}} = \delta_{j,l}$, we have:

$$\overline{|\langle f_\pm^\dagger, f_{1,0}\rangle|^2} = \int d^2\vec{\beta}_\perp d^2\vec{x} \int_{-\infty}^{0} d\tau \int_{-\infty}^{0} d\tau' f_0 E_\pm\left(\vec{x}_+(\tau)\right) E_z^*\left(\vec{x}_-(\tau)\right) e^{i(\frac{\omega_\pm}{c}+k_z\dot{z})\tau - i(\frac{\omega_\pm^*}{c}+k_z\dot{z})\tau'}. \tag{4.30}$$

Performing the integral in $d^2\vec{\beta}_\perp d^2\vec{x}$ we have, in dimensionless units:

$$\begin{aligned}\overline{|\langle f_\pm^\dagger, f_{1,0}\rangle|^2} =& \frac{n_\lambda^2 c^2}{N\omega_p^2} \int_{-\infty}^{0} dT \int_{-\infty}^{0} dT' e^{-i(\Omega_\pm T - \Omega_\pm^* T') - \frac{K_\gamma^2 (T-T')^2}{2}} \\ & \frac{1}{(1+iK_\epsilon(T-T'))^2 + 4\Re\{w_\pm\}(1+iK_\epsilon(T-T')) + 4|w_\pm|^2 \sin^2 K_\beta(T-T')}.\end{aligned} \tag{4.31}$$

Finally, performing the change of variables $T - T' = T''$ and integrating by parts we obtain the final result shown in section 4.3:

$$\begin{aligned}\overline{|\langle f_\pm^\dagger, f_{1,0}\rangle|^2} =& \frac{n_\lambda^2 c^2}{N\omega_p^2} \int_{-\infty}^{0} dT' \frac{e^{-i\Omega_\pm T'} - e^{-i\Omega_\pm^* T'}}{-i(\Omega_\pm - \Omega_\pm^*)} \\ & \frac{e^{-\frac{K_\gamma^2 T'^2}{2}}}{(1+iK_\epsilon T')^2 + 4\Re\{w_\pm\}(1+iK_\epsilon T') + 4|w_\pm|^2 \sin^2 K_\beta T'}.\end{aligned} \tag{4.32}$$

Similarly we can compute the cross-term in Eq.(4.22) as:

$$\begin{aligned}\overline{\langle f_+^\dagger, f_{1,0}\rangle\langle f_-^\dagger, f_{1,0}\rangle^*} = & \frac{n_\lambda^2 c^2}{N\omega_p^2} \int_{-\infty}^{0} dT \int_{-\infty}^{0} dT' e^{-i(\Omega_+ T - \Omega_-^* T') - \frac{K_\gamma^2 (T-T')^2}{2}} \\ & \frac{1}{(1+iK_\epsilon(T-T'))^2 + 2(w_+ + w_-^*)(1+iK_\epsilon(T-T')) + 4w_+ w_-^* \sin^2 K_\beta(T-T')}\end{aligned} \tag{4.33}$$

which reduces to:

$$\overline{\langle f_+^\dagger, f_{1,0}\rangle\langle f_-^\dagger, f_{1,0}\rangle^*} = \frac{n_\lambda^2 c^2}{N\omega_p^2}\int_{-\infty}^{0} dT' \frac{e^{-i\Omega_+ T'} - e^{-i\Omega_-^* T'}}{-i(\Omega_+ - \Omega_-^*)} \frac{e^{-\frac{K_\gamma^2 T'^2}{2}}}{(1+iK_\epsilon T')^2 + 2(w_+ + w_-^*)(1+iK_\epsilon T') + 4w_+ w_-^* \sin^2 K_\beta T'}. \tag{4.34}$$

CHAPTER 5

Three Dimensional Kinetic Theory of the Longitudinal Space-Charge Amplifier

In the previous chapters, the self-consistent evolution of small perturbations in six-dimensional phase-space was analyzed in the context of an initial value problem based on a bi-orthogonal eigenmode expansion in six-dimensional phase-space. This analysis allows to study the effects of transverse betatron motion and longitudinal velocity spread on the beam space-charge waves and it's the basis for a self-consistent kinetic analysis of space-charge induced microbunching amplification.

Space-charge based microbunching amplification is a two-step process (see Fig. 5.1): an electron beam with a small density modulation travels through a drift space or a focusing channel and the longitudinal space-charge field generates an energy modulation. After the drift, a magnetic chicane or any transport element with a significant longitudinal dispersion, shifts the longitudinal position of the particles proportionally to their energy, thus transforming the accumulated energy modulation into a density modulation. For a high quality beam (low energy spread and emittance) the final amplitude of the density modulation can be much higher than the initial value, resulting in a significant amplification of the bunching factor.

This effect is usually referred to as microbunching instability and it can strongly affect the operation of high gain free-electron laser compromising the beam quality and interfering with beam diagnostic instruments. Recently, the longitudinal space-charge microbunching instability has been proposed as a broad-band amplifier for advanced free-electron laser seeding schemes [13].

In this chapter we use the results from chapters 3 and 4 to give a self-consistent theoretical description of this process, with the inclusion of the kinetic effects described in the previous chapters (betatron motion, energy-spread and finite emittance). This chapter is organized as follows: in section 5.1 we describe the use of the formalism for the 6-dimensional initial value problem to describe the microbunching amplification induced by space-charge; in 5.2 we find explicit expressions for the microbunching gain associated with the fundamental plasma eigenmode starting from a coherent density modulation; in 5.3 we use the present formalism to analyze the amplification of shot-noise microbunching coupled to the fundamental mode; finally we show the application of this analysis to the optimization of a microbunching amplification experiment at the NLCTA test facility.

5.1 Six-dimensional model of space-charge microbunching

In this section we derive a general formulation for the microbunching induced by LSC starting from an arbitrary perturbation in six-dimensional phase-space. Throughout this chapter we will refer to the physical scenario described in fig.5.1. An electron beam with an initial perturbation in phase-space travels through a focusing channel, where the LSC field induces an energy modulation in the beam. After the focusing channel, a magnetic chicane introduces longitudinal dispersion, transforming the energy modulation into density modulation.

The self-consistent evolution of six-dimensional phase space under the effect of LSC can be described using the formalism developed in chapters 3, 4. We assume a coasting, non-accelerating electron beam of energy γmc^2 matched to a uniform focusing channel. The electron beam is described by a six-dimensional phase-space distribution function $f(\vec{x}, \vec{\beta}, z, \eta, \tau)$ where $\vec{x}$ is the transverse position with respect to the propagation axis, $\vec{\beta}$ is the transverse velocity normalized to the speed of light, $\eta = \frac{\delta\gamma}{\gamma}$ is the relative energy deviation, z is the longitudinal position along the beam and $\tau = ct$, where t is the time variable and c is the speed of light. The distribution function is expanded to first order in perturbation theory $f = f_0 + f_1 e^{ik_z z}$ where f_0 is a stationary distribution function and $|f_1| \ll f_0$. We assume a gaussian stationary distribution function of the type:$f_0 = n_0 e^{-\frac{\vec{x}^2}{2\sigma_x^2} - \frac{\vec{\beta}_\perp^2}{2\sigma_x^2 k_\beta^2} - \frac{\eta^2}{2\sigma_\eta^2}} / (2\pi)^{3/2} \sigma_x^2 k_\beta^2 \sigma_\eta$.

The perturbed phase-space distribution f_1 evolves under the effect of LSC forces starting from an initial value $f_{1,0}$. The evolution of the phase-space perturbation can be expressed in terms of the plasma eigen-modes of the beam. We define the LSC field eigenmodes E_n and eigenvalues ω_n as the solutions to the following eigenvalue equation:

$$(\nabla_\perp^2 - \frac{k_z^2}{\gamma^2}) E_n = -\frac{k_z^2 \omega_p^2}{\gamma^2 c^2} \int \int_{-\infty}^{0} \tau e^{-\frac{(k_z \sigma_\eta \tau)^2}{2} - i k_z \frac{k_\beta^2 \vec{x}^2 + \vec{\beta}_\perp^2}{4} \tau - i \frac{\omega_n \tau}{c}} E_n(\vec{x}_+(\tau)) f_{0\perp} d\tau d^2 \vec{\beta}_\perp. \tag{5.1}$$

where $f_{0\perp} = e^{-\frac{\vec{x}^2}{2\sigma_x^2} - \frac{\vec{\beta}_\perp^2}{2\sigma_x^2 k_\beta^2}} / 2\pi \sigma_x^2 k_\beta^2$, $\vec{x}_\pm(\tau) = \vec{x} \cos k_\beta \tau \pm \frac{\vec{\beta}}{k_\beta} \sin k_\beta \tau$ and $\omega_p^2 = \frac{n_0 e^2}{\epsilon_0 \gamma^3 m}$ is the one-dimensional plasma oscillation frequency. The field eigenmodes represent a set of propagating solutions to the system of coupled Poisson/Vlasov equation.

The phase-space eigenmodes of the beam associated with the field eigenmodes are

$$\hat{f}_n = -\frac{e}{\gamma mc^2} \partial_\eta f_0 \int_{-\infty}^{0} e^{-i \frac{\omega_n \tau}{c} + i k_z \dot{z} \tau} E_n \left(\vec{x}_+(\tau) \right) d\tau, \tag{5.2}$$

with $\dot{z} = \eta/\gamma^2 - (k_\beta^2 \vec{x}^2 + \vec{\beta}^2)/4$ and $\vec{x}_\pm(\tau) = \vec{x} \cos k_\beta \tau \pm \frac{\vec{\beta}}{k_\beta} \sin k_\beta \tau$. The adjoint phase-space eigenmodes are

$$\hat{f}_n^\dagger = -\frac{e}{\gamma mc^2} \int_{-\infty}^{0} e^{-i\frac{\omega_n \tau}{c} + ik_z \dot{z}\tau} E_n^\dagger \left(\vec{x}_-(\tau)\right) d\tau, \tag{5.3}$$

where, for a general field eigenmode of the type $E_n(\vec{x}) = R_{m,r}(|\vec{x}|)e^{im\phi}$ (where ϕ is the polar angle in the transverse plane) the adjoint field eigenmode is given by the following relation $E_n = R_{m,r}(|\vec{x}|)e^{im\phi} \leftrightarrow E_n^\dagger = R_{m,r}(|\vec{x}|)e^{-im\phi}$.

The phase-space eigenmodes represent a set of propagating solutions to the system of coupled Maxwell/Vlasov equations described in [42] and in chapter 3. These solutions can be employed as a representation basis for the perturbed phase-space distribution starting from the initial perturbation $f_{1,0}$. The evolution of the phase-space perturbation in the focusing channel is then computed by using the bi-orthogonality property of the phase-space eigenmodes with respect to the set of adjoint eigenmodes:

$$f_1(\tau) = \sum_n \hat{f}_n e^{-i\frac{\omega_n \tau}{c}} \frac{\langle \hat{f}_n^\dagger, f_{1,0} \rangle}{\langle \hat{f}_n^\dagger, \hat{f}_n \rangle}. \tag{5.4}$$

where $< a, b >= \int d\eta d^2\vec{\beta} d^2\vec{x} a(\vec{x}, \vec{\beta}, \eta, \tau) b(\vec{x}, \vec{\beta}, \eta, \tau)$ is the five-dimensional scalar product.

Equation (5.4) solves our problem up to the entrance of the magnetic chicane. To complete the analysis we have to describe the effect of longitudinal dispersion in the magnetic chicane. The magnetic chicane introduces the following coordinate transformation $z \to z + R_{56}\eta$. The effect of this transformation on the phase-space perturbation is that of introducing a phase-shift proportional to the energy deviation as: $f_1 \to f_1 e^{-ik\eta R_{56}}$. It follows that the density modulation after

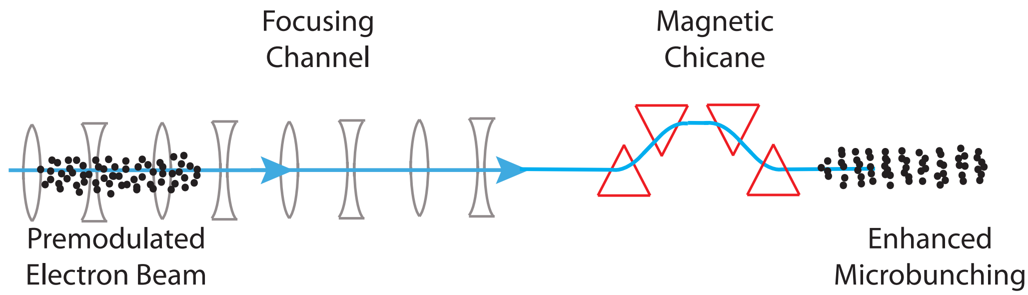

Figure 5.1: Schematic representation of a longitudinal space-charge amplifier.

a focusing channel of length L_d and magnetic chicane dispersion R_{56} is given by:

$$\tilde{n}_{R_{56}} = \sum_n \frac{\langle \hat{f}_n^\dagger, f_{1,0} \rangle}{\langle \hat{f}_n^\dagger, \hat{f}_n \rangle} \int d\eta d^2\vec{\beta} d^2\vec{x} \hat{f}_n e^{-ik\eta R_{56} - i\frac{\omega_n L_d}{c}}. \tag{5.5}$$

Equation (5.5) describes the density modulation induced by LSC starting from an arbitrary perturbation $f_{1,0}$. In the following sections we will find explicit closed-form expressions for some of the cases of interest to illustrate the physical processes involved in the LSC gain mechanism.

In what follows, we will use the dimensionless scaling parameters and variables introduced in chapter 3.

5.2 Microbunching gain for the fundamental plasma eigenmode

In this section we will compute the microbunching gain in Eq.(5.5) for the fundamental plasma eigenmode. For the sake of simplicity we will use the variational solutions to the plasma eigenmode problem that were derived in [42]. In the variational approximation, the electric field is approximated with a gaussian mode $E_z = e^{-w|\vec{X}|^2}$. The plasma eigenvalue Ω and the variational parameter w are computed by projecting the field dispersion equation (3.8) on the gaussian mode and imposing the condition $\frac{d\Omega}{dw} = 0$. We will also work in the dominant pole approximation, and we will keep the two roots of the dispersion relation with the lowest Landau damping constant. The two roots are identified as $\Omega_\pm$ and are associated with the phase space eigenmodes $\hat{f}_\pm$ and the field eigenmodes with variational paramters $w_\pm$. The notation $\pm$ refers to the sign of the real part of the eigenvalue, corresponding to a forward or backward propagating space-charge wave depending on the sign of k_z. Note that the propagation properties of the forward and backward modes are different due to the anisotropy induced by transverse emittance. In particular the backward propagating mode has a stronger emittance induced damping. With the above notation and assumptions the density modulation amplitude after longitudinal dispersion is given by:

$$\begin{aligned}\tilde{n} \simeq ik_z R_{56} n_\lambda e^{-\frac{K_\phi^2}{2}} \Bigg(& e^{-i\Omega_+ T} \frac{\langle \hat{f}_+^\dagger, f_{1,0}\rangle}{\langle \hat{f}_+^\dagger, \hat{f}_+\rangle} \int_{-\infty}^{0} dT' \frac{e^{-i(\Omega_+ + iK_\gamma K_\phi)T' - \frac{(K_\gamma T')^2}{2}}}{(1+iK_\epsilon T')^2 + 2w_+(1+iK_\epsilon T')} \\ & + e^{-i\Omega_- T} \frac{\langle \hat{f}_-^\dagger, f_{1,0}\rangle}{\langle \hat{f}_-^\dagger, \hat{f}_-\rangle} \int_{-\infty}^{0} dT' \frac{e^{-i(\Omega_- + iK_\gamma K_\phi)T' - \frac{(K_\gamma T')^2}{2}}}{(1+iK_\epsilon T')^2 + 2w_-(1+iK_\epsilon T')} \Bigg)\end{aligned} \tag{5.6}$$

with $K_\phi = k\sigma_\eta R_{56}$. Note that in Eq. (5.6) we have only kept the term proportional to R_{56}, which accounts for the microbunching enhancement due to longitudinal rearrangement.

In chapter 4, explicit expressions for the coupling and normalization coefficients were found for the fundamental mode in the variational approximation. In dimensionless units we have:

$$\langle \hat{f}_\pm^\dagger, \hat{f}_\pm\rangle = \frac{ikn_\lambda c^3}{\gamma^2\omega_p^3} \int_{-\infty}^{0} dT \frac{T^2 e^{-i\Omega_\pm T - \frac{(K_\gamma T)^2}{2}}}{(1+iK_\epsilon T)^2 + 4w_\pm(1+iK_\epsilon T) + 4w_\pm^2 \sin^2 K_\beta T} \tag{5.7}$$

where $n_\lambda = n_0 2\pi\sigma_x^2$ is the average linear beam density and we have omitted the inessential factor $-e/\gamma mc^2$ from both $\hat{f}_\pm$ and $\hat{f}^\dagger_\pm$.

To find a closed form expression for the coupling coefficient $\langle \hat{f}^\dagger_\pm, f_{1,0}\rangle$, one has to make some assumptions on the initial phase space perturbation. In this section we will discuss the case of a coherent density modulation with the following type of perturbation: $f_{1,0} = \tilde{\rho}(\vec{x}) f_0(\vec{x}, \vec{\beta}, \eta)$. We will also assume that the input bunching factor has a gaussian shape: $\tilde{\rho} = \frac{\tilde{n}_0}{n_\lambda}(1 + 2\nu)e^{-\nu \vec{X}^2}$. The resulting coupling coefficient is for this type of initial perturbation was computed in chapter 4:

$$\langle \hat{f}^\dagger_\pm, f_{1,0}\rangle = \tilde{n}_0(1+2\nu)\frac{c}{\omega_p}\int_{-\infty}^{0} dT \frac{e^{-i\Omega_\pm T - \frac{(K_\gamma T)^2}{2}}}{(1 + iK_\epsilon T)^2 + 2(w_\pm + \nu)(1 + iK_\epsilon T) + 4w_\pm \nu \sin^2 K_\beta T}. \tag{5.8}$$

In the cold beam limit ($K_\gamma \ll 1$, $K_\epsilon \ll 1$) Eqs.(5.6,4.15,4.16) reduce to:

$$\tilde{n} = -\tilde{n}_0 \frac{\omega_p}{c}\gamma^2 R_{56} e^{-\frac{K_\phi^2}{2}} \Gamma \Omega_+ \sin \Omega_+ T, \tag{5.9}$$

where the geometrical coupling coefficient is given by: $\Gamma = \frac{(1+2\nu)(1+4w)}{(1+2w)(1+2(w+\nu))}$ for $K_\beta \ll 1$ and $\Gamma = \frac{(1+2\nu)(1+4w+2w^2)}{(1+2(w+\nu)+2w\nu)(1+2w)}$ for $K_\beta \gg 1$. Note that, up to a factor Γ, this formula is equivalent to the one derived in [30], revealing the same underlying physical process. The gain mechanism induced by the longitudinal space-charge corresponds to a fraction of plasma oscillation of duration t_{sc} followed by a space-charge-free drift of length $L_{eq} = \gamma^2 R_{56}$. The resulting microbunching gain can be interprepeted as the time-derivative of the density modulation $d\tilde{n}/dt = -\Gamma\omega \sin \omega t_{sc}$ times the crossing time of the space-charge free drift. Finally, the phase mixing effect due to the finite energy spread introduces the term $e^{-K_\phi^2/2}$. Note that even for $K_\gamma \ll 1$ energy spread can have a significant effect due to the phase mixing term. In other words, energy spread can have a negligible effect on the plasma oscillation but it can become important in the longitudinal rearrangement process.

5.3 Shot-noise amplification

In the case of coupling to shot-noise the problem of microbunching gain must be treated statistically. Namely, the coupling coefficients $\langle f_\pm^\dagger, f_{1,0}\rangle$ have to be modified to take into account density fluctuations due to the intrinsic discrete nature of the six-dimensional particle distribution. Expressing the initial particle distribution as a sum of δ-functions in six-dimensional phase space we get 4:

$$\langle f_\pm^\dagger, f_{1,0}\rangle = \frac{1}{L}\sum_j e^{-ik_z z_j}\int_{-\infty}^{0} e^{-i\frac{\omega_\pm\tau}{c}+ik_z\dot{z}_j\tau}E_\pm\left(\vec{x}_{j-}(\tau)\right)d\tau \tag{5.10}$$

where $(\vec{x}_j, \vec{\beta}_j, z_j, \eta_j)$ is the position in phase-space of the j-th particle and $\vec{x}_{j-}(\tau) = \vec{x}_j\cos k_\beta\tau - \frac{\vec{\beta}_{\perp,j}}{k_\beta}\sin k_\beta\tau$. The sum is performed over the N particles in the region $0 < z < L$. For an uncorrelated initial distribution the average density modulation vanishes but the average absolute value squared is different than zero. We shall thus compute the averaged microbunching power as:

$$\overline{|\tilde{n}|^2} = e^{2\Omega_+^I T}|g_+|^2\overline{|\langle f_+^\dagger, f_{1,0}\rangle|^2}+e^{2\Omega_-^I T}|g_-|^2\overline{|\langle f_-^\dagger, f_{1,0}\rangle|^2}+2\Re\left\{e^{-i(\Omega_+-\Omega_-^*)T}g_+g_-^*\overline{\langle f_+^\dagger, f_{1,0}\rangle\langle f_-^\dagger, f_{1,0}\rangle^*}\right\} \tag{5.11}$$

with:

$$g_\pm = \frac{\omega_p^2\gamma^2 R_{56}}{c^2}e^{-\frac{K_\phi^2}{2}}\frac{\int_{-\infty}^{0}dT'\frac{e^{-i(\Omega_\pm+iK_\gamma K_\phi)T'-\frac{(K_\gamma T')^2}{2}}}{(1+iK_\epsilon T')^2+4w(1+iK_\epsilon T')}}{\int_{-\infty}^{0}dT'\frac{T'^2e^{-i\Omega_\pm T'-\frac{(K_\gamma T')^2}{2}}}{(1+iK_\epsilon T')^2+4w(1+iK_\epsilon T')+4w^2\sin^2 K_\beta T'}} \tag{5.12}$$

By taking the absolute value squared of Eq.(4.21), recalling that $\overline{e^{ik_z(z_j-z_l)}} =$

$\delta_{j,l}$, and using the results from chapter 4:

$$\overline{|\langle \hat{f}^\dagger_\pm, f_{1,0}\rangle|^2} = \frac{n_\lambda^2 c^2}{N\omega_p^2}\int_{-\infty}^{0} dT' \frac{e^{-i\Omega_\pm T'} - e^{-i\Omega^*_\pm T'}}{-i(\Omega_\pm - \Omega^*_\pm)} \frac{e^{-\frac{K_\gamma^2 T'^2}{2}}}{(1+iK_\epsilon T')^2 + 4\Re\{w_\pm\}(1+iK_\epsilon T') + 4|w_\pm|^2\sin^2 K_\beta T'}, \tag{5.13}$$

and

$$\overline{\langle \hat{f}^\dagger_+, f_{1,0}\rangle\langle \hat{f}^\dagger_-, f_{1,0}\rangle^*} = \frac{n_\lambda^2 c^2}{N\omega_p^2}\int_{-\infty}^{0} dT' \frac{e^{-i\Omega_+ T'} - e^{-i\Omega^*_- T'}}{-i(\Omega_+ - \Omega^*_-)} \frac{e^{-\frac{K_\gamma^2 T'^2}{2}}}{(1+iK_\epsilon T')^2 + 2(w_+ + w_-^*)(1+iK_\epsilon T') + 4w_+w_-^*\sin^2 K_\beta T'}. \tag{5.14}$$

In the cold beam limit ($K_\gamma \ll 1, K_\epsilon \ll 1$) we have $\Omega_- \to -\Omega_+$ and $\Im\{\Omega_\pm\} \to 0$. In this limit Eq.(5.11) reduces to:

$$\overline{|\tilde{n}|^2} = \overline{|\tilde{n}_{sn}|^2}\left(\Gamma_{sn}\frac{\omega_p}{c}\gamma^2 R_{56} e^{-\frac{K_\phi^2}{2}}\Omega_+ \sin\Omega_+ T\right)^2 \tag{5.15}$$

where the shot noise geometrical coupling coefficient was defined in chapter 4 as: $\Gamma_{sn}^2 = \frac{1+4w}{(1+2w)^2}$ for $K_\beta \ll 1$ and $\Gamma_{sn}^2 = \frac{1+4w+2w^2}{(1+2w)^2}$ for $K_\beta \gg 1$, while $\overline{|\tilde{n}_{sn}|^2} = \frac{n_\lambda}{L}$ is the average shot-noise power.

5.4 Cold beam spectrum

In this section we will show some applications of our self-consistent analysis. We will consider the example of the Next Linear Collider Test Accelerator (NLCTA) at SLAC. We will assume the following beam parameters:

- beam energy: $E_b = 120MeV$;

- beam current: $I_b = 200A$;
- normalized transverse emittance: $\epsilon = 3mm \times mrad$;
- slice energy spread: $\sigma_\eta = 5 \times 10^{-5}$.

In this sub-section we study the amplification spectrum for the NLCTA beam in the cold beam limit. In this limit, we neglect the longitudinal velocity spread induced by emittance and we use the closed-form expression in Eq. (5.9). Since the coupling coefficient Γ depends on the details of the initial distribution of the beam microbunching, and it is typically of order $\simeq 1$ for many cases of interest, we will neglect it.

Figure 5.2 shows the microbunching power gain $g = |\tilde{n}_{R_{56}}/\tilde{n}_0|^2$ for a transverse beam size of $\sigma_x = 50\mu m$ and a drift length of $L_d = 0.5$, $L_d = 1$ and $L_d = 1.5$ respectively. The longitudinal dispersion is chosen to optimize the gain at $\lambda = 800nm$ for the assumed energy spread of $\sigma_\eta = 5 \times 10^{-5}$, i.e. $R_{56} = 1/k\sigma_\eta$

The gain is maximum around $\lambda \simeq 1\mu m$ and it rolls off as $e^{-(kR_{56}\sigma_\eta)^2}$ at short wavelengths due to the phase-mixing induced by energy-spread. At long wavelengths the gain decays due to transverse edge effects, which make the plasma frequency tend to zero as $D \to 0$. Using the variational solution the mode oscillation frequency scales as $\omega \propto 1/\lambda$, giving a scaling for the gain of $g \propto 1/\lambda^4$ for an interaction length much shorter than a quarter plasma period and $g \propto 1/\lambda^2$ for an interaction length close to a quarter plasma period. Note that the accuracy of the variational solution based on a Gaussian mode decreases for very small values of D (below 0.01), where the decay to 0 is slower than $\propto D$ (see e.g. the thin beam limit in Ref. [48]). However the previous discussion remains valid since variational solution is accurate within 10% for $D > 0.01$.

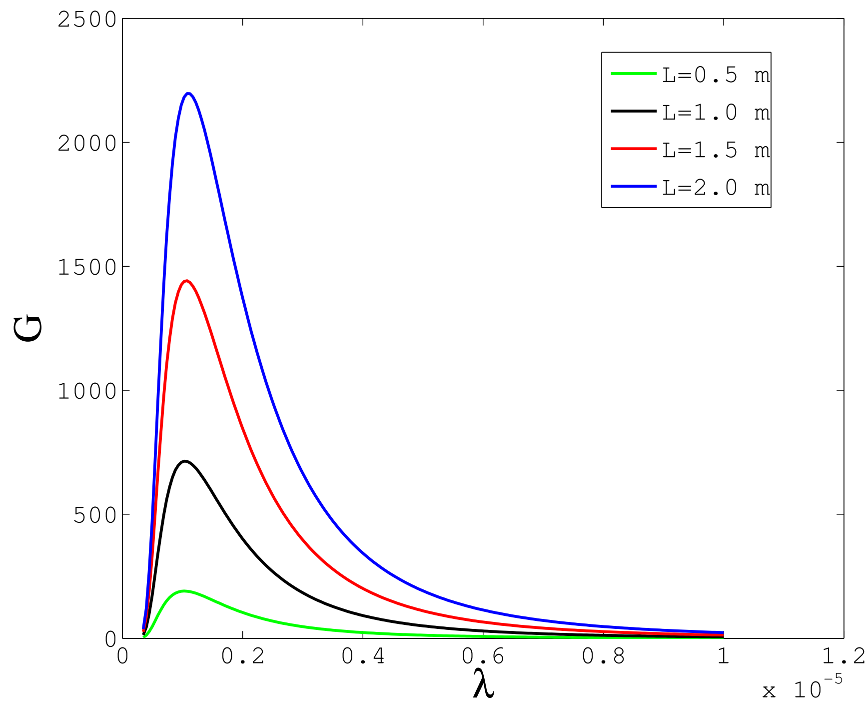

Figure 5.2: Amplification spectrum for the NLCTA beam paramters, with $\sigma_x = 50\mu m$ and several values of the drift length.

5.5 Optimization of a short-wavelength longitudinal space-charge amplifier

The longitudinal space-charge amplifier has been proposed as a source of broad-band radiation in the VUV / soft x-ray region. While the amplification of optical microbunching induced by space-charge happens spontaneously in x-ray FEL beamlines and has been observed at several facilites, the use of a longitudinal space-charge amplifier at short wavelenghts poses several challenges due to the effects of longitudinal thermal motion. These effects lead to Landau damping of the microbunching structure during the space-charge interaction [42], leading to suppression of the microbunching gain. At short wavelengths and high beam energies, the main contribution to thermal motion comes from emittance, since the longitudinal velocity-spread induced emittance scales like $\sigma_{\beta_z} \propto \epsilon_g^2 \propto 1/\gamma^2$, where ϵ_g is the beam's geometrical emittance (as opposed to the energy-spread term which scales as $\sigma_{\beta_z} \propto 1/\gamma^3$).

The optimization of a space-charge amplifier at short wavelengths, has to include the effects of emittance by balancing two competing effects. On one hand, by strongly focusing the beam the space-charge fields are enhanced and the gain tends to increase. On the other hand, strong focusing enhances the longitudinal velocity-spread due to transverse emittance, which tends to suppress the collective response of the electrons. The gain is then maximized when the two effects balance each other or, if the beam is cold enough, when the plasma oscillation mechanism makes the space-charge fields vanish after one-quarter plasma period.

Note that the same effect happens in x-ray high-gain free-electron lasers (see for example [10]), in which the beam focusing channel is designed to minimize the gain-length by balancing high-density and emittance-induced velocity spread.

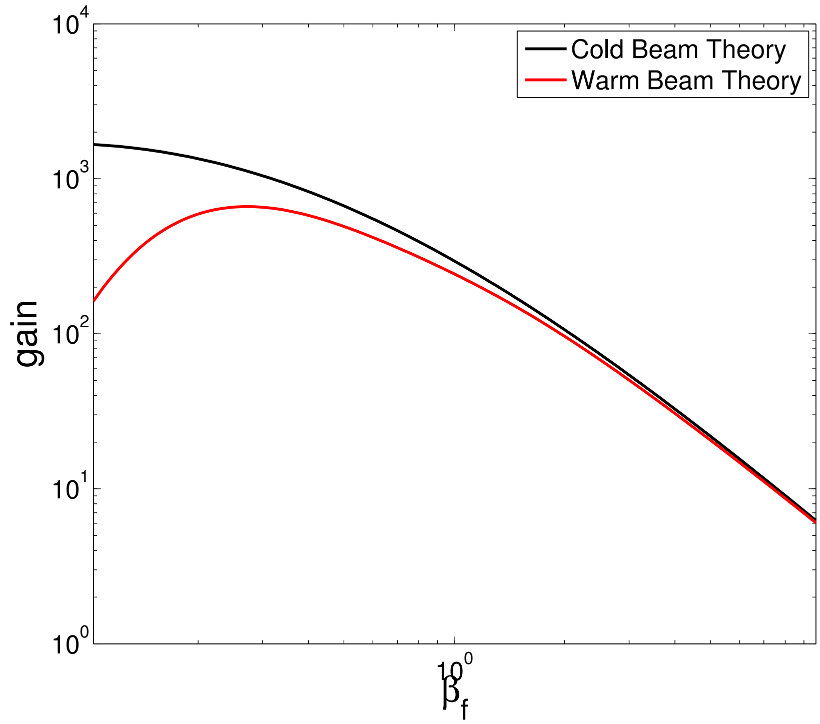

Figure 5.3: Microbunching power gain as a function of the beam β_f function for the $30nm$ longitudinal space-charge amplifier as derived from the cold beam (black line) and warm beam (red line) models.

To illustrate this point, we will discuss the example of a LSCA at $\lambda = 30nm$. We assume the following beam parameters:

- beam energy: $E_b = 1GeV$;
- beam current: $I_b = 1500A$;
- normalized transverse emittance: $\epsilon = 1mm \times mrad$;
- slice energy spread: $\sigma_\eta = 1 \times 10^{-4}$.

Figure 5.3 shows the microbunching power gain after $L_d = 5m$, as a function of the beam beta-function $\beta_f = 1/k_\beta$ for both the cold beam and the warm beam theory. The longitudinal dispersion is chosen to optimize the gain at $30nm$. In the cold beam model the gain increases with decreasing β_f until it reaches a maximum corresponding to the point in which the drift-length is equal to one-quarter plasma period. If we include the effects of emittance, however, the gain reaches a lower maximum value. For this value of the focusing function, we have $K_\epsilon \simeq 0.5$. For smaller values of the beta-function, the gain is suppressed due to the Landau damping induced by transverse emittance.

5.5.1 Higher order modes

In sections 3.4 and 3.5 we described the propagation features of higher-order plasma eigenmodes. It was found that, when the betatron frequency is larger than the beam plasma-frequency, the oscillation frequency of the higher-order plasma eigenmodes is significantly reduced with respect to the fundamental mode. This can have a significant impact on the transverse shape of the microbunched distribution.

In this section we will compare the gain mechanism for the fundamental mode and for the lowest order $m = 1$ transverse mode (the $E_{1,1,0}$ eigenmode) in the high-betatron frequency limit. We will not give the explicit details of the mathematical derivation but we will state some of the most important results.

The lowest order $m = 1$ eigenvalues are: $\Omega_{\pm,\pm} = \pm K_\beta \pm \delta\Omega$. It can be shown that the coupling and normalization coefficients have the same value for the the four associated phase-space eigenmodes $\hat{f}_{1,\pm,\pm}$. It follows that the microbunching gain for the lowest-order $m = 1$ mode is given by:

$$\tilde{n}_{R56/1,1,0} = -\tilde{n}_0 e^{-\frac{(k_z \sigma_\eta R_{56})^2}{2}} \Gamma_{1,1,0} \frac{\omega_p \delta\Omega}{c} \gamma^2 R_{56} \cos K_\beta T \sin \delta\Omega T, \tag{5.16}$$

where $\Gamma_{1,1,0}$ is a coupling coefficient of order ~ 1.

The term $\cos K_\beta T$ accounts for the ballistic evolution of the beam perturbation under the effect of transverse focusing, while the term $\sin \delta\Omega T$ describes the collective response of the electron beam. Note that, up to the geometrical coupling coefficients Γ, the ratio of the power gain for the fundamental mode and the higher order mode scales as $(\Omega_{0,0,0} \sin \Omega_{1,0} T / \delta\Omega_{1,1,0} \sin \delta\Omega_{1,1,0} T)^2$. Note also that, for the high betatron frequency limit $\delta\Omega_{1,1,0} < 0.6\Omega_{0,0,0}$ for any wavelength. This has interesting consequences for the transverse coherence properties of the longitudinal space-charge amplifier.

For $\Omega_{1,0}\omega_p L_d \ll \pi/2$, the ratio of the gain for the two modes scales as $g_{0,0,0}/g_{1,1,0} \propto (\Omega_{0,0,0}/\delta\Omega_{1,1,0})^4$ and the amplification of the higher order mode is strongly suppressed with respect to the fundamental mode. In this case, the effect of betatron motion is that of increasing the transverse coherence of the microbunching by suppressing the gain on the high-order modes. This effect will be particularly noticeable when starting from shot-noise, which couples strongly to a great number of transverse modes.

In cases in which $\Omega_{1,0}\omega_p L_d \simeq \pi$ the plasma frequency reduction induced by betatron motion can be employed to selectively amplify higher order modes. In this case, in fact, the gain of the fundamental mode is null, while the high order mode undergoes a significant amplification. As mentioned in Section 3.5, this effect could be employed in an advanced FEL seeding scheme for the generation of light with orbital angular momentum [44]

5.6 Conclusions

In this chapter we have developed a three-dimensional kinetic model of the longitudinal space-charge microbunching instability. Our analysis is based on the modal decomposition of the phase-space perturbation developed in chapters 3 and 4. We derive a general formalism for the microbunching induced by longitudinal space-charge for a beam with finite emittance, energy spread, betatron motion and finite transverse size.

The general formalism is employed to find closed form expressions for the microbunching gain for the fundamental plasma eigenmode starting from both a coherent density modulation or shot-noise.

Finally we employed our model to describe a specific experimental scenario corresponding to the compressed NLCTA electron beam. We derive a closed form solution for the microbunching gain in the case of a cold beam which we use to describe the spectral properties of the LSCA. We show how emittance can suppress the microbunching for strong beam focusing, an effect which is due to the emittance induced Landau damping of the space-charge oscillations. We show how our theoretical model can be employed for the design and optimization of a space-charge experiment, again with the example of the NLCTA beamline. Finally we briefly discuss the effect of betatron motion on the amplification of higher order transverse modes and its impact on the transverse coherence properties of a LSCA.

CHAPTER 6

Quasi-Three-Dimensional Analysis of Space-Charge Induced Optical Microbunching

In the previous sections, we have derived an analysis of longitudinal space-charge interactions based on a modal expansion in six-dimensional phase-space. In the 1-D limit, in which the plasma eigenmodes are totally degenerate, the modal expansion is highly impractical since many transverse modes need to be included to describe the transverse distribution of the beam microbunching. In this case, it is more convenient to give a local description of the process in a so-called quasi three-dimensional model. The the analysis contained in this chapter was published in [30].

In the high-frequency regime, the transverse beam size fulfills the condition $\sigma_x \gg \gamma\lambda/2\pi$, where σ_x is the root mean square transverse size of the electron beam, λ is the wavelength of interest and the Lorentz factor γ is the energy of the electron beam normalized to mc^2. In this limit, the Fourier components of the electric field generated by an uncorrelated electron distribution have a transverse correlation area which is much smaller than the electron beam section [20]. Under these conditions, the collective physics of the electron beam can be treated in analogy to an unbounded uniform plasma. In this context, it is useful to work in the spatial frequency domain in three-dimensions and define the bunching factor with an angular dependence [21]:

$$B = \frac{1}{N}\sum_{n=1}^{N} e^{-ik(z_n+\sin\theta(x_n\cos\phi+y_n\sin\phi))} \tag{6.1}$$

where N is the number of particles in the electron bunch, θ and ϕ are, respectively, the polar and azimuthal angles relative to the beam propagation axis z, z_n is the longitudinal position along the bunch of the n-th particle and x_n and y_n are the transverse positions. With this definition, the bunching factor is effectively the three-dimensional Fourier transform of the electron density and accounts for any transverse structure in the micro-bunched beam.

A detailed computation of the angular distribution of the micro-bunching is of fundamental importance since the angular spectra of the radiation processes used to experimentally diagnose this effect, such as coherent optical transition radiation, are extremely sensitive to the transverse structure of the micro-bunched distribution. With the assumption of transverse laminar motion, the micro-bunching geometry matches that of the longitudinal space-charge fields, yielding an angular width for the micro-bunching gain of $\theta_c = 1/\gamma$ [21]. Emittance effects in space-charge interactions, however, significantly modify the transverse structure of the micro-bunching pattern, and a kinetic treatment of the interaction between electrons and space-charge fields is needed to fully understand the physics of longitudinal space-charge-induced micro-bunching in this limit.

In this chapter, we show that in the high frequency limit, with the assumption that longitudinal motion is quasi-laminar, the problem of space-charge interactions leading to micro-bunching growth becomes formally equivalent to that of one-dimensional plasma oscillations in a warm electron plasma. The theory of such electrostatic oscillations in thermal plasmas has been discussed in two seminal papers by Landau [38] and Jackson [4]; our present work represents a new application of these venerated techniques of mathematical physics in a radically different context than the one considered in the original papers. We show that transverse emittance induces strong Landau damping at high transverse spatial frequencies, significantly narrowing the angular width of the micro-bunching gain with respect to the characteristic angular width of the space-charge fields. Finally we compare the results of our analysis and those of high resolution molecular dynamics simulations, capable of investigating spatial features in the fields below the mean inter-particle distance.

6.1 Longitudinal Space-Charge Induced Micro-bunching in the High-Frequency Limit

In this section we derive the equations that describe the formation of micro-bunching starting from shot-noise through the effect of collective longitudinal space-charge forces. We base this analysis on the Vlasov equation, a kinetic approach that is appropriate for a warm plasma in which the number of beam electrons acting collectively to produce the electric and magnetic fields is much larger than unity. This is true when the condition $n_0\gamma^2\lambda^3 >> 1$ applies, where n_0 is the electron density and λ is the wavelength of interest. This condition is equivalent to requiring that the wavelength of interest, as seen in the beam's rest frame $\gamma\lambda$, is much bigger than the rest frame mean inter-particle distance $(\gamma/n_0)^{1/3}$. Obviously this approach precludes the possibility of describing beam crystallisation processes, which require an analysis of particle to particle correlations on the scale of the mean inter-particle distance in the beam's reference frame. Such analysis is the subject of current investigation and we will not discuss it here.

To aid in analysis and to compare to previous theoretical work, we assume a coasting (non-accelerating) beam with constant current. We also limit ourselves to the high-frequency limit of space-charge interactions ($\sigma_x >> \gamma\lambda/2\pi$). In the high-frequency limit, edge effects due to the finite transverse size of the beam can be neglected and the 0-th order charge density can be considered constant over the characteristic transverse scale of the problem.

Consistent with the current theoretical and experimental understanding of the process, we model the formation of micro-bunching as follows: the electron beam initially undergoes an external-force-free drift and space-charge generates an energy modulation starting from shot-noise. After the drift the electrons go through a series of optical elements which rearrange their longitudinal and transverse phase space coordinates according to a given transfer matrix R_{ij}. The electron beam particle distribution is described by a six-dimensional distribution function $f(\vec{x}_\perp, z, \vec{\beta}_\perp, \eta, \tau)$. Where $\vec{x}_\perp$ is the transverse position, z is the longitudinal position in the beam coordinate system, $\vec{\beta}_\perp$ is the transverse velocity normalized to the speed of light, $\eta = \Delta\gamma/\gamma$ is the relative energy deviation and $\tau = ct$ where c is the speed of light and t is the time, measured from the beginning of the interaction. The distribution function is normalized to the total number of particles N.

We expand the distribution function to first order in perturbation theory: $f = f_0 + f_1$, with $|f_1| << |f_0|$. In the high-frequency limit we can specify the following form for the 0-th order distribution function: $f_0 = n_0 f_v(\vec{\beta}_\perp, \eta)$, where n_0 is the local average particle density. For simplicity we assume that f_v is isotropic in transverse velocity. Also, for simplicity, we will assume that n_0 is independent of time. This assumption is reasonable if the interaction happens close to a waist and the maximum distance from the waist is significantly shorter than the minimum β-function. If the waist is at the center of the drift the following condition has to apply: $L_d < \sigma_{x,0}/\sigma_{\beta,0}$, where L_d is the length of the drift and $\sigma_{x,0}$ and $\sigma_{\beta,0}$ are, respectively, the root mean square (RMS) transverse size of the beam and the transverse velocity spread (normalized to c) at the waist. If this condition does not apply, a possible solution is that of defining an equivalent drift length [21], shorter than the actual drift length, over which the beam density can be considered constant. In this chapter we will not be concerned with this problem and we will assume that the condition $L_d < \sigma_{x,0}/\sigma_{\beta,0}$ is verified, leaving a detailed study of the effect of density variation for future investigation.

The collective beam dynamics in the drift are described by the Vlasov equation, coupled to the Maxwell equations. In the coasting beam case, we may derive the fields from the scalar potential computed in the beam rest frame. With these underlying assumptions the linearized Vlasov equation for the electrons in the drift reads:

$$\frac{\partial f_1}{\partial \tau} + \vec{\beta}_\perp \cdot \nabla_\perp f_1 + \frac{\eta}{\gamma^2}\frac{\partial f_1}{\partial z} + \frac{F_z}{\gamma mc^2} n_0 \frac{\partial f_v}{\partial \eta} + \frac{\vec{F}_\perp}{\gamma mc^2} \cdot n_0 \frac{\partial f_v}{\partial \vec{\beta}} = 0 \tag{6.2}$$

where the approximation $\frac{dz}{d\tau} \approx p/\gamma^2$, valid for relativistic electrons has been used. F_z and $\vec{F}_\perp$ are respectively the longitudinal and transverse forces generated by the collective electric and magnetic fields of the electrons and can be computed solving Poisson's equation in the beam rest frame, where self-magnetic fields are negligible:

$$\left[{\nabla_\perp}^2 + \frac{1}{\gamma^2}\frac{\partial^2}{\partial z^2}\right]\phi = \frac{e}{\gamma \epsilon_0}\int f_1 d\eta d^2\vec{\beta}. \tag{6.3}$$

Longitudinal forces are Lorentz invariant while transverse forces transform as $F_\perp \to F_\perp/\gamma$ going from the beam rest frame to the laboratory frame, we then have: $F_z = \frac{e}{\gamma}\frac{\partial \phi}{\partial z}$ and $\vec{F}_\perp = \frac{e}{\gamma}\nabla_\perp \phi$.

It is convenient to solve equations (6.2) and (6.3) in the Laplace-Fourier domain. We give the following definitions:

$$\hat{f}_1 = \int f_1 e^{-i\left(k_z z + \vec{k}_\perp \cdot \vec{x}\right)} dz d^2\vec{x} \tag{6.4}$$

$$\tilde{\hat{f}}_1 = \int_0^\infty \hat{f}_1 e^{-s\tau} d\tau \tag{6.5}$$

and similarly for F_z and $\vec{F}_\perp$. Since the system is isotropic in the transverse dimension we can set $\vec{k}_\perp = \hat{x} k_x$ without loss of generality. We also work in the paraxial approximation and set $k_z = k$ and $k_x = \theta k$. With the above definitions, the Laplace-Fourier transform of equations (6.2) and (6.3) yields:

$$\begin{aligned} & s\tilde{\hat{f}}_1 - \hat{f}_1\Big|_{\tau=0} + i(k\theta\beta_x + k\frac{\eta}{\gamma^2})\tilde{\hat{f}}_1 \\ & + \frac{1}{\gamma m c^2} n_0 \left(\tilde{\hat{F}}_z \frac{\partial f_v}{\partial \eta} + \tilde{\hat{F}}_x \frac{\partial f_v}{\partial \beta_x}\right) = 0 \end{aligned} \tag{6.6}$$

$$\tilde{\hat{F}}_z = -\frac{i}{k}\frac{e^2}{\epsilon_0}\frac{1}{1+(\gamma\theta)^2}\int \tilde{\hat{f}}_1 d\eta d^2\vec{\beta} \tag{6.7}$$

$$\tilde{\hat{F}}_x = \theta \tilde{\hat{F}}_z \tag{6.8}$$

where $\hat{f}_1\Big|_{\tau=0}$ is the spatial Fourier transform of the initial value of f_1.

From Eqs. 6.6 and 6.8 we can express $\tilde{\hat{f}}_1$ in terms of $\tilde{\hat{F}}_z$:

$$\tilde{\hat{f}}_1 = \frac{1}{s + ik(\theta\beta_x + \frac{\eta}{\gamma^2})}\left(\hat{f}_1\Big|_{\tau=0} - \frac{n_0}{\gamma m c^2}\tilde{\hat{F}}_z\left(\frac{\partial f_v}{\partial \eta} + \theta\frac{\partial f_v}{\partial \beta_x}\right)\right). \tag{6.9}$$

Inserting Eq. (6.9) into (6.6), recalling that $\tilde{\hat{F}}_z$ does not depend on p and $\vec{\beta}$, we have:

$$\tilde{\hat{F}}_z = -\frac{i}{k}\frac{e^2}{\epsilon_0 \epsilon_p}\frac{1}{1+(\gamma\theta)^2}\int \frac{\hat{f}_1\Big|_{\tau=0}}{s_j + ik\left(\theta\beta_x + \frac{\eta}{\gamma^2}\right)} d\eta d^2\vec{\beta}. \tag{6.10}$$

where ϵ_p is the beam's plasma dielectric function defined as:

$$\epsilon_p = 1 + \frac{\omega_p^2}{c^2(1+(\gamma\theta)^2)}\frac{\gamma^2}{ik}\int \frac{\frac{\partial f_v}{\partial \eta} + \theta \frac{\partial f_v}{\partial \beta_x}}{s + ik\left(\theta\beta_x + \frac{\eta}{\gamma^2}\right)} d\eta d^2\vec{\beta} \tag{6.11}$$

with $\omega_p^2 = \frac{e^2 n_0}{\epsilon_0 m \gamma^3}$ being the relativistic beam plasma frequency.

Inserting Eq. (6.10) back into Eq. (6.9), after some algebraic manipulation, we obtain the following expression for the first order distribution function:

$$\tilde{\hat{f}}_1 = \frac{1}{s + ik(\theta\beta_x + \frac{\eta}{\gamma^2})}\left(\hat{f}_1\Big|_{\tau=0} - \frac{1}{\epsilon_p}\frac{\omega_p^2}{c^2(1+(\gamma\theta)^2)}\left(\frac{\partial f_v}{\partial \eta} + \theta\frac{\partial f_v}{\partial \beta_x}\right)\frac{\gamma^2}{ik}\int \frac{\hat{f}_1\Big|_{\tau=0}}{s + ik(\theta\beta_x' + \frac{\eta'}{\gamma^2})} d\eta' d^2\vec{\beta}'\right) \tag{6.12}$$

In what follows it will be understood that all the above integrals are analytically continued in the complex variable s to the half-plane $\Re[s] < 0$.

In performing the inverse Laplace transform we will only consider the zeros of the plasma dielectric function since these are the poles that describe the collective response of the electrons. Also, for the moment, we will only retain the R_{56} matrix element in the transport matrix describing the optical elements after the drift. A more general treatment applicable to arbitrary linear phase space transformations is included in the appendix.

The bunching factor in the frequency domain is defined as the Fourier transform of the density perturbation normalized to the number of particles, i.e.:

$$B(k_z, \vec{k}_\perp) = \frac{1}{N}\int f_1 e^{-i(k_z z + \vec{k}_\perp \cdot \vec{x})} dz d^2\vec{x} d\eta d^2\vec{\beta}. \tag{6.13}$$

In order to arrive at the final prediction for the bunching factor, after the space-charge forces have modulated the particle energy distribution, we must account for the effect of longitudinal dispersion due to systems of bending elements (e.g. magnetic chicanes). The effect of the longitudinal dispersion, modeled through the R_{56} matrix element, is that of shifting each particle's longitudinal position by an amount proportional to its energy deviation, i.e. $z \to z + \eta R_{56}$. The effect of this transformation on the spatial Fourier components of the distribution function is that of introducing a phase shift proportional to the spatial rearrangement: $\hat{f}_1 \to \hat{f}_1 e^{-ik\eta R_{56}}$.

It follows that the bunching factor after the particles' rearrangement following the drift, can be expressed as:

$$B = -\frac{1}{N}\sum_j e^{s_j L_d} \frac{1}{\frac{\partial \epsilon_p}{\partial s}\Big|_{s=s_j}} \frac{\omega_p^2}{c^2(1+(\gamma\theta)^2)} \frac{\gamma^2}{ik}$$
$$\int \frac{e^{-ik\eta R_{56}}(\frac{\partial f_v}{\partial \eta} + \theta \frac{\partial f_v}{\partial \beta_x})}{s_j + ik\left(\theta\beta_x + \frac{\eta}{\gamma^2}\right)} d\eta d^2\vec{\beta} \int \frac{\hat{f}_1\Big|_{\tau=0}}{s_j + ik\left(\theta\beta_x + \frac{\eta}{\gamma^2}\right)} d\eta d^2\vec{\beta} \tag{6.14}$$

where L_d is the length of the drift and the sum is performed over all the zeros s_j of the plasma dielectric function.

Integrating the first integral on the right-hand side of Eq. (6.14) by parts in η, and retaining only the term proportional to R_{56}, that accounts for the micro-bunching enhancement due to the longitudinal rearrangement, we obtain:

$$B_{R_{56}} = -\frac{1}{N}\sum_j e^{s_j L_d} \frac{1}{\frac{\partial \epsilon_p}{\partial s}\Big|_{s=s_j}} \frac{\omega_p^2 R_{56}\gamma^2}{c^2(1+(\gamma\theta)^2)}$$
$$\int \frac{e^{-ik\eta R_{56}} f_v}{s_j + ik\left(\theta\beta_x + \frac{\eta}{\gamma^2}\right)} d\eta d^2\vec{\beta} \int \frac{\hat{f}_1\Big|_{\tau=0}}{s_j + ik\left(\theta\beta_x + \frac{\eta}{\gamma^2}\right)} d\eta d^2\vec{\beta}. \tag{6.15}$$

Finally, if the initial value of the perturbation f_1 results from shot-noise, representing the individual particle positions in terms of δ-functions, we may write the final integral in Eq. 6.15 as:

$$\int \frac{\hat{f}_1\Big|_{\tau=0}}{s + ik\left(\theta\beta_x + \frac{\eta}{\gamma^2}\right)} d\eta d^2\vec{\beta} = \sum_{n=1}^{N} \frac{e^{-i(kz_n + k\theta x_n)}}{s + ik\left(\theta\beta_{x,n} + \frac{\eta_n}{\gamma^2}\right)}\Bigg|_{\tau=0} \tag{6.16}$$

where the particle positions are assumed random.

6.2 The Laminar and Quasi-Laminar beam cases

Before proceeding to discuss the general case of interest in this chapter, that of a transversely warm beam, we first examine analytically the limiting cases in which transverse thermal effects play a small role. To that end, in this section we derive a closed form expression for the micro-bunching in two simplified cases: the laminar and quasi-laminar beam.

In the laminar beam approximation, where to lowest order particles are fixed in beam-frame position with respect to each other, we may write $f_v = \delta(\eta)\delta^2(\vec{\beta})$. In this case the plasma dielectric function can be easily computed analytically:

$$\epsilon_p = 1 + \frac{\omega_p^2}{c^2}\frac{1}{s^2}. \tag{6.17}$$

The zeros of ϵ_p are $s_\pm = \pm i\omega_p/c$. Inserting $s_\pm$ in equation (6.15) we get:

$$\begin{aligned} B_{R_{56}} =& - B_0\gamma^2 R_{56}\frac{\omega_p}{c(1+(\gamma\theta)^2)}\sin\left(\frac{\omega_p}{c}L_d\right) \\ \approx& -b_0\left(\frac{(\gamma\omega_p)^2}{c^2(1+(\gamma\theta)^2)}\right)R_{56}L_d \end{aligned} \tag{6.18}$$

where $B_0 = \frac{1}{N}\sum_{n=1}^{N} e^{-i(kz_n+k\theta x_n)}\Big|_{\tau=0}$, with z_n and x_n being randomly distributed, is the shot-noise bunching factor and we have made the approximation $\omega_p L_d/c << 1$.

To describe the quasi-laminar beam approximation, we assume the following form of velocity distribution: $f_v = \frac{1}{(2\pi)^{3/2}\sigma_\beta^2\sigma_\eta} e^{-\frac{\eta^2}{2\sigma_\eta^2}-\frac{\vec{\beta}^2}{2\sigma_\beta^2}}$ with $k\sigma_\eta/\gamma^2 << \omega_p/c$ and $k\theta\sigma_\beta << \omega_p/c$. These assumptions mean that the electron displacement due to thermal motion in a plasma period ($\tau_p = 2\pi/\omega_p$) is much smaller than the wavelength $\lambda = 2\pi/k$ longitudinally and λ/θ transversely. Since the plasma oscillation period sets the time scale for space-charge effects, thermal effects become negligible when the thermal displacement in a plasma period is smaller than the length scale of the problem.

With this assumption, the plasma dielectric function is approximately equal to that found in the cold beam case and the bunching factor is given by:

$$\begin{aligned} B_{R_{56}} =& -B_0\left(\frac{\gamma^2\omega_p R_{56}\sin\frac{\omega_p L_d}{c}}{c(1+(\gamma\theta)^2)}\right)e^{-\frac{(k\sigma_\eta R_{56})^2}{2}} \\ &\approx -B_0\left(\frac{(\gamma\omega_p)^2}{c^2(1+(\gamma\theta)^2)}\right)R_{56}L_d e^{-\frac{(k\sigma_\eta R_{56})^2}{2}}. \end{aligned} \tag{6.19}$$

Finally, the micro-bunching gain is defined as the ratio of the statistical averages of the absolute values squared of the final to original bunching factor $g = < |B_{R_{56}}|^2 > / < |B_0|^2 > = N < |B_{R_{56}}|^2 >$ and it is equal to:

$$\begin{aligned} g =& \left(\frac{\gamma^2\omega_p R_{56}\sin\frac{\omega_p L_d}{c}}{c(1+(\gamma\theta)^2)}\right)^2 e^{-(k\sigma_\eta R_{56})^2} \\ &\approx \left(\left(\frac{\gamma\omega_p}{c}\right)^2\frac{1}{1+(\gamma\theta)^2}R_{56}L_d\right)^2 e^{-(k\sigma_\eta R_{56})^2}. \end{aligned} \tag{6.20}$$

In both the laminar and quasi-laminar beam approximations, the electron thermal motion can be considered frozen on the scale of a plasma period. Thus, the micro-bunched distribution is transversely correlated on the same scale as the longitudinal Fourier components of the electric field generated by shot noise: $\gamma\lambda/2\pi$ (with $\lambda = 2\pi/k$ equal to the wavelength of interest). This results in a cut-off angle of $\theta_c = 1/\gamma$ in the micro-bunching gain.

Note that the same result (up to a geometric factor due to the assumptions on the 0-th order charge density) has been obtained previously in [21].

6.3 The transversely warm beam case

In this section we treat the case that is most often found in experimental scenarios of interest: that of a beam that is transversely warm but longitudinally quasi-laminar, i.e. we keep the assumption $k\sigma_\eta/\gamma^2 \ll \omega_p/c$ but we make no assumptions on σ_β. Since space-charge forces naturally yield an angular cut-off of $1/\gamma$, transverse temperature effects will be important only if $k\sigma_\beta > \gamma\omega_p/c$, which is applicable for many relevant experimental situations.

By performing a double integration by parts (in η and in β_x) in the term proportional to $\frac{\partial f_v}{\partial \eta}$ in (6.11), and performing the integration in $d\eta$ and $d\beta_y$, the plasma dielectric function can be expressed as:

$$\epsilon_p = 1 + \frac{\omega_p^2}{c^2}\frac{1}{ik\theta}\int_{\tilde{c}} \frac{\frac{\partial f_v}{\partial \beta_x}}{s + ik\left(\theta\beta_x\right)} d\beta_x. \tag{6.21}$$

In the case of a warm beam, the analyticity of ϵ_p as a function of the complex variable s has to be enforced by deforming the integration path in (6.21) so that it runs in the complex plane below the singularity at $\beta_x = -s/ik\theta$ as shown in figure 6.1 (the resulting integration path is usually referred to as Landau contour [38] and we will denote it $\tilde{c}$).

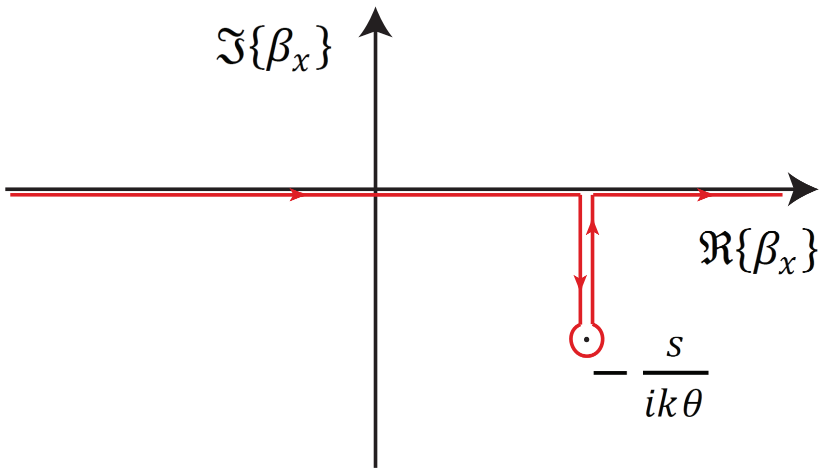

Figure 6.1: Landau contour in the complex β_x plane. The deformation of the integration path makes the plasma dielectric function analytical as a function of s.

The zeros of the plasma dielectric function, in this case, cannot be expressed in closed form. It is then useful to express equation (6.21) in dimensionless form. We give the following definitions: $k_D = \omega_p / c\sigma_\beta$ is the Debye wave-number, which we employ to normalize the transverse wave-number as $K = k\theta/k_D$; the Laplace variable s is normalized to the plasma frequency as $\Omega = -cs/i\omega_p$; finally, we normalize the transverse velocity to the thermal velocity spread: $B = \beta_x/\sigma_\beta$, $F = \frac{1}{(2\pi)^{1/2}} e^{-\frac{B^2}{2}}$. Note that the Debye wavelength $\lambda_D = 2\pi/k_D$ is the transverse thermal displacement in a plasma period and is the fundamental parameter that describes thermal effects in warm plasmas. The resulting scaled beam plasma dielectric function is then

$$\epsilon_p = 1 - \frac{1}{K^2} \int_{\tilde{c}} \frac{\frac{\partial F}{\partial B}}{B - \frac{\Omega}{K}} dB. \tag{6.22}$$

Note that the plasma dielectric function, as a function of Ω, depends only on one external dimensionless parameter K. Since longitudinal thermal effects have been neglected and the system is azimuthally symmetric, this three-dimensional problem reduces formally to that of one-dimensional plasma oscillations discussed in [4].

The zeros Ω_j of (6.22) can be found numerically [4] and are, in general, complex. The imaginary part of the scaled frequency Ω_j is always negative, resulting in an exponential decay of the micro-bunching as a function of the drift length (this collisionless damping process due to thermal motion is usually denoted Landau damping). Also, if $\Omega_R - i\Omega_I$ is a solution (with Ω_R, Ω_I positive real numbers), then $-\Omega_R - i\Omega_I$ is also a solution [4]. We will thus denote as $\Omega_\pm$ the two dominant roots of the dielectric function (i.e. the roots with the smallest damping constant).

To develop an intuition on the physical processes involved, we examine Figure 6.2 which shows the real and imaginary parts of the dominant root Ω_+ (see also [4]). The imaginary part of $-\Omega_+$ is a growing function of K. For small values of K the damping constant $-\Im\{\Omega_+\}$ is small and can be neglected for drifts that are significantly shorter than a plasma wavelength, as is usual in most experimental situations. However, for $K > 1$ the damping term is significantly bigger than 1, resulting in a strong suppression of the micro-bunching gain at angles bigger than k_D/k. Equivalently, one could state that a transversely warm electron beam is unable to develop transverse structures on a scale that is smaller than $\lambda_D = 2\pi c\sigma_\beta/\omega_p$ under the effect of longitudinal space-charge forces.

To find the actual angular dependence of the micro-bunching gain we must compute the square of the absolute value of (6.15) and perform a statistical average. It can be shown that equation (6.15), with the above approximations,

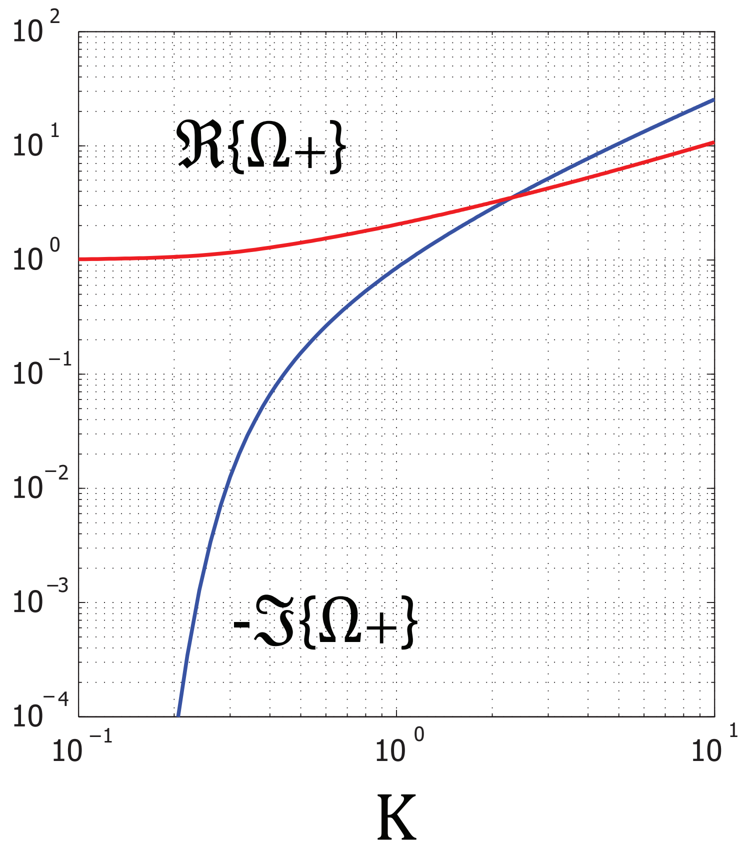

Figure 6.2: Real part (red line) and imaginary part (blue line) of the roots of the plasma dielectric function for a transversely warm beam, as a function of the scaled wave-number K [4].

can be simplified to:

$$
\begin{aligned}
B_{R_{56}} = & - i\frac{\omega_p}{c(1+(\gamma\theta)^2)}\gamma^2 R_{56} e^{-\frac{(k\sigma_\eta R_{56})^2}{2}} \\
& \frac{1}{N}\sum_j e^{-i\Omega_j \frac{\omega_p}{c}L_d}\frac{K}{1-\frac{\Omega_j^2}{1+K^2}}\sum_{n=1}^{N}\frac{e^{-i(kz_n+k\theta x_n)}}{B_n-\frac{\Omega_j}{K}}.
\end{aligned} \tag{6.23}
$$

Taking the statistical average of the absolute value squared of (6.23), recalling that $< e^{-ik(z_n-z_m)-ik\theta(x_n-x_m)} >= \delta_{n,m}$ (where $\delta_{n,m}$ is the Kronecker delta), from the definition of micro-bunching gain we obtain:

$$
\begin{aligned}
g = & \left(\frac{\omega_p}{c(1+(\gamma\theta)^2)}\gamma^2 R_{56}\right)^2 e^{-(k\sigma_\eta R_{56})^2}\int dBF(B)\left(\sum_j e^{-i\Omega_j\frac{\omega_p}{c}L_d}\frac{K}{1-\frac{\Omega_j^2}{1+K^2}}\frac{1}{B-\frac{\Omega_j}{K}}\right) \\
& \left(\sum_{j'} e^{-i\Omega_{j'}\frac{\omega_p}{c}L_d}\frac{K}{1-\frac{\Omega_{j'}^2}{1+K^2}}\frac{1}{B-\frac{\Omega_{j'}}{K}}\right)^*.
\end{aligned} \tag{6.24}
$$

In the dominant pole approximation, we keep only the two dominant roots in the summation in (6.24). In this case, expression (6.24) can be simplified to:

$$
\begin{aligned}
g = & 2\left(\frac{\omega_p}{c(1+(\gamma\theta)^2)}\gamma^2 R_{56}\right)^2 e^{-(k\sigma_\eta R_{56})^2}\left(\left|\frac{Ke^{-i\Omega_+\frac{\omega_p}{c}L_d}}{1-\frac{\Omega_+^2}{1+K^2}}\right|^2\left(\left|\frac{K^2(1+K^2)}{\Omega_+^2}\right| - \sqrt{2\pi}K\frac{\Re\{e^{-\frac{\Omega_+^2}{2K^2}}\}}{\Im\{\Omega_+\}}\right)\right. \\
& \left. -\Re\left\{\left(\frac{Ke^{-i\Omega_+\frac{\omega_p}{c}L_d}}{1-\frac{\Omega_+^2}{1+K^2}}\right)^2\left(\frac{K^2(1+K^2)}{\Omega_+^2}-\sqrt{2\pi}K\frac{e^{-\frac{\Omega_+^2}{2K^2}}}{\Omega_+}\right)\right\}\right).
\end{aligned} \tag{6.25}
$$

Note that the quasi-laminar beam case corresponds to $|K| << 1$. It can be shown that in this limit $\Omega_+ \approx 1 + \frac{3}{2}K^2 - i\sqrt{\frac{\pi}{8}}e^{-\frac{1+3K^2}{2K^2}}/K^3$ [38, 4]. With this asymptotic expression, equation (6.25) reduces to (6.20).

6.4 Numerical Examples

As an example, we display a numerical evaluation of the angular dependence of the gain for the following beam parameters, corresponding to a typical electron beam produced by an RF photo-injector. We assume a uniform beam with a current of $I = 40$ A and an RMS envelope size of $\sigma_x = 85$ μm and an energy of 135 MeV ($\gamma = 270$). The length of the drift is $L_d = 4$ m.

Figure 6.3 shows the angular dependence of the micro-bunching gain for several values of σ_β for a wavelength of $\lambda = 0.5$ μm. We can see that for reasonable values of the emittance, transverse Landau damping can have an important role in the formation of micro-bunching, significantly reducing the angular width of the gain with respect to the laminar beam case. Note that, for the $1mm - mrad$ case we have $L_d \approx 2\sigma_{x,0}/\sigma_{\beta,0}$ and the results of the theory, in this case, are not accurate and should be interpreted with care.

6.5 Molecular Dynamics Simulations

Numerical modeling of space-charge induced optical micro-bunching at optical and sub-optical wavelengths is a challenging task since it requires high resolution and a great number of macro-particles. Ideally, to correctly reproduce shot-noise statistics in the electron distribution, each particle in the simulation should correspond to a particle in the beam. Also, resolution well below the optical spectrum is required to correctly compute the collective fields generated by the electrons.

Recently, the use of large computer clusters with parallel codes has allowed simulations with unprecedented resolution in the computation of self-fields, reaching down to the few μm level [49]. However, the resolution needed for optical

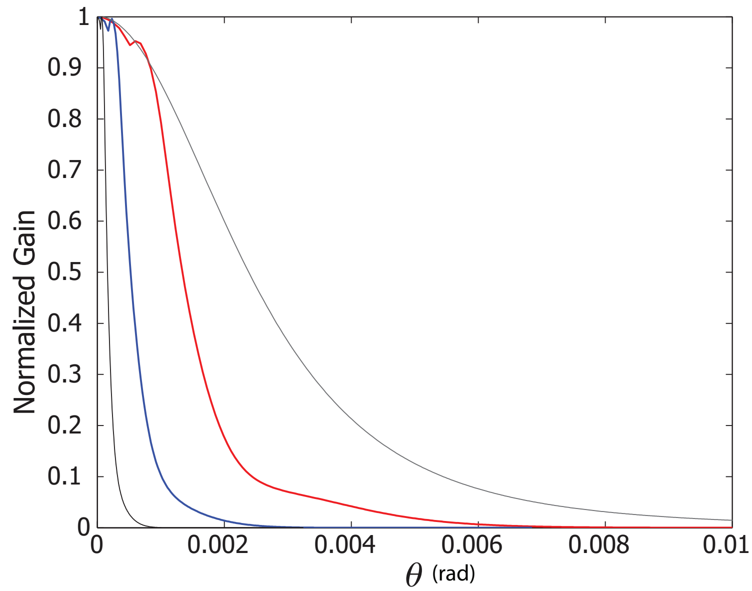

Figure 6.3: Angular dependence of micro-bunching gain for different values of σ_β corresponding to a normalized emittance of $\epsilon = 0$ (gray line), $\epsilon = 0.1$ mm-mrad (red line), $\epsilon = 0.5$ mm-mrad (blue line) and $\epsilon = 1$ mm-mrad (black line).

and sub-optical micro-bunching represents a serious challenge even for highly parallelized codes.

To model high-frequency space-charge phenomena with a low computational cost, we have created a code which computes the electron dynamics with periodic boundary conditions in all three dimensions. Periodicity allows to limit the simulation window to a small fraction of the beam (few μm in the longitudinal dimension and several tens to few hundreds of μm transversely depending on the energy) thus reaching the resolution required (few nm to few tens of nm longitudinally). Also, due to the periodic boundary conditions, the code works in the high-frequency limit (see figure 6.4) since edge-effects due to the finite size of the beam cannot be included. This limits the use of the code to very high-frequency

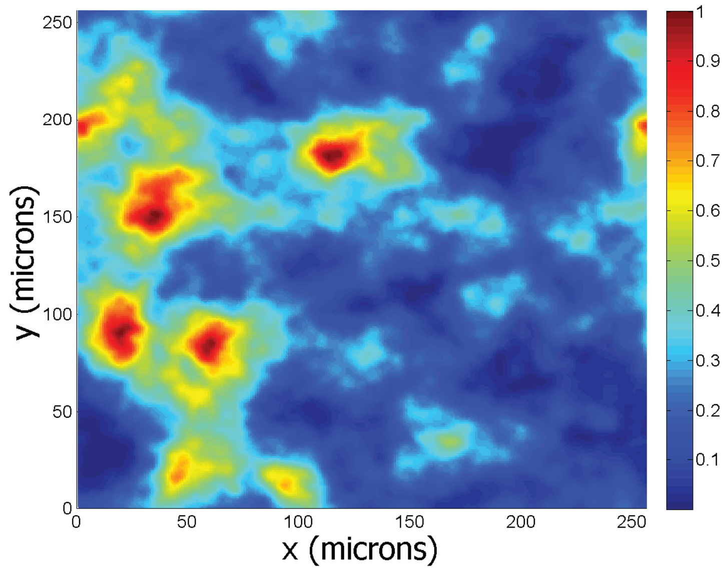

Figure 6.4: Longitudinal Fourier transform of the electric field (in arbitrary units) generated by an uncorrelated electron distribution for $\gamma = 270$ and $\lambda = 0.5\mu m$, illustrating the features of the high-frequency limit of space-charge fields.

phenomena.

The code has the capability of including external fields (accelerating and focusing) and internal fields. The high frequency components of the collective fields are computed solving Poisson's equation in the beam rest frame with discrete Fourier transform (DFT) methods.

We have performed simulations for the model assumed in section 6.1 with no acceleration but only a free drift with subsequent rearrangement through longitudinal dispersion. The beam parameters are those described in section 6.4.

Figure 6.5 shows the x-z trace space after longitudinal dispersion for two simulations with and without the effect of emittance. Note that in the zero emittance simulation, the position and size of the micro-bunches varies randomly with the transverse position, resulting in a broad angular width of the micro-

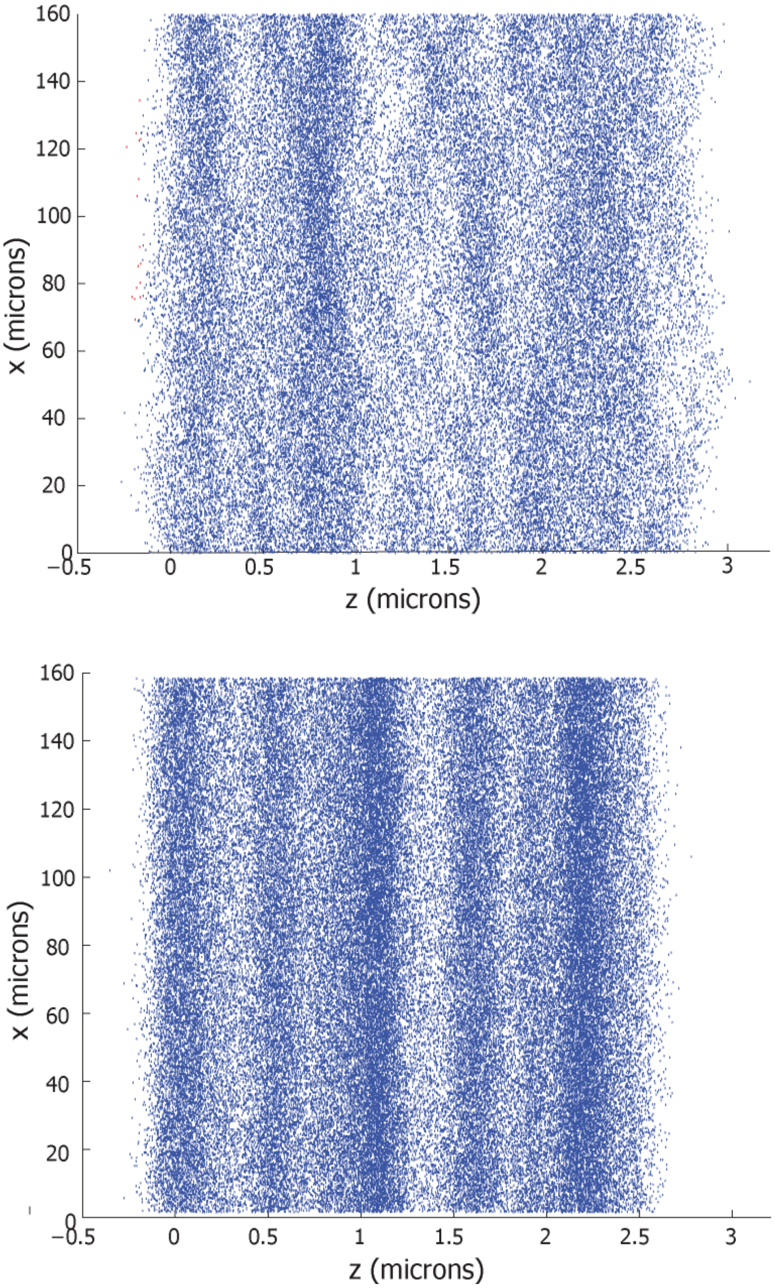

Figure 6.5: x-z trace space after a drift and longitudinal dispersion without emittance (upper plot) and with 1 mm-mrad emittance (lower plot) showing the effect of Landau damping on the transverse structure of micro-bunching.

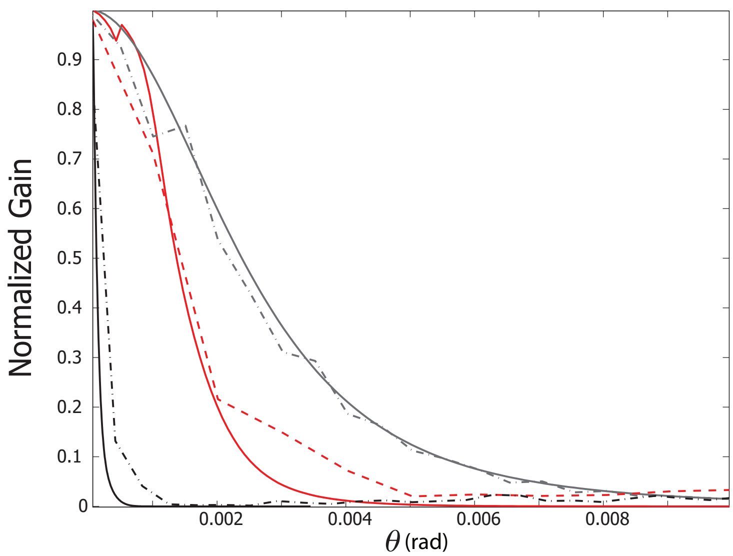

Figure 6.6: Theoretical results (solid lines) versus numerical simulations (dashed lines) for different values of σ_β corresponding to a normalized emittance of $\epsilon = 0$ (gray line), $\epsilon = 0.1$ mm-mrad (red line) and $\epsilon = 1$ mm-mrad (black line). The results of the simulations are averaged over 50 independent runs

bunching pattern.

Figure 6.6 shows a comparison between the results of the theoretical model and the numerical simulations. The two are in good agreement, validating the theoretical analysis described earlier.

6.6 Conclusions

In this chapter we discussed a kinetic analytical description of space-charge induced optical micro-bunching based on the beam plasma dielectric function.

The theory developed is fully three-dimensional and accounts for the angular dependence of the micro-bunching in the high-frequency limit. The kinetic approach allows for the inclusion of transverse thermal motion due to finite transverse emittance.

With the approximation that longitudinal motion is quasi-laminar, which holds for typical high brightness electron beam parameters, the problem can be treated with the same mathematical methods used to describe one-dimensional plasma oscillations in thermal plasmas, as discussed in the work from Landau and Jackson [38, 4]. In particular, the effect of Landau damping of transverse modes due to finite emittance has been discussed and found to be of great importance when typical values of emittance and beam plasma frequency are considered, significantly reducing the angular width of the micro-bunching gain with respect to the natural width $\theta_c = 1/\gamma$ of longitudinal space-charge fields.

With the further assumption of transverse quasi-laminar motion, the results of our theory agree with those derived in previous papers on the same subject [21].

Finally the results of our analysis have been compared to those generated by high resolution molecular dynamics simulations with periodic boundary conditions. The analytical and numerical results are found to be in good agreement, validating the theoretical analysis derived in this chapter.

6.A Derivation of the closed form expression for the micro-bunching gain

With the assumption of longitudinal quasi-laminar motion, equation (6.15) can be simplified taking advantage of the analytical properties of the plasma dispersion function, defined as $Z(\zeta) = \frac{1}{\sqrt{\pi}} \int_{\tilde{c}} dB \frac{e^{-B^2}}{B-\zeta}$. The plasma dispersion function is analytical in ζ in the whole complex plane and can be shown to have the following properties [4]:

$$Z(\zeta) = 2ie^{-\zeta^2} \int_{-\infty}^{i\zeta} e^{-x^2} dx \tag{6.26}$$

$$Z'(\zeta) = -2 - 2\zeta Z(\zeta) \tag{6.27}$$

where Z' is the complex derivative of Z and $erfc(\zeta)$ is the complex valued complementary error function.

Integrating by part the plasma dielectric function, we obtain:

$$\epsilon_p = 1 - \frac{1}{2K^2} Z' \left(\frac{\Omega}{\sqrt{2}K} \right). \tag{6.28}$$

Using equations (6.27) and (6.28) we can express the plasma dielectric function and all its derivatives at the zeros of the plasma dielectric function. In particular we have:

$$Z|_{\epsilon_p=0} = -\frac{1+K^2}{\Omega} K\sqrt{2} \tag{6.29}$$

$$Z'|_{\epsilon_p=0} = 2K^2 \tag{6.30}$$

$$Z''|_{\epsilon_p=0} = 2\sqrt{2}K \left(\frac{1+K^2}{\Omega} - \Omega \right). \tag{6.31}$$

Finally we express the integrals in 6.15 as a function of Z and its derivatives, with the approximation of longitudinal quasi-laminarity:

$$\int \frac{e^{-ikpR_{56}} f_v}{s_j + ik\left(\theta\beta_x + \frac{p}{\gamma^2}\right)} dp d^2\vec{\beta} \approx \frac{ce^{-\frac{(k\sigma_\eta R_{56})^2}{2}}}{iK\omega_p\sqrt{2}} Z\left(\frac{\Omega_j}{\sqrt{2}K}\right) \tag{6.32}$$

$$\frac{\partial \epsilon_p}{\partial s}|_{s=s_j} \approx \frac{c}{i2\sqrt{2}K^3\omega_p} Z''\left(\frac{\Omega_j}{\sqrt{2}K}\right). \tag{6.33}$$

Equation 6.15 follows immediately substituting equations (6.29) and (6.31) into equations (6.32) and (6.33).

The same method can be applied to derive equation (6.25). By computing the partial fractions expansion of the integrand in equation (6.24) we can reduce it to a sum of Z functions. Equation (6.25) then follows easily using the symmetry properties of Z:

$$Z(-\zeta) = -Z(\zeta) + 2i\sqrt{\pi}e^{-\zeta^2} \tag{6.34}$$

$$Z(\zeta^*) = Z^*(\zeta) + 2i\sqrt{\pi}e^{-\zeta^2}. \tag{6.35}$$

6.B Micro-bunching gain with transverse matrix elements

The model developed in the previous sections can be easily generalized to included transverse transport matrix elements. Note that the inclusion of cartesian matrix elements breaks the azimuthal symmetry of the problem even if the transverse velocity distribution is isotropic. It is then necessary to set-up the problem in a more general way. We adopt the following convention: $\vec{k} = k\hat{z} + k\theta\cos(\phi)\hat{x} + k\theta\sin(\phi)\hat{y}$. We also define $\beta_{\parallel}$ and $\beta_{\perp}$ the parallel and perpendicular components of transverse velocity with respect to $\vec{k}_{\perp}$. Finally we define $\tilde{k}_x = k(\theta\cos(\phi)R_{11} + R_{51})$, $\tilde{k}_y = k(\theta\sin(\phi)R_{33} + R_{53})$, $R_x = \theta\cos(\phi)R_{12} + R_{52}$ and $R_y = \theta\sin(\phi)R_{34} + R_{54}$. With these definitions, the derivation of the micro-bunching gain is similar to that of the previous sections with a few differences: $k\theta$ is now replaced by $\sqrt{\tilde{k}_x^2 + \tilde{k}_y^2}$ and the integral $\int \frac{e^{-ikpR_{56}}\frac{\partial f_v}{\partial p}}{s_j + ik\left(\theta\beta_x + \frac{p}{\gamma^2}\right)} dp d^2\vec{\beta}$ is replaced by $\int \frac{e^{-ikpR_{56}-ikR_x\beta_x-ikR_y\beta_y}\frac{\partial f_v}{\partial p}}{s_j+i\left(\sqrt{\tilde{k}_x^2+\tilde{k}_y^2}\beta_{\|}+\frac{p}{\gamma^2}\right)}dpd^2\vec{\beta}$. The final result is given by:

$$
\begin{aligned}
g = {} & 2\left(\frac{\tilde{\omega}_p}{c(1+\gamma^2(\frac{\tilde{k}_x^2+\tilde{k}_y^2}{k^2}))}\gamma^2 R_{56}\right)^2 e^{-(k\sigma_\eta R_{56})^2-k^2(R_x^2+R_y^2)\sigma_\beta^2} \\
& \Bigg(\left|\frac{KZ(\frac{\Omega_+}{\sqrt{2}K}+\frac{ik(R_x\cos(\phi)+R_y\sin(\phi))\sigma_\beta}{\sqrt{2}})e^{-i\Omega_+\frac{\tilde{\omega}_p}{c}L_d}}{\frac{(1+K^2)}{\Omega_+}-\Omega_+}\right|^2 \left(\left|\frac{K^2(1+K^2)}{\Omega_+^2}\right|-\sqrt{2\pi}K\frac{\Re\{e^{-\frac{\Omega^2}{2K^2}}\}}{\Im\{\Omega\}}\right) \\
& -\Re\left\{\left(\frac{KZ(\frac{\Omega_+}{\sqrt{2}K}+\frac{ik(R_x\cos(\phi)+R_y\sin(\phi))\sigma_\beta}{\sqrt{2}})e^{-i\Omega_+\frac{\tilde{\omega}_p}{c}L_d}}{\frac{(1+K^2)}{\Omega_+}-\Omega_+}\right)^2\left(\frac{K^2(1+K^2)}{\Omega_+^2}-\sqrt{2\pi}K\frac{e^{-\frac{\Omega_+^2}{2K^2}}}{\Omega_+}\right)\right\}\Bigg)
\end{aligned}
\tag{6.36}
$$

with the following substitution: $K = c\sigma_\beta\sqrt{\tilde{k}_x^2+\tilde{k}_y^2}/\omega_p$. Z is the called plasma dispersion function defined in appendix 6.A.

CHAPTER 7

Experimental Demonstration of a Cascaded Longitudinal Space-Charge Amplifier

The analysis discussed in chapters 3,4, 5 and 6 provides a strong theoretical background for the space-charge induced microbunching instability and for the Longitudinal Space-Charge Amplifier (LSCA).

Space-charge induced microbunching is a robust effect that happens over a broad frequency bandwidth. At short wavelengths, the spectral properties of this amplification mechanism are determined by thermal effects, with a cut-off caused by the phase mixing induced by energy spread, which results in the fast decaying term $e^{-(k\sigma_\eta R_{56})^2}$). At long wavelengths, instead, the amplification is suppressed by edge effects due to the finite size of the beam, which slow down the space-charge dynamics of the electrons when $D = k_z\sigma_x/\gamma < 1$. In an LSCA, the microbunching induced by the space-charge instability is optimized and employed in a downstream undulator for the emission of coherent radiation. As was discussed in the introductory chapters, since the space-charge insability has a broad amplification bandwidth, the LSCA can deliver intense broad-band radiation pulses, accessing operating regimes that are beyond the capabilities of currently operating free-electron lasers.

In this chapter we present the first experimental demonstration of a longitudinal space-charge amplifier at optical wavelengths. The experiment has been carried out at the Next Linear Collider Test Accelerator at SLAC. Our experimental setup employs the three-chicane Echo bemline [50, 51], which is customarily used for the generation of high-harmonic seeded microbunching via the echo mechanism. In our experiment, operating with a strongly compressed electron beam, we turn the NLCTA echo-beamline into a cascaded 3-stage LSCA, leading to strong amplification of shot-noise microbunching for the emission of broad-band coherent undulator radiation.

While the generation of coherent radiation induced by the microbunching instability was observed in the past in several FEL injectors, the optimization and control of the gain process demonstrated here are two crucial novelties, that pave the way for the generation of broad-band coherent pulses at fourth generation light sources. The most striking features of our experiment are the temporal and longitudinal coherence properties of the radiation pulses. We demonstrate the generation of radiation pulses with a single transverse mode and single spectral spike, which are indication of fully coherent photons. Both these features are related to the strong electron beam compression along the amplifier, leading to up-shifting of the microbunching frequency from the far-infrared to the optical scale and to the generation of a short microbunching structure.

7.1 The Next Linear Collider Test Accelerator

In this section we describe the experimental facility where the LSCA experiment was performed. The Next Linear Collider Test Accelerator (NLCTA) is a test facility located in the SLAC Accelerator Laboratory. The NLCTA is a mixed x-band/s-band accelerator which operates at energies up to 120 MeV. The beamline setup for the LSCA experiment is illustrated in Fig. 7.1 The electrons bunches are generated by radio-frequency (RF) gun, which is composed of a laser excited

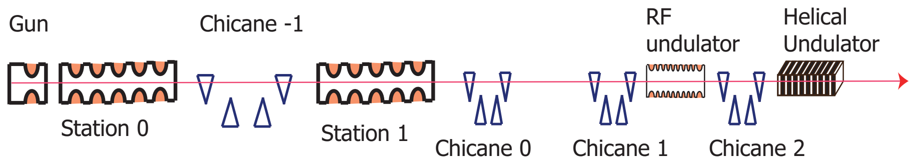

Figure 7.1: Overview of the NLCTA beamline for the LSCA experiment.

photocathode and a $5MeV$ s-band accelerating RF cavity. After the generation in the RF gun, the electrons are accelerated to energies of up to $E_1 = 60MeV$ by the first x-band accelerating cavity, referred to as station 0 (st0). After st0, the beam goes through a large magnetic chicane with tunable dispersion (chicane -1). Chicane -1 can be bypassed sending the beam through a straight drift section. The beam is then accelerated up to a final energy $E_{max} < 125MeV$ by a second x-band structure (st1).

The photoinjector delivers low emittance bunches ($\epsilon \simeq 1.1\mu m$) with a charge ranging from few pC to $\simeq 100pC$. The duration of the uncompressed bunches is $T_b \simeq 1psec$. Figure 7.2 shows a picture of the RF gun and of st1.

The space-charge amplifier setup is composed of three-magnetic chicanes, separated by drift-spaces, with an undulator after the last magnetic chicane. The three-magnetic chicanes (labeled chicane 0,1,2) have tunable dispersion, with a range $0.5mm < R_{56} < 10mm$ at 80 MeVs. The lower limit is set by three optical mirrors that are used, in the echo experiment, to inject and eject the two seed lasers, while the upper limit is set by the size of the vacuum pipe. The flexibility in the choice of the longitudinal dispersion is a key element to the experiment, since it allows to study several different modes of operation , as well as to give a direct demonstration of cascaded space-charge amplification.

The radiator is a helical undulator with 10 periods of length $\lambda_u = 1.9cm$ and an undulator parameter $K = 0.58$.

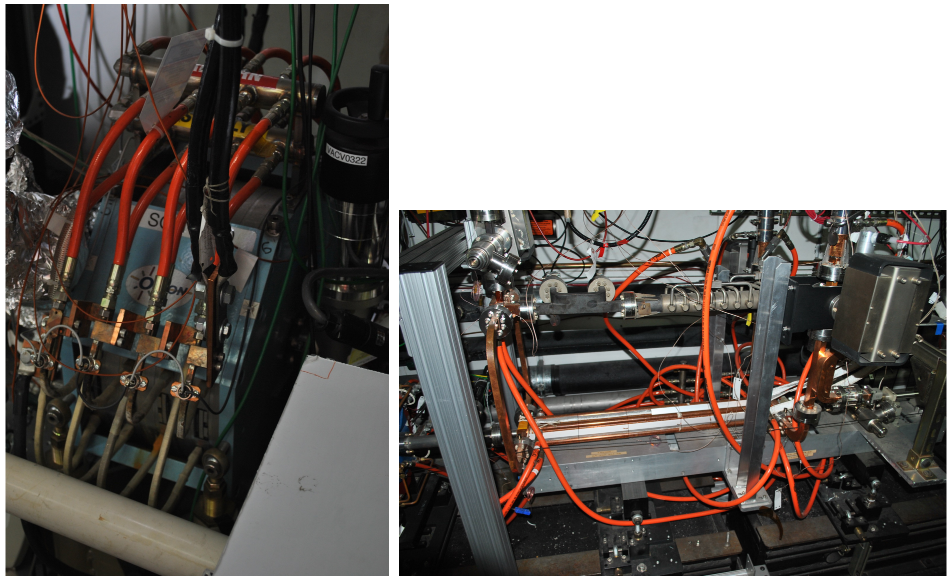

Figure 7.2: The NLCTA RF gun (left image) and the x-band accelerating structure st1 (right image).

The drift space between chicanes 1 and 2 is occupied by a 77 period radio-frequency undulator. The RF undulator was not used as the final radiator but only as a diagnostic for the microbunching. Unless otherwise noted, the RF undulator can be considered as a free-drift space for the scope of this experiment.

7.2 Space-charge gain in the compressed mode of operation at the NLCTA

The NLCTA injector generates electron bunches with currents of up to a few tens of Amperes. To achieve microbunching gain, longitudinal compression is required. At the NLCTA the electron beam is compressed inducing an energy chirp by accelerating off-crest in either of the accelerating sections. For reasons that will be explained later, we decided to bypass chicane -1 and compress in the last three-chicanes. This means that the compression mechanism happens during

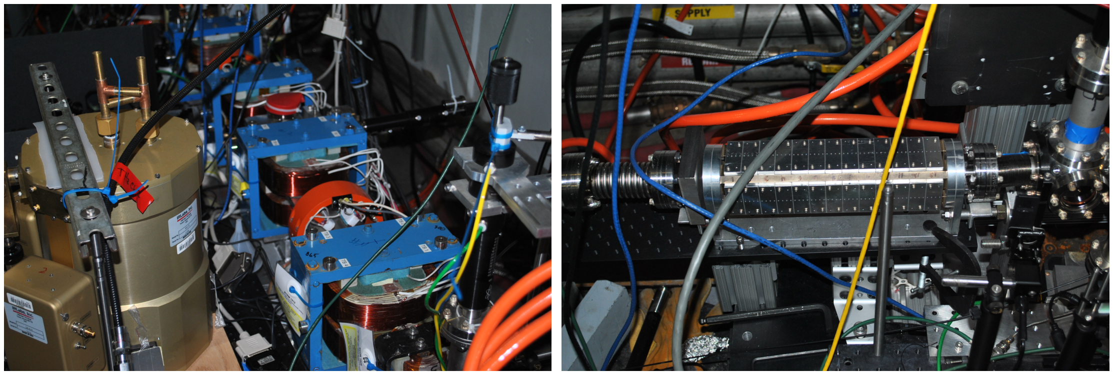

Figure 7.3: Chicane 2 (left image) and the helical undulator (right image).

the amplification process, which has important consequences for the coherence properties of the space-charge amplifier. In this section we will describe the chicane compression mechanism and its effect on microbunching gain.

7.2.1 Linear compression

In the idealized case of a linear energy-chirp and linear transport through the magnetic chicane, given a z-energy correlation $h = d\eta/dz$, the beam is compressed by the compression factor $C = 1/1 - hR_{56,tot}$, where $R_{56,tot}$ is the cumulative R_{56} of the transport beamline. When $hR_{56,tot} \simeq 1$, energy-spread effects become dominant, limiting the maximum compression factor achievable. For a gaussian uncorrelated energy distribution with uncorrelated relative energy-spread σ_η the shortest RMS beam length attainable with linear compression is $R_{56,tot}\sigma_\eta$. Fig. 7.4 shows a schematic representation of this idealized compression scheme.

An energy chirp can have a strong effect on the microbunching dynamics. If the beam has a periodic phase-space perturbation at the wavelength $\lambda = 2\pi/k_z$, the wavelength is shifted by the compression mechanism to $\lambda \to \lambda/C$ (see Fig 7.4). The microbunching gain is also affected by compression and the power-gain

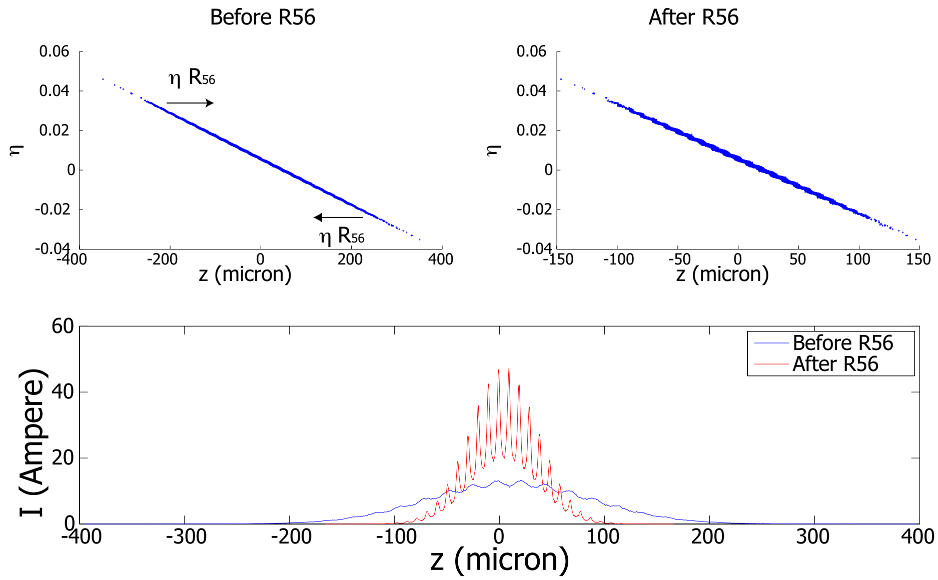

Figure 7.4: Schematics of the linear bunch compression mechanism.

formula for a beam with a linear chirp has to be modified as follows:

$$g = \left(\gamma^2 R_{56} C \Omega \frac{\omega_p}{c} \sin(\Omega \frac{\omega_p}{c} L_d) e^{-\frac{(C k_z \sigma_\eta R_{56})^2}{2}}\right)^2, \tag{7.1}$$

where, for simplicity, we have assumed the cold-beam limit and we have omitted the coupling coefficient Γ. The eigenvalue Ω has to be computed using the beam parameters before compression and the uncompressed wavelength k_z. Note that for a given final wavelength $k_{fin} = C k_z$, it is convenient to operate at strong compression, since the gain depends quadratically on the compression factor C. In the case of the three-stage amplifier discussed here the compression process happens gradually along the amplifier. For a given energy chirp, the total R_{56} is limited by the condition that the beam be not overbunched $hR_{56,tot} < 1$. The way the total R_{56} is distributed along the three amplification stages has important consequences on the amplification mechanism. In general it is convenient to work with decreasing values of dispersion, i.e. the first chicane should have the strongest dispersion and the last one should have the smallest. This point can be understood by considering that concentrating the larger part of the total dispersion at the first stage generates a high current that can be exploited to increase gain in the last two stages.

Operating a longitudinal space-charge amplifier with a chirped beam has important consequences on the transverse structure of the microbunching and, thus, on the transverse coherence of the radiation pulse emitted in the radiator. As discussed in the previous chapters, the space-charge eigenmodes of a laminar beam are fully degenerate for large values of the 3-D parameter $D = k_z \sigma_x / \gamma$, i.e. for short wavelengths. As a consequence of the full degeneracy, the transverse distribution of microbunching in this limit is composed of several uncorrelated speckles. This type of microbunching would radiate a transversely incoherent mode in the radiator. This effect limits the operation of an un-chirped LSCA to wavelengths $\lambda > \sigma_x / 2\pi\gamma$. For the typical operating condition of the NLCTA, this would limit the operation of the LSCA to far-infrared wavelengths. This problem can be overcome by operating the LSCA with an energy-chirped beam. In fact, due to beam compression, the optical microbunching generated at the last stage corresponds to the long wavelength microbunching generated at the first stage and frequency up-shifted by the compression mechanism in the second and third chicanes. As a result, the microbunching is transversely coherent and the beam radiates a single transverse mode in the undulator. A similar mechanism was proposed in [17] in the context of the generation of attosecond pulses in the soft x-ray region by laser-compression of UV microbunching.

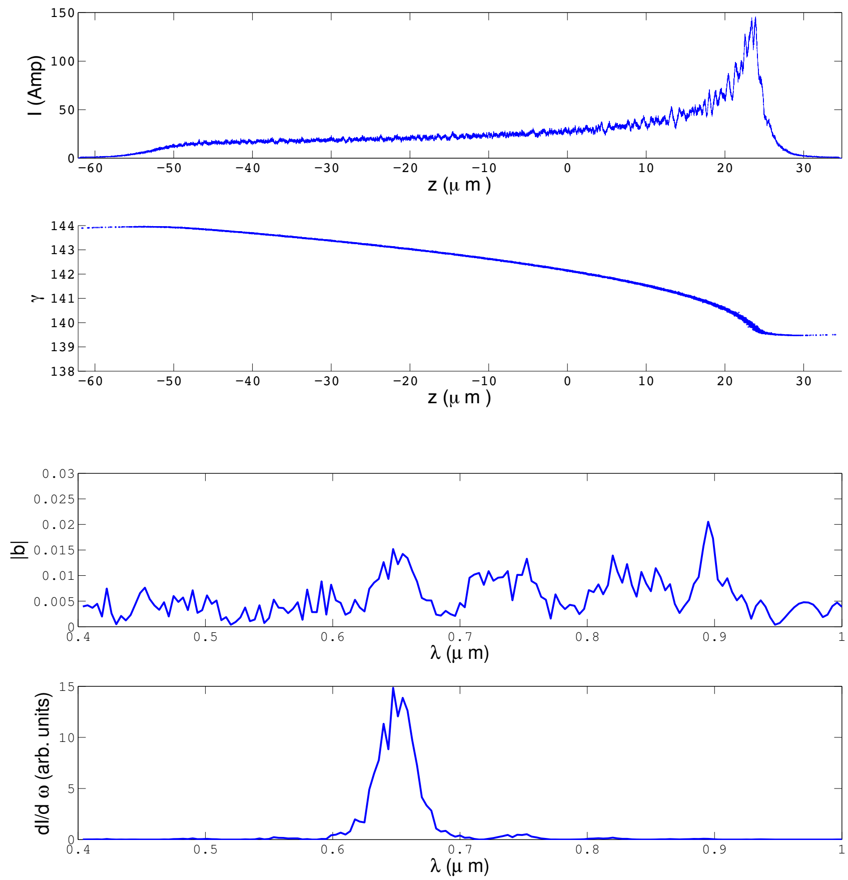

Figure 7.5: Simulated phase-space for the non-linear compression scheme at the NLCTA (first figure) and corresponding current distribution (second figure). The third figure shows the bunching factor as a function of wavelength while the fourth image shows the corresponding undulator radiation spectrum.

7.2.2 Non-linear compression

The linear model of beam compression that we described earlier is only accurate for very short beams with a small energy-spread. In more realistic cases, non-linear effects associated with a quadratic energy dependence induced by the accelerating fields, and to motion in the magnetic chicane should be taken into account. The first effect can be understood by looking at the z-dependence of the accelerating field $E_{rf} = E_0 cos\left(k_{rf}(z_l - ct)\right)$ (where z_l is the longitudinal coordinate along the accelerator), which generates a z-energy correlation of the type:

$$\delta\gamma = +\Delta\gamma \cos((k_{rf}z + \phi_{ACC})\,, \tag{7.2}$$

where $\delta\gamma$ is the energy gain of a particle traveling in the accelerating station, z is the longitudinal position along the electron bunch and ϕ_{ACC} is the accelerating phase of a reference particle at $z = 0$. This gives a non-linear energy-chirp: $\gamma = \gamma_0 + hz + h_2 z^2$, where $h = -k_{rf}\Delta\gamma \sin(\phi_{ACC})/\gamma_{av}$ and $h_2 = -k_{rf}^2 \Delta\gamma \cos(\phi_{ACC})/\gamma_{av}$, where γ_{av} is the mean energy at the exit of the accelerating station normalized to mc^2.

Non-linear effects in chicane transport can be modeled with the T_{566} and U_{5666} elements. The longitudinal coordinate change introduced by the magnetic chicane can be expressed, to third-order in energy deviation, as:

$$z = z_0 + R_{56}\eta + T_{566}\eta^2 + U_{5666}\eta^3, \tag{7.3}$$

where $\eta = (\gamma - \gamma_0)/\gamma$ is the usual relative energy deviation variable. For a simple four-magnet chicane we have: $T_{566} = -R_{56}3/2$, $U_{5666} = 2R_{56}$.

The combined effects of the non-linear energy-chirp and non-linear longitudinal transport generates a triangular current distribution after compression with a sharp spike in the head of the beam (see Fig.7.5). While the spike itself has a very large energy-spread it still gives a large contribution to the amplification process, due to its high peak current. Since the high-gain region of the beam has a length on the order of the slippage length in the final undulator, a spectrum with few spectral spikes is expected.

Figure 7.5 shows a diagram of current as a function of longitudinal position and the associated longitudinal phase-space for the electron beam after chicane 2 from a 1-D simulation model. The simulation was performed with the approach described in [17], where the effect of the longitudinal space-charge fields in each drift space is described in terms of a beam impedance averaged over the drift length. The simulation contains 3-D effects due to the finite beam size and energy-spread effects in chicane transport. This approximate modeling gives an intuition about the effect of the non-linear compression scheme on the gain mechanism and on the spectral properties of the emitted radiation.

7.3 Experimental results

In this section we present the results of the LSCA experiment. The goal of the experiment was to give a demonstration of the most important features of the LSCA mechanism:

-high-gain (of several orders of magnitude);

-broad spectral bandwidth;

-transverse coherence;

-cascading.

The diagnostic setup for the coherent undulator radiation is shown in Fig. 7.6: a near and a far-field camera are used to characterize the transverse structure of

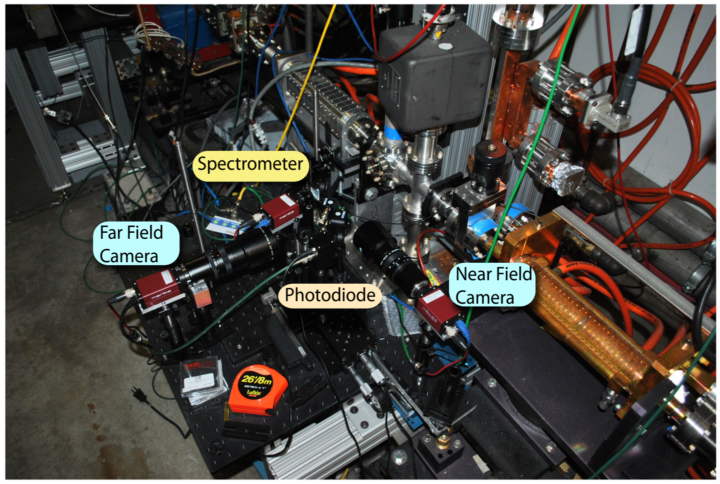

Figure 7.6: Diagnostic setup for the LSCA: a near and a far-field camera are used to characterize the transverse structure of the radiation, while the spectrometer camera is used for spectral measurements. A photodiode is setup to measure absolute gain.

the radiation, while the spectrometer camera is used for spectral measurements. A photodiode is setup to measure absolute gain. A system of mirror flippers was used to switch from one diagnostic device to the other.

In the experiment the chicane setup was held fixed and compression was scanned by varying the accelerating phase of station 1. In general this method perturbs the orbit and transport of the electrons, since the focusing properties of the RF accelerating fields are dependent on the accelerating phase. In this case, however, this problem was not important since a significant amplification was only observed in a narrow window of phase values (see, for example, Fig, 7.9). This allowed us to tune the beam transport at an accelerating phase close to the optimum phase (roughly 10 degrees away from maximum compression) avoiding the effects of coherent transition radiation on the beam diagnostics. After the machine tuning was completed, a small variation in phase allowed us to observe coherent radiation with a negligible effect on the beam transport.

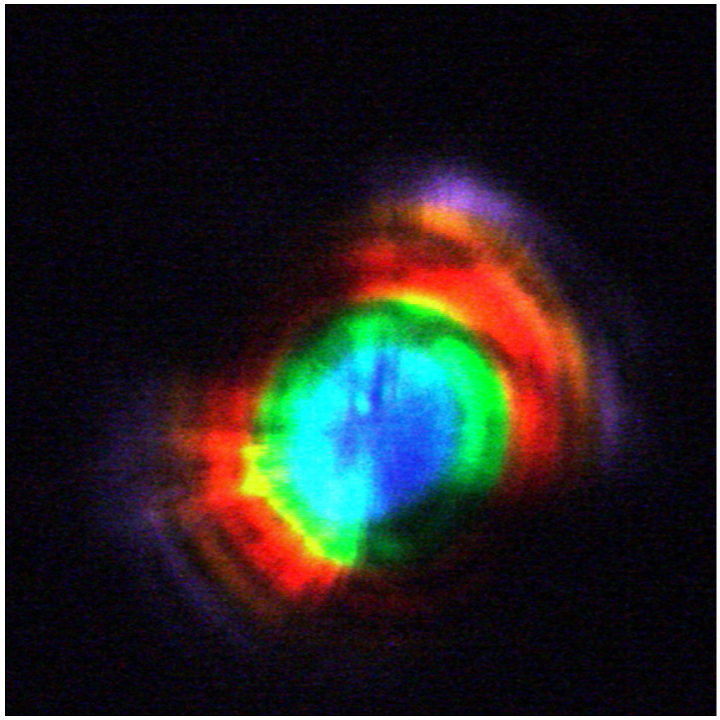

Figure 7.7: True-color far-field radiation pattern from the compressed electron beam radiating through a 77-period radio-frequency undulator. The strong angular dependece and the broad frequency content of the radiation wavelength, extending all the way from violet to red, illustrates the broad-band nature of the space-charge instability.

Note that, while the final undulator selects a broad but finite emission bandwidth, the LSCA generates microbunching over a larger bandwidth, ranging down to sub-optical wavelengths. Figure 7.7 shows a real-color far-field image of coherent undulator radiation from the RF undulator. Due to the large number of periods $N_{w,RF} = 78$, the emission bandwidth for each angle is rather narrow, giving a sharp frequency/angle correlation. Figure 7.7 gives a striking demonstration of the broadband feature of the LSCA microbunching amplification mechanism.

The experiment was performed operating at different values of charge. The most significant results were obtained in the range of $Q \simeq 8 \div 12pC$. The initial

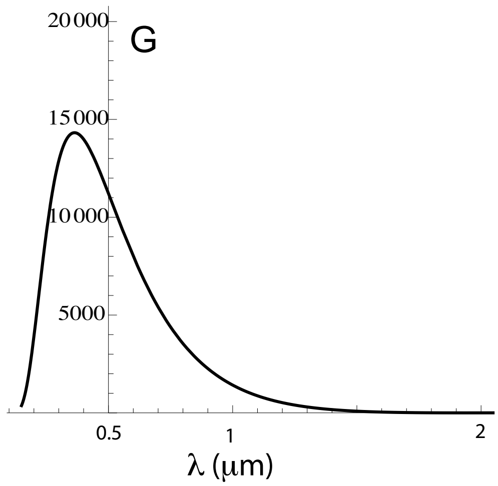

Figure 7.8: Microbunching power gain as a function of wavelength for the NLCTA beam parameters in the single-spike regime, from the linear theory. The overall compression factor is C = 15.

root mean square (RMS) beam length was roughly $\sigma_z = c \times 1psec$. The transverse beam size was measured to be respectively $\sigma_{x,1} \simeq 160\mu m$ and $\sigma_{x,2} \simeq 150\mu m$ in the drift spaces after chicane-0 and chicane-1. For the first amplification stage, we estimate that most of the gain happens in the last 10 meters before chicane-0, where the average beam-size is $\sigma_{x,0} \simeq 250\mu m$. Note that the electron beam is not axisymmetric: the x and y rms widths are different and there are strong x-y correlations. The numbers reported are an estimate of the size of an axisymmetric electron beam that has the same transverse area as the measured beam. For the measured beam size before chicane-0, the microbunching is transversely coherent if starting from wavelengths on the order of $\lambda_{in} \simeq 10\mu m$, which requires a compression factor of $C \simeq 15$ for single transverse mode operation

7.3.1 Single-spike regime

The best results in terms of gain were observed with the following chicane setup: $R_{56,0} = 4mm$, $R_{56,1} = 2.5mm$, $R_{56,2} = 1.5mm$ and a beam energy of $E_b = 72.5MeV$ at full compression. Figure 7.8 shows the microbunching gain spectrum for this configuration for an overall compression factor of $C = 15$. The gain peaks in the optical spectral region for the idealize linear gain model. Figure 7.9 shows the integrated signal on the near-field camera as a function of the accelerating phase for this chicane configuration. Significant gain with respect to spontaneous radiation is obtained over a phase range of about 10 degrees. To get an accurate measurement of the absolute integrated intensity gain, we used a high dynamic range photodiode detector. The average gain in integrated intensity with respect to spontaneous emission, measured at $Q = 12pC$, is $I_{max}/I_{inc} \simeq 600$ with peaks up to 1000. Note that the angular width of the coherent radiation is narrower than the incoherent. Furthermore, as discussed in section 7.2.2, only a fraction of the electron bunch contributes to the coherent emission, while the entire electron bunch contributes to incoherent emission. This means that the local microbunching power gain, in the region of high microbunching, is higher than the intensity gain. By comparing the coherent and incoherent far-field distributions, we measure a larger angular width for the incoherent radiation by a factor 2.2. Furthermore, from the numerical simulations discussed in section 7.2.2, we estimate that the current peak that drives the microbunching process has contains roughly 20% of the bunch charge. It follows that the local microbunching power can be estimated to be four orders of magnitude above the shot-noise level.

Figure 7.10 shows the coherent undulator radiation spectrometer image for the highest gain phase and for intermediate gain. A spectrometer image corresponds to a two-dimensional correlation plot of intensity as a function of wavelength and

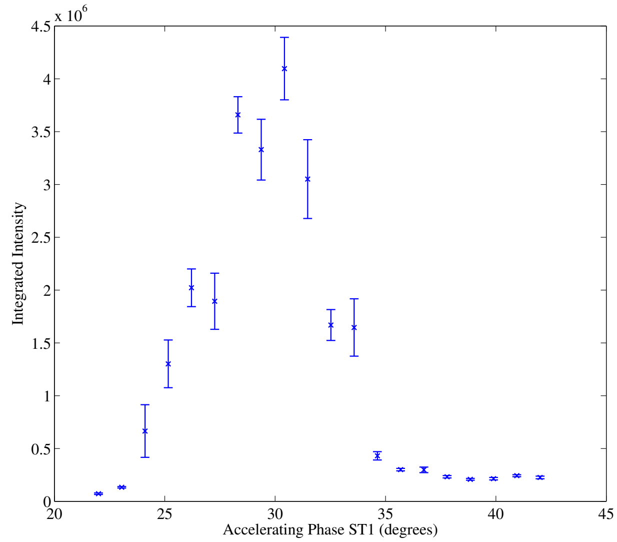

Figure 7.9: Integrated signal on the far-field camera as a function of accelerating phase in station 1. The emitted radiation energy increases with increasing compression reaching an optimum for maximum compression. For phases larger than $\simeq 30$ deg the beam is overcompressed, giving a fast decay of the coherent emission with accelerating phase.

vertical angle $\theta_y = k_y/k_z$. The intermediate gain configuration corresponds to a weaker current compression than the peak gain. For this value of compression, the spectrum exhibits a spiky structure, due to the fact that the slippage length in the undulator is shorter than the fraction of the beam that contributes to coherent emission. Note also that for moderate compression the coherent field exhibits speckles in the transverse dimension (see the θ_y dependence of the intensity). In the optimal compression case, instead, the spectrometer shows a single spectral spike and a single transverse mode. As the result of strong compression, the microbunched fraction of the beam is shorter than the slippage length, resulting in the single spike spectrum. The transverse single mode, instead, is due to the wavelength shift of the transversely uniform far-infrared microbunching to optical wavelengths. The on-axis FWHM bandwidth is $\Delta\lambda/\lambda \simeq 10\%$, corresponding to

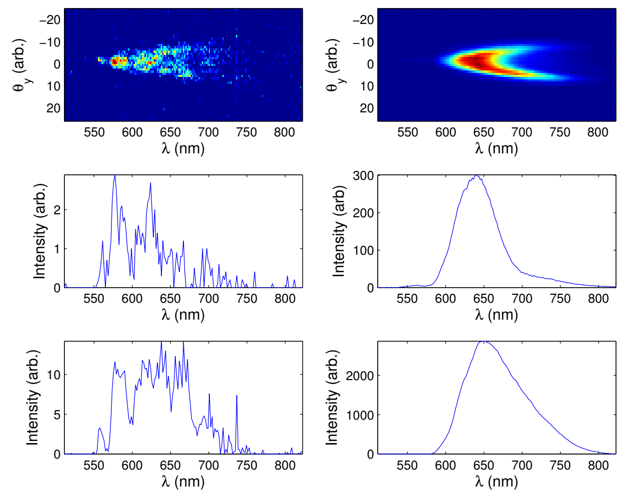

Figure 7.10: Spectrometer image (upper imgaes), on-axis spectrum (middle images) and integrated spectrum (lower images) from a fully compressed image (right images) and for moderate compression (left images). The figure shows the transition from a spiky regime to the single spike regime, in which slippage of the radiation over the compressed electron bunch generates a single spectral mode. Note also how a single smooth transverse mode is achieved as the result of compression. The FWHM bandwidth on axis is $\Delta\lambda \simeq 65nm$.

the on-axis emission bandwidth of the undulator. The integrated spectrum has a wider bandwidth $\Delta\lambda/\lambda \simeq 14\%$ since the off-axis emission happens at longer wavelengths than on-axis emission.

Figure 7.11 shows a single-shot far-field image of coherent undulator radiation. As inferred from the spectrometer image, the far-field transverse distribution exhibits a single mode structure. As mentioned above, this results from the effect of wavelength compression from the far-infrared to optical wavelengths, which transfers the transverse coherence properties of the long-wavelength microbunching to the optical spectrum.

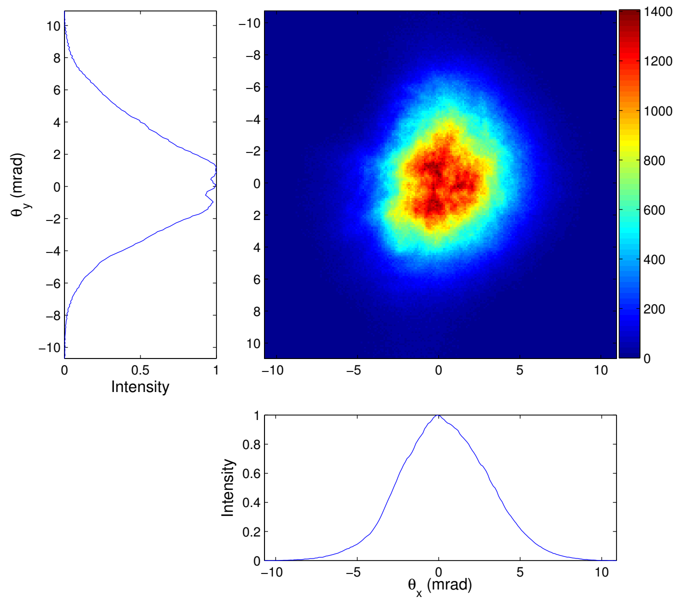

Figure 7.11: Far-field undulator radiation image at maximum compression. This image shows the transverse structure of the emitted radiation for the configuration yielding the highest radiated energy. The image shows a single transverse mode, which is the result of compression of far-infrared microbunching to optical wavelengths.

7.3.2 Multi-spike regime

To better characterize the LSCA mechanism, we performed an experiment with a chicane setup yielding an overall larger total R_{56} compared to the case discussed in the previous sub-section. The chicane configuration is $R_{56,0} = 5mm$, $R_{56,1} = 5mm$, $R_{56,2} = 4mm$.

In this regime, the length of the current spike that contributes to gain is larger than in the previous case, which causes the undulator slippage length to cover only a fraction of the microbunched part of the electron beam. Furthermore, this high R_{56} configuration favors gain at long wavelengths, resulting in an overall shift

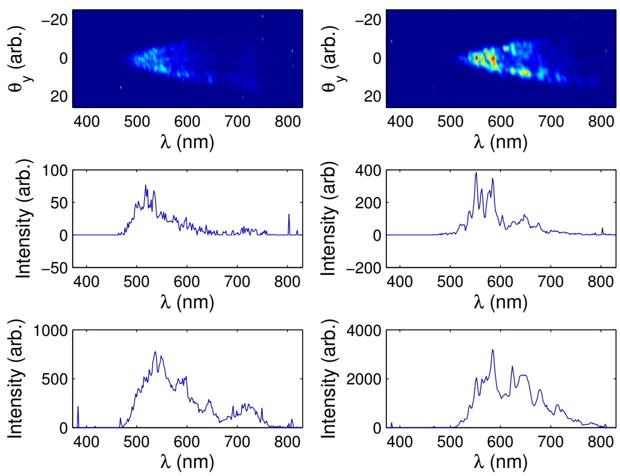

Figure 7.12: Spectrometer image (upper images), on-axis spectrum (middle images) and integrated spectrum (lower images) from a fully compressed image (right images) and for moderate compression (left images). In this high R_{56} configuration, the spectrum is spiky even in the case of highest compression.

of the coherent emission towards the infrared spectral region. The absolute gain measurement in this regime yields an overall gain of a factor 5 smaller than the previously discussed case (an average of $I_{max}/I_{inc} \simeq 120$ with peaks of 200), this decrease in intensity, however, is mostly due to the narrow angular distribution (see Fig. 7.13) which yields a lower angle-integrated signal.

7.4 Demonstration of Cascaded Gain

While high gain was demonstrated with the gain measurements described in the previous section, cascading requires a separate discussion. In fact, the observation of high-gain through a system of three chicanes does not guarantee that the gain process is multiplicative along the three stages. Moreover, the observation of increased microbunching from one chicane to another does not prove multiplica-

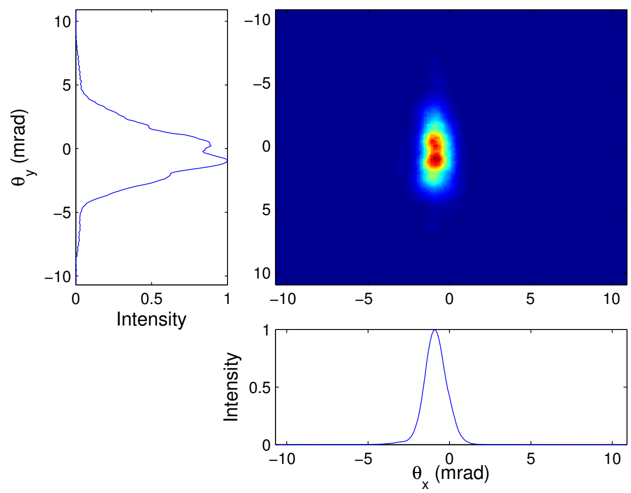

Figure 7.13: Far-field image for the spiky spectrum case. The far-field still exhibits a clean single-mode structure due to strong compression.

tive gain. In fact, the three chicanes might be converting the energy modulation generated before chicane-0 into microbunching, gradually along the beamline, which would result in an additive gain process rather than a multiplicative one.

Cascaded amplification can be proved by changing the relative values of the individual R_{56}s but keeping the sum constant. In this case, if the gain process is additive instead of multiplicative, varying the relative values of the dispersion does not change the final gain, whereas in the case of cascaded gain it would significantly affect it. Figure 7.14 shows the integrated signal on the near-field camera for four different chicane configurations yielding the same total R_{56}. The figure shows a comparison with the theoretical prediction for the microbunching gain, with the assumption of linear compression and with the measured beam parameters. The last three configurations can be obtained from the original one ($4mm - 3mm - 2mm$) by switching the R_{56} of two chicanes piecewise. The measurements were performed adjusting the beamline so that the beamsize between the three chicanes would remain roughly constant. This was accomplished by compensating the change in vertical focusing due to the chicane magnets with the magnetic quadrupoles. The plot shows a variation of the intensity with different chicane configurations, which is an indication of cascaded gain. Note that, even though the product of the three R_{56} is constant the gain is still expected to change since the compression factor C at each chicane changes for each configuration. We also note that the configuration with decreasing R_{56} shows the highest intensity gain, in good agreement with our theoretical model.

The last data shows some disagreement with the theory, which predicts a smaller gain than observed. This is likely due to non-linear compression, which is not included in the theoretical model. In the growing R_{56} configuration, in fact, most of the compression happens in the last chicane. This means that the microbunching is not confined to the leading current peak and it is more uniformly distributed along the electron bunch than in the decreasing R_{56} configuration. In this case, a larger fraction of the bunch contributes to the coherent emission compared to the previous cases, an effect that compensates the lower microbunching gain.

7.5 Conclusions

In this chapter we have discussed the first experimental demonstration of a cascaded longitudinal space-charge amplifier. Coherent radiation induced by the microbunching instability was demonstrated in the past in several experiments, in the context of transition radiation diagnostics for FEL drive beams. The difference with respect to previous experiments is that, in our case, the instability was controlled and optimized to generate intense and transversely coherent undulator radiation pulses. This provides a proof of principle demonstration for the

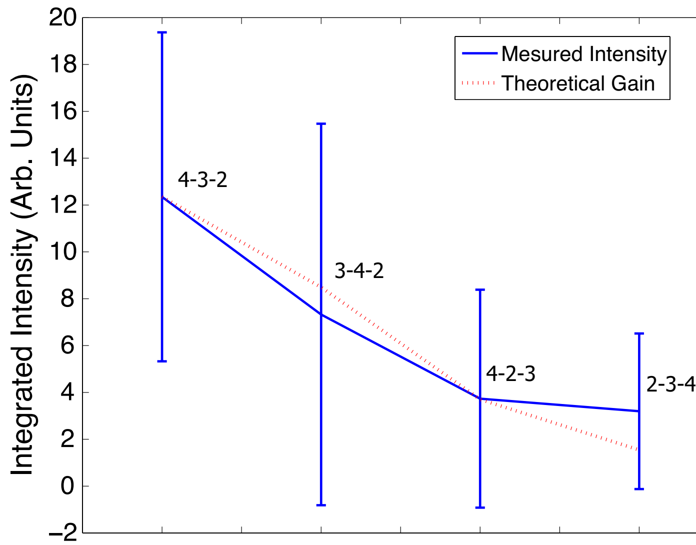

Figure 7.14: Integrated camera intensity for four different chicane configurations $R_{56,0} - R_{56,1} - R_{56,2}$ (measured in mm), yielding the same total R_{56}. The maximum intensity is achieved for decreasing R_{56} (first data point). The red dotted curve shows the theoretical prediction, based on the assumption of linear compression, normalized to the first experimental point. Changing the partition of the longitudinal dispersion keeping the sum constant changes the intensity gain, which is a signature of cascaded microbunching gain over the three chicanes.

generation of broad-band coherent radiation at fourth generation light sources.

In particular, the experiment has demonstrated high-intensity, broadband coherent undulator radiation pulses from an electron beam modulated by the longitudinal space-charge instability. The regime of strong compression due to chirped beam operation, results in coherent radiation pulses with a single transverse mode, consistently with our theoretical understanding of the amplfication/compression process. Due to the short duration of the electron bunch, a single spectral mode has been observed under conditions of strong compression.

Finally, cascading between the three chicanes has been proved by scanning the relative values of the three R_{56}s and keeping the total compression constant (i.e. keeping the same total R_{56}). Cascading is a crucial feature of the LSCA which will enable, in the future, high gain at sub-optical wavelengths.

CHAPTER 8

Single shot reconstruction of beam microbunching by phase-retrieval of optical transition radiation images

The generation, compression and transport of such high-density, cold relativistic electron beams in FEL injectors poses several challenges, especially due to beam collective instabilities that develop during acceleration and transport, that amplify the beam's shot-noise-derived microbunching. As discussed in the introductory part of this dissertation, this effect generates strong perturbations in the beam's longitudinal phase-space, which serve to reduce the efficiency of the FEL process in the downstream undulator [48, 12] and induce the emission of coherent radiation in beam diagnostic stations [24, 27, 52, 53]. While the effect of the microbunching instability on the FEL performance can be mitigated using a laser heater, this does not suppress the emission of coherent optical transition radiation (COTR) to a manageable level [12] making the use of beam profile monitors impractical for compressed electron beams.

In this chapter we discuss a method for the reconstruction of the transverse spatial structure of beam microbunching from a single-shot, far-field coherent optical transition radiation (COTR) image, and report on the experimental demonstration of this technique at the Next Linear Collider Test Accelerator (NLCTA), located at the SLAC National Accelerator Center. The technique proposed is general and can be applied to any type of microbunching, such as the microbunching generated by the FEL interaction or by the microbunching instability [21, 30] or to a helical microbunching structure used to drive the emission of orbital angular momentum modes in FELs [54, 44]. In particular, in this chapter we will focus on the specific case of microbunching generated by the interaction of the beam with an external laser pulse in a magnetic undulator, henceforth referred to as laser induced microbunching (LIM). This specific case is particularly convenient, since it allows the benchmarking of our technique using and incoherent optical transition radiation (OTR) image, thus allowing a proof of principle demonstration of this technique. The reconstruction of LIM is also of importance for the diagnostics of compressed electron beams, such as the ones used to drive high-gain x-ray FELs. As mentioned above, the diagnosis of these beams is severely compromised by the emission of COTR, which makes it impossible to directly measure the transverse profile of the beam with a simple near field OTR image. Recently several methods have been proposed to avoid this problem, by using fluorescent screens that emit in the UV spectral region [55], or combining a scintillation screen with a gated optical camera [56]. However, phosphorescent-screen-based measurements are are affected by beam surface-field-driven image blooming [57], which limits the resolution of these imaging techniques. The reconstruction of LIM, that is demonstrated in this chapter, allows the reconstruction of compressed beams even in the presence of the microbunching instability. In fact if the beam microbunching has a uniform transverse distribution (as is the case of LIM from a laser pulse that is transversely larger than the electron beam) the transverse distribution of the microbunching provides a direct map of the beam density distribution, extending the applicability of commonly used diagnostic techniques based on (incoherent) OTR to beams that are strongly affected by collective instabilities through use of the dominant coherent signal. This overall approach has also been proposed in a related context of reconstructing the beam's longitudinal profile, in a scheme known as an optical replica synthesizer, or ORS [58]. In contrast, we will refer to the transverse reconstruction technique introduced in this chapter as the transverse optical replica (TOR).

8.1 Reconstruction Method

The emission of coherent radiation from a relativistic electron beam requires the formation of a density modulation on the scale of the radiation wavelength. This type of density modulation, generally termed beam microbunching, is commonly quantified by the bunching factor, defined as the Fourier transform of the beam longitudinal density profile normalized to the number of particles:

$$b(k) = \frac{1}{N}\int dxdydz\ \rho(x,y,z)e^{-ikz} = \frac{1}{N}\sum_n e^{-ikz_n} \tag{8.1}$$

where z is the longitudinal position along the beam axis, x, y are the transverse positions, $\rho(x,y,z)$ is the three-dimensional beam density distribution, N is the number of electrons in the beam and z_n is the longitudinal position of the n_{th} electron. The bunching factor is nearly equal to 0 for a beam with a uniform density profile, with a small component due to shot-noise. On the other hand approaches unity ($b(k) = 1$) if the electrons are arranged in z into periodic structures smaller than the relevant period wavelength, $\lambda = 2\pi/k$.

For a beam with microbunching above the shot-noise level, the radiated power from a given emission process (e.g. transition radiation or undulator radiation) scales proportionally with $|b(k)|^2N^2$; in the case of randomly distributed electrons in which the emission is incoherent, the bunching factor scales as $1/N^{1/2}$ and the total radiated power scales proportionally to N.

While the one-dimensional bunching factor b captures the basic features of cooperative radiation processes, in many cases it is more useful to keep track of the transverse distribution of the density modulation and give a generalized three-dimensional definition of the bunching factor as the longitudinal Fourier transform of the three-dimensional beam volume density:

$$b(x, y, k) = \frac{1}{N} \int dz \rho(x, y, z) e^{-ikz}. \tag{8.2}$$

The goal of our experiment is that of reconstructing the spatial dependence of $b(x, y, k_z)$ from a single-shot, far field COTR image. The far field COTR differential power spectrum emitted by a microbunched beam is given by

$$\frac{dP}{d\omega d\Omega} = \frac{dP}{d\omega d\Omega}|_{sp} N^2 |B(k_x, k_y, k_z)|^2, \tag{8.3}$$

where $\frac{dP}{d\omega d\Omega} = \frac{e^2}{4c\epsilon_0\pi^3} \frac{\beta^2 \sin^2\theta}{(1-\beta^2\cos^2\theta)^2}$ indicates the single particle differential spectrum, e is the electron charge, c is the speed of light, ϵ_0 is the vacuum permittivity and β is the beam velocity normalized to the speed of light. The polar angle is related to k_x, k_y, k_z by $\cos\theta = \frac{\sqrt{k_x^2+k_y^2}}{\sqrt{k_x^2+k_y^2+k_z^2}}$. The form factor B is defined as the three-dimensional Fourier transform of the beam's charge density distribution:

$$B(k_x, k_y, k_z) = \frac{1}{N} \int dx dy dz \ \rho(x, y, z) e^{-ik_x x - ik_y y - ik_z z}. \tag{8.4}$$

Note that $b(x, y, k_z)$ and $B(k_x, k_y, k_z)$ are a two-dimensional Fourier transform pair, i.e.

$$B(k_x, k_y, k_z) = \int dx dy \ b(x, y, k_z) e^{-ik_x x - ik_y y}. \tag{8.5}$$

From the above definitions, it follows that, from a single shot, far-field COTR image one can measure the amplitude of B. The spatial dependence of the beam microbunching can, in principle, be recovered by an inverse discrete Fourier transform (DFT). However, to invert the DFT one needs information about the complex phase of B, which cannot be inferred directly from the far-field image. However, it has been understood in recent years that the phase of a two-dimensional signal can be recovered by means of an iterative phase-retrieval algorithm, provided that $|B(k_x, k_y, k_z)|$ is sampled with high enough resolution in the frequency domain. The condition that needs to be satisfied is $dk < \pi/L$ where dk is the resolution in the transverse frequency domain and L is the characteristic size of the beam in the space-domain. In practice, L is the size of a finite support in x, y that fully contains the signal. This condition is often referred to as the oversampling condition.

Iterative phase-retrieval algorithms (see e.g. [59, 60]) are now used in a great number of advanced applications, such as coherent diffraction imaging of non-crystalline samples [61]. Figure 8.1 shows a schematic of the algorithm. The retrieval algorithm starts by applying a random phase to the signal in the frequency domain (or reciprocal space). An inverse fast Fourier transform (IFFT) is then applied to obtain a trial signal in the spatial domain. At this point a given set of constraints (discussed below) is applied in the spatial-domain and a fast Fourier transform (FFT) is performed. Finally, one substitutes the amplitude in the frequency domain with the measured amplitude while keeping the phase from the FFT.This process is repeated for several iterations (typically a few hundreds to thousands) until the amplitude of the final FFT is equal to the measured amplitude within a small tolerance.

The constraints applied in the spatial domain depend on the type of measurement performed but usually include a support constraint, i.e. the signal in x, y is constrained to be equal to zero outside of a given finite support. The size of the finite support depends on the oversampling ratio of the measured amplitude in frequency domain [59]. Furthermore, if the beam microbunching is real and positive in the spatial-domain, a positivity constraint can be applied by keeping just the real part of the spatial-domain signal and setting to zero all the data points that have a negative value. This kind of constraint increases the speed of the reconstruction algorithm and ensures the uniqueness of the solution [59]. The latter constraint can be applied in the case of LIM, which is the case of interest for this chapter. This can be understood by noting that a seed laser with a flat transverse profile generates a density distribution of the type

$$\rho_{und} = \rho(x,y,z)\left(1 + 2\sum_n a_n \cos(nk_z z)\right), \tag{8.6}$$

where $a_n = J_n(nk_z\delta\eta R_{56})e^{-k_z^2\sigma_\eta^2 R_{56}^2}$, J_n is n_{th} order Bessel function of the first kind, $\delta\eta$ is the amplitude of the laser-induced energy modulation normalized to the beam energy, σ_η is the relative energy-spread and R_{56} is the longitudinal dispersion of the bunching magnetic chicane. The resulting microbunching distribution is given by $b(x,y,k_z) = \frac{a_1}{N}\int dz\rho(x,y,z)$ which is an everywhere positive function that represents the transverse profile of the beam.

8.2 Experimental demonstration

To test this reconstruction method, we have performed a seeded COTR experiment at the NLCTA. The schematic layout of the experiment is shown in Fig.8.2. The experimental setup corresponds to the first part of the ECHO beamline [50, 51]. An electron beam of energy $E = 120$ MeV is sent through an undulator, copropagating together with a resonant laser of wavelength $\lambda = 800$ nm. The resonant interaction generates an energy modulation in the electron beam which

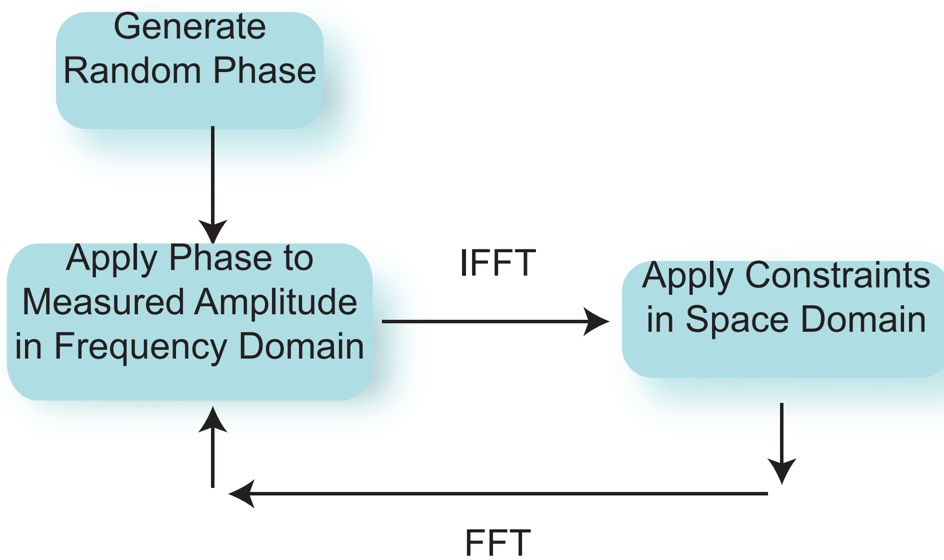

Figure 8.1: Schematics of a phase-retrieval algorithm.

is then transformed into density modulation by a subsequent magnetic chicane. The electron beam is then sent through a metal foil, causing the emission of a COTR pulse that is collected by a CCD camera focused to infinity. Figure 8.3 shows a picture of the seeding beamline.

The imaging system is composed of two CCD cameras (see Fig. 8.4). The first camera is focused to infinity to collect the far-field coherent image. A second camera is focused on the metal foil to collect a near field image of the incoherent OTR that is used to benchmark the reconstruction. The diagnostic switches from one camera to the other by means of a mirror flipper. Note that the seed laser leaks through the chicane mirror (see Fig. 8.2) and affects the measurement. A simple solution to this problem is that of slightly off-setting the emission frequency of COTR by introducing a small linear energy chirp in the electron beam and using an optical filter to select the shifted emission wavelength.

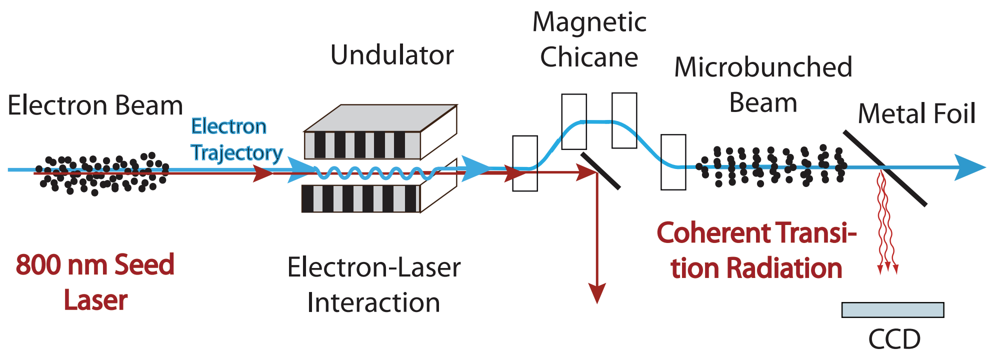

Figure 8.2: Layout of the experimental setup.

The seed laser has a transverse size that is significantly larger than the electron beam, giving a nearly transversely uniform electric field that interacts with the beam electrons. Under these conditions, the microbunching is, to an excellent approximation, a replica of the transverse shape of the electron beam. Since in the experiment we worked with an uncompressed beam which is not notably affected by the microbunching instability, the measurement can be benchmarked by comparison with a near-field incoherent OTR image obtained without the LIM applied. Figure 8.5 shows a far-field COTR image and the inferred beam form factor. Note that, since the COTR single particle differential intensity is zero on axis, the beam form factor cannot be measured for $k_x \simeq 0, k_y \simeq 0$. The amplitude of B close to the axis is then reconstructed by the retrieval algorithm simply keeping the amplitude and phase of the IFFT near the axis as the last step of each iteration. This issue is analogously found in coherent diffraction imaging experiments, where the near axis diffraction pattern is dominated by the direct beam (see e.g. Ref. [61]) and it is commonly referred to as the missing center problem. Figure 8.6 shows the reconstructed phase of B and the resulting transverse dependence of the beam microbunching $b(x, y, k_z)$.

The NLCTA photoinjector-derived beam possesses small shot-to-shot fluctu-

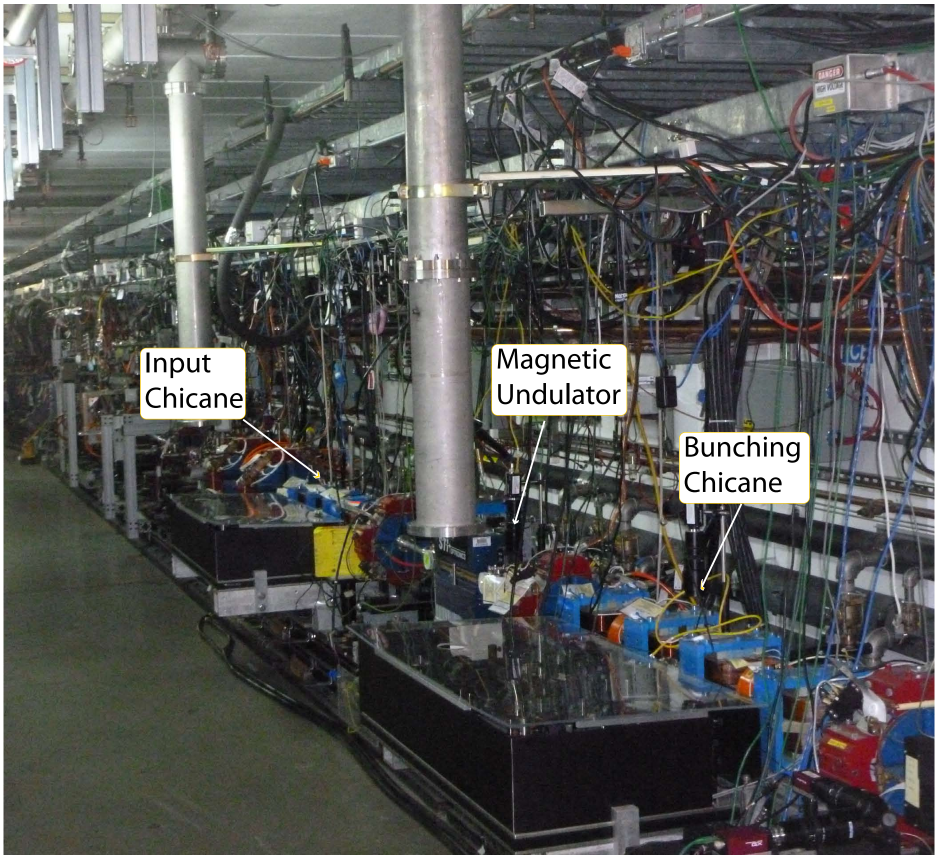

Figure 8.3: Photograph of the seeding beamline.

ations of the beam transverse shape, which gives some slight variations in the comparison beam profiles, thus allowing a less than exact benchmarking of this measurement. Nevertheless, there are many repeatable features of the beam profile that bear comparison. Figures 8.7 and 8.9 show a comparison between several reconstructed bunches and near-field OTR images for two different beamline configurations, yielding two significantly different beam profiles. The incoherent OTR images show some fluctuations in the beam shape. However, as noted above, the characteristic size and shape of the beam consistently reproduced in the reconstructed microbunching images. Finally, Fig. 8.8 shows a reconstructed

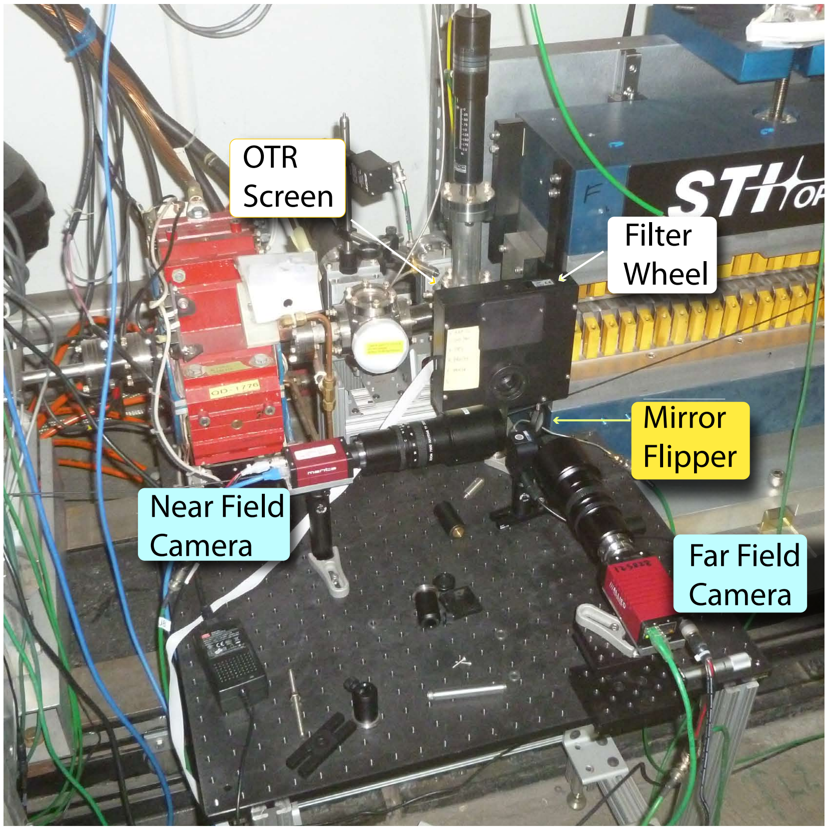

Figure 8.4: Photograph of the diagnostic system.

microbunching and the corresponding OTR image with a comparison of the x and y projected profiles. We note that the near-field OTR images are calibrated by taking an image of the OTR screen fiducials, while the far-field COTR images are calibrated with an incoherent far-field OTR measurement, which has a peak at $\sqrt{k_x^2 + k_y^2} = k_z/\gamma$. The two calibrations are consistent, as shown in Fig. 8.7. This indicates that the method can be used quantitatively to image compressed beams when near-field OTR imaging is impossible.

Indeed, both incoherent and coherent OTR-based diagnostics methods may be undesirable due to their destructive nature. In this regard, the technique described and demonstrated in this chapter would be greatly enhanced by the use of non-destructive coherent undulator radiation, as proposed in the original ORS

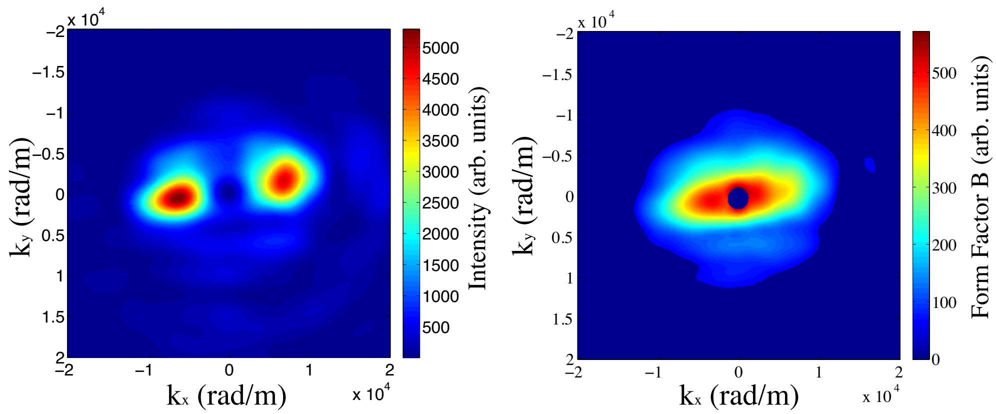

Figure 8.5: Raw far-field COTR image (left image) and inferred amplitude of the beam's form factor (right image).

scheme. This scenario would evade the problem of zero emission on axis, which limits the amount of information gathered with COTR near the $k_x \simeq 0, k_y \simeq 0$ far-field region. A further refinement to the method employed here would involve the simultaneous use of near- and far-field COTR images, which would greatly improve microbunching reconstruction by imposing a more stringent set of constraints for the phase-retrieval algorithm.

8.3 Conclusions

In this chapter we have introduced, and experimentally tested, a technique for the single-shot reconstruction of the transverse shape of beam microbunching for a relativistic electron beam. This technique is based on far-field COTR imaging and on the application of a phase-retrieval algorithm. The technique is general and could be applied to the case of arbitrary microbunching structures. We have demonstrated this method in the case of uniform microbunching generated by resonant interaction of the electrons with an external laser pulse in an undulator.

This case is of great relevance to x-ray free-electron lasers since it extends the customary beam profile monitor techniques based on OTR to compressed beams, even in the presence of coherent light emission induced by the microbunching instability. Further, we note that by combining this measurement to those discussed in [58], one may obtain a 3D replica of the beam distribution. Finally, in the absence of externally imposed microbunching, the method promises to be a keen tool in unfolding the details of transverse spatial distribution of the collective instability-induced microbunching itself.

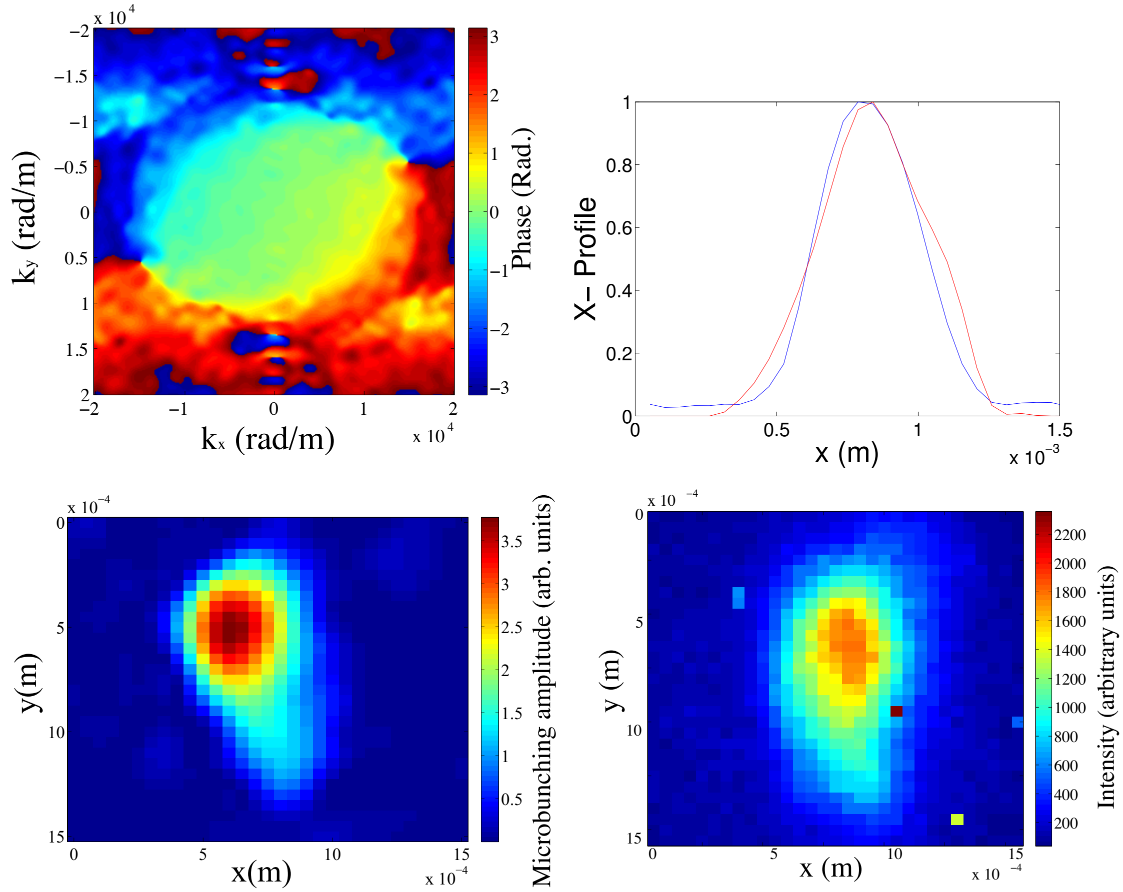

Figure 8.6: Reconstructed phase in the frequency domain (upper left image) and reconstructed microbunching in the space-domain (bottom left image). For comparison an incoherent OTR image is shown in the bottom right image. The upper right image shows the x-profile of the electron beam from the reconstruction and from the incoherent OTR.

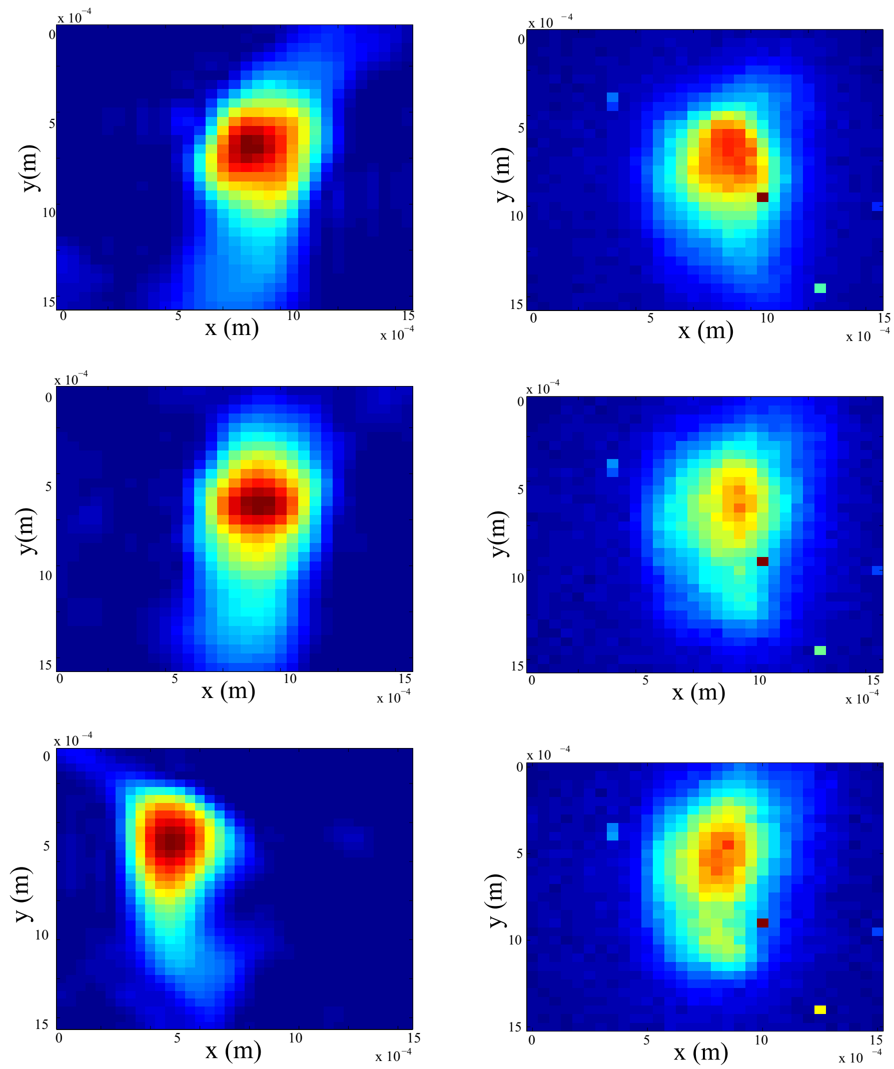

Figure 8.7: Reconstructed microbunching (left images) and near field OTR image (right images) for several independent shots.

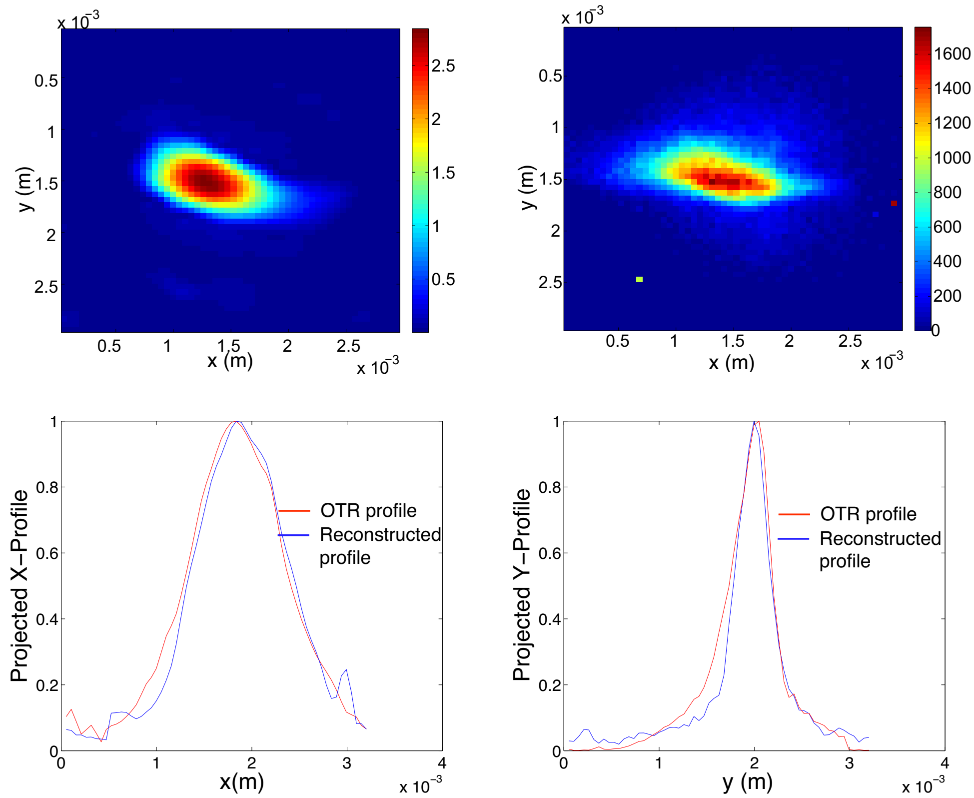

Figure 8.8: Reconstructed microbunching (upper left image) and near field OTR image (upper right image) for a beamline configuration yielding a horizontal beam. The bottom images show the x and y projected profiles of both images.

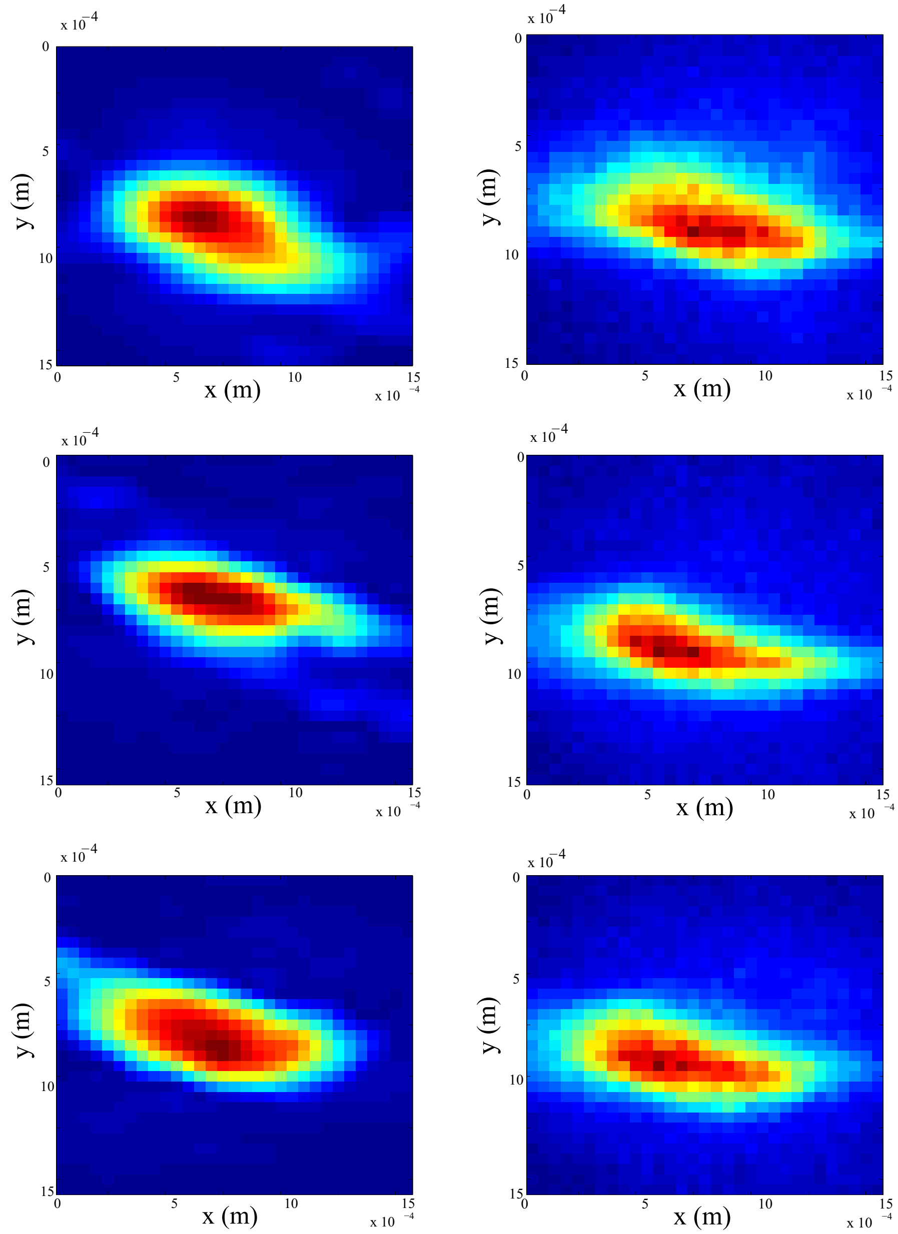

Figure 8.9: Reconstructed microbunching (left images) and near field OTR image (right images) for several independent shots.

CHAPTER 9

General Conclusions

9.1 Concluding Remarks

The main topic of this dissertation has been the space-charge microbunching instability. Experimental evidence for this effect in free-electron laser (FEL) injectors was found at several facilities, where the induced microbunching causes the emission of coherent transition radiation. The microbunching instability is usually regarded as a parasitic effect since the induced microbunching strongly disturbs the beam diagnostics in particle accelerators and generates perturbations in the beam phase-space which compromise the efficiency of the FEL. Recently, however, the space-charge microbunching instability has been proposed as a coherent microbunching amplifier for advanced free-electron laser seeding schemes, a configuration that is now referred to as Longitudinal Space-Charge Amplifier (LSCA).

The physics of this instability is rather complex and is strictly related to that of relativistic plasma oscillations. Previous theoretical work on this subject relied on the "frozen beam" approximation, in which the electrons do not move with respect to each other during the collective interaction. While this simple two-step cold-beam theory captures the basic features of the microbunching instability, understanding thermal motion due to emittance and betatron motion, and the effect of beam plasma oscillations induced by the self-consistent response of the beam, is very important for the design and optimization of advanced microbunching experiments, such as shot-noise suppression or coherent microbunching amplification.

Our theoretical approach is based on a kinetic theory of space-charge waves in six-dimensional phase-space and consists of three different steps:

1) finding the propagating eigenmodes of space-charge waves in six-dimensional phase-space;

2) using the self-consistent eigenmodes as an expansion basis for an arbitrary initial phase-space perturbation to (i.e. solving the initial value problem)

3) using the general formalism derived in the first two steps to describe the collective evolution and amplification of beam microbunching.

In chapter 2 we described the propagating eigenmodes of the space-charge fields. We derived a dispersion relation for the plasma eigenmodes and expressed it in terms of four dimensionless scaling parameters. The dispersion relation was solved for a broad range of the scaling parameters and used to describe several properties of the beam plasma oscillations. In chapter 3 we studied the coupling of these modes to an arbitrary initial perturbation of the six-dimensional phase-space distribution. These two chapters provided a theoretical description of the self-consistent evolution of a phase-space perturbation under the effect of space-charge, which was used in chapter 4 to model the amplification of microbunching due to the combined effects of space-charge interactions and longitudinal dispersion in bending magnets. Finally, in chapter 5 we developed a quasi-three dimensional model for the microbunching instability of a transversely large beam with no transverse focusing, a case in which the modal analysis described in the previous chapters fails due to the degeneracy of the plasma eigenmodes.

One of the most important features of this theoretical model is the study of transverse motion due to emittance. This effect is very important since it ultimately determines the transverse distribution of the beam microbunching. We demonstrated how transverse motion can increase the transverse coherence of the amplification process, strongly suppressing the amplification of higher order modes. In particular, when the beam travels in a focusing channel, transverse motion gives rise to plasma-betatron beat-waves for higher order transverse modes, with a fast oscillation of the microbunching due to the betatron oscillations, superimposed on the slow collective response of the electrons. In this case, the amplification of complex transverse structures is suppressed due to the slower plasma response with respect to the laminar beam approximation.

Another important effect due to transverse emittance is the longitudinal velocity spread induced by transverse motion. This is a second order effect, since the longitudinal velocity deviation of a particle due to its finite betatron amplitude is given by $\dot{z}_\epsilon = -(k_\beta \vec{x}^2 + \vec{\beta}_\perp^2)/4$. Since the velocity deviation due to emittance is always negative, this effect induces an anisotropy in the plasma response of the beam, causing strong Landau damping of the space-charge waves that propagate in the negative z-direction (relative to the electron beam). The Landau damping due to emittance is a critically important effect which ultimately determines the optimal focusing for a space-charge experiment. We used our theory to describe emittance effects in both shot-noise suppression and microbunching amplification experiments. We showed how the optimal design of such experiments has to balance the field enhancement due to strong transverse focusing and the longitudinal velocity spread due to emittance which dominates the behavior of strongly focused beams. Finally, the reduction of the plasma oscillation frequency due to the finite size of the beam was determined to be a critical effect, suppressing the microbunching amplification at long wavelengths.

In the one-dimensional limit (i.e. the limit for a large quasi-laminar electron beam), total mode degeneracy makes the use of the bi-orthogonal mode expansion highly impractical. For this specific case, we developed a quasi three-dimensional model in which the electron beam is modeled as a uniform unmagnetized plasma and the evolution of beam microbunching is analyzed in terms of plane plasma waves. Our model shows how transverse motion due to emittance induces strong Landau damping of high $k_\perp$ components of optical microbunching, reducing the angular width of the gain induced by space-charge. As a general rule, the characteristic transverse coherence length of the microbunching is given by $\gamma\lambda$, or by the Debye length λ_D whichever is larger. This effect is critical for the coherent optical transition radiation diagnostics of the microbunching instability, since it determines the angular distribution of the coherent signal.

After establishing a strong theoretical background for the space-charge instability, we performed a proof of principle experimental demonstration of the longitudinal space-charge amplifier (LSCA). In an LSCA, the longitudinal space-charge microbunching instability is employed to generate a strong modulation in the electron beam, which is then used to generate coherent radiation in an undulator. The experiment was performed at the NLCTA test facility and demonstrated the key features of a LSCA: broadband ($\Delta\lambda/\lambda \simeq 15\%$), high-gain (up to three orders of magnitude over spontaneous emission), cascaded amplification and single transverse mode operation. A single transverse mode is obtained as the result of strong compression, which shifts the transversely coherent microbunching generated at long wavelenghts to the optical spectral region. Strong compression also results in a single spectral spike in cases in which the slippage length in the radiator is shorter than the microbunched portion of the electron bunch. Cascaded amplification was proved by varying the R_{56} partition along the amplification beamline and keeping the total compression factor constant. This experiment proves the feasibility of broad-band coherent radiation sources at free-electron laser user facilities and opens new possibilities for the free-electron laser user community.

Finally, we developed and demonstrated experimentally a coherent diffraction imaging technique for the reconstruction of beam microbunching. This technique relies on far-field imaging of coherent transition radiation pulses and on the application of an iterative phase-retrieval algorithm. The technique is general and could be applied to any type of microbunching. We have successfully tested this method with laser-induced optical microbunching at the NLCTA test facility. As mentionedin chapter 8, this experiment has a wide number of applications in the diagnostics of compressed electron beams in free-electron laser injectors or as a diagnostic for advanced free-electron laser experiments.

9.2 Future Directions of Investigation

The physics of longitudinal space-charge effects has raised significant interest in the free-electron laser community and the broader field of particle accelerators. The experimental demonstration of the LSCA accomplished in this PhD dissertation opens new lines of research in advanced FEL seeding schemes. The next generation of experiments will have to demonstrate the emission of ultra-short pulses with a LSCA seeded by an ultra-fast external laser and the extension of the LSCA to VUV and soft x-ray wavelengths.

While the LSCA holds great promise as a source of coherent broad-band radiation, I believe that alternative amplification mechanisms need to be pursued to improve the operation of broad-band coherent amplifiers at short wavelengths (specifically the nanometer level and sub-nanometer level). I am currently investigating the two-stream amplifier (2SA) as an alternative to the LSCA, with a number of collaborators. The 2SA shares the same conceptual layout as an LSCA: a collective instability is used to generate microbunching (starting from shot-noise or an external seed), which is then employed in an undulator for the emission of coherent photons. However, unlike the LSCA, in this case the amplification mechanism consists of the unstable response of an electron beam with two distinct energy levels. This type of instability is driven by longitudinal space-charge but it does not require a magnetic chicane since the microbunching grows exponentially as a function of time. The three-dimensional theory of this effect, based on the same formalism developed in this dissertation, is currently being investigated and future experiments at the NLCTA are in the planning stages.

The coherent imaging technique developed in this dissertation is also being expanded to measure more general forms of microbunching. In fact, extending this method to cases where the microbunching has large phase variations in the transverse plane presents several challenges. This is the case of the space-charge induced microbunching for a degenerate beam, or the helical microbunching that drives orbital angular momentum modes in an FEL. A more robust reconstruction method can be achieved with simultaneous near and far-field imaging of coherent transition radiation. With this approach, a stronger constraint can be applied to the signal in the space-domain, ensuring convergence of the phase-reconstruction algorithm even for cases in which sign constraints cannot be imposed.

The lines of research opened by this dissertation will generate new and exciting science in the near future, and will contribute to the development of ultra-fast radiation sources aiming to reach the attosecond level at the next generation of light sources.

References

[1] M. M. Seibert, Ekeberg T., F. Maia, M. Svenda, and al. Single mimivirus particles intercepted and imaged with an x-ray laser. *Nature*, 470:78–81, 2011.

[2] H. N. Chapman, P. Fromme, A. Barty, T. A. White, R. A. Kirian, and al. Femtosecond x-ray protein nanocrystallography. *Nature*, 470:73–77, 2011.

[3] P. Emma and al. First lasing and operation of an angstrom-wavelength free-electron laser. *Nat Photon*, 4:641–647, Aug 2010.

[4] J D Jackson. Longitudinal plasma oscillations. *Journal of Nuclear Energy. Part C, Plasma Physics, Accelerators, Thermonuclear Research*, 1(4):171, 1960.

[5] S. M. Vinko, O. Ciricosta, B. I. Cho, K. Engelhorn andH. K. Chung, C. R. D. Brown, and al. Creation and diagnosis of a solid-density plasma with an x-ray free-electron laser. *Nature*, 482:59–62, 2012.

[6] N. Rohringer, D. Ryan, R. London, M. Purvis, and al. Atomic inner-shell x-ray laser at 1.46 nanometres pumped by an x-ray free-electron laser. *Nature*, 481:488–491, 2012.

[7] Pellegrini, C. The history of x-ray free-electron lasers. *Eur. Phys. J. H*, 2012.

[8] P. Musumeci, J. T. Moody, R. J. England, J. B. Rosenzweig, and T. Tran. Experimental generation and characterization of uniformly filled ellipsoidal electron-beam distributions. *Phys. Rev. Lett.*, 100:244801, Jun 2008.

[9] R. Bonifacio, C. Pellegrini, and L.M. Narducci. Collective instabilities and high-gain regime in a free-electron laser. *Optics Communications*, 50(6):373–378, Jul 1984.

[10] Ming Xie. Exact and variational solutions of 3d eigenmodes in high gain fels. *Nuclear Instruments and Methods in Physics Research Section A: Accelerators, Spectrometers, Detectors and Associated Equipment*, 445(1-3):59 – 66, 2000.

[11] M. Borland, Y.C. Chae, P. Emma, J.W. Lewellen, V. Bharadwaj, W.M. Fawley, P. Krejcik, C. Limborg, S.V. Milton, H.-D. Nuhn, R. Soliday, and M. Woodley. Start-to-end simulation of self-amplified spontaneous emission free electron lasers from the gun through the undulator. *Nuclear Instruments*

and Methods in Physics Research Section A: Accelerators, Spectrometers, Detectors and Associated Equipment, 483(1-2):268 – 272, 2002.

[12] Z. Huang, A. Brachmann, F.-J. Decker, Y. Ding, D. Dowell, P. Emma, J. Frisch, S. Gilevich, G. Hays, Ph. Hering, R. Iverson, H. Loos, A. Miahnahri, H.-D. Nuhn, D. Ratner, G. Stupakov, J. Turner, J. Welch, W. White, J. Wu, and D. Xiang. Measurements of the linac coherent light source laser heater and its impact on the x-ray free-electron laser performance. *Phys. Rev. ST Accel. Beams*, 13:020703, Feb 2010.

[13] E. A. Schneidmiller and M. V. Yurkov. Using the longitudinal space charge instability for generation of vacuum ultraviolet and x-ray radiation. *Phys. Rev. ST Accel. Beams*, 13(11):110701, Nov 2010.

[14] A. Gover and E. Dyunin. Collective-interaction control and reduction of optical frequency shot noise in charged-particle beams. *Phys. Rev. Lett.*, 102(15):154801, Apr 2009.

[15] Daniel Ratner, Zhirong Huang, and Gennady Stupakov. Analysis of shot noise suppression for electron beams. *Phys. Rev. ST Accel. Beams*, 14(6):060710, Jun 2011.

[16] Daniel Ratner and Gennady Stupakov. Observation of shot noise suppression at optical wavelengths in a relativistic electron beam. *Phys. Rev. Lett.*, 109:034801, Jul 2012.

[17] M. Dohlus, E. A. Schneidmiller, and M. V. Yurkov. Generation of attosecond soft x-ray pulses in a longitudinal space charge amplifier. *Phys. Rev. ST Accel. Beams*, 14:090702, Sep 2011.

[18] F. Ferrari, F. Calegari, M. Lucchini, C. Vozzi, S. Stagira, G. Sansone, and M. Nisoli. High-energy isolated attosecond pulses generated by above-saturation few-cycle fields. *Nat Photon*, 4:875–879, Nov 2010.

[19] Alexander A. Zholents and William M. Fawley. Proposal for intense attosecond radiation from an x-ray free-electron laser. *Phys. Rev. Lett.*, 92:224801, Jun 2004.

[20] Marco Venturini. Models of longitudinal space-charge impedance for microbunching instability. *Phys. Rev. ST Accel. Beams*, 11(3):034401, Mar 2008.

[21] D. Ratner, A. Chao, and Z. Huang. Three dimensional analysis of longitudinal space-charge microbunching starting from shot-noise. *Proceedings of the 2008 Free-Electron Laser Conference*, page 338, 2008.

[22] Gianluca Geloni, Evgeni Saldin, Evgeni Schneidmiller, and Mikhail Yurkov. Theory of space-charge waves on gradient-profile relativistic electron beam: An analysis in propagating eigenmodes. *Nuclear Instruments and Methods in Physics Research Section A: Accelerators, Spectrometers, Detectors and Associated Equipment*, 554(1-3):20 – 48, 2005.

[23] Juhao Wu, Zhirong Huang, and Paul Emma. Analytical analysis of longitudinal space charge effects for a bunched beam with radial dependence. *Phys. Rev. ST Accel. Beams*, 11(4):040701, Apr 2008.

[24] A. H. Lumpkin, Y. C. Chae, J. W. Lewellen, W. J. Berg, M. Borland, S. G. Biedron, R. J. Dejus, M. Erdmann, Z. Huang, K. J. Kim, Y. Li, S. V. Milton, E. R. Moog, D. W. Rule, V. Sajaev, and B. X. Yang. Evidence for transverse dependencies in cotr and microbunching in a sase fel. *Nuclear Instruments and Methods in Physics Research Section A: Accelerators, Spectrometers, Detectors and Associated Equipment*, 507(1-2):200–204, 2003.

[25] H. Loos and et al. Observation of coherent optical transition radiation in the lcls linac. *Proceedings of the 2008 Free-Electron Laser Conference (Gyeongju, Korea)*, page p. 619, August 2008.

[26] S. Wesch and et al. *Proceedings of the 2009 Free-Electron Laser Conference (Liverpool, UK)*, page 485, August 2009.

[27] A. H. Lumpkin, N. S. Sereno, W. J. Berg, M. Borland, Y. Li, and S. J. Pasky. Characterization and mitigation of coherent-optical-transition-radiation signals from a compressed electron beam. *Phys. Rev. ST Accel. Beams*, 12:080702, Aug 2009.

[28] G. Stupakov and S. Heifets. Beam instability and microbunching due to coherent synchrotron radiation. *Phys. Rev. ST Accel. Beams*, 5:054402, May 2002.

[29] Zhirong Huang and Kwang-Je Kim. Formulas for coherent synchrotron radiation microbunching in a bunch compressor chicane. *Phys. Rev. ST Accel. Beams*, 5:074401, Jul 2002.

[30] Agostino Marinelli and James B. Rosenzweig. Microscopic kinetic analysis of space-charge induced optical microbunching in a relativistic electron beam. *Phys. Rev. ST Accel. Beams*, 13(11):110703, Nov 2010.

[31] John David Jackson. *Classical Electrodynamics*, volume 2011. 1998.

[32] M. L. Ter-Mikaelian. *High-energy electromagnetic processes in condensed media*. Wiley-Interscience, 1972.

[33] V.A. Lebedev. Diffraction-limited resolution of the optical transition radiation monitor. *Nuclear Instruments and Methods in Physics Research Section A: Accelerators, Spectrometers, Detectors and Associated Equipment*, 372(3):344 – 348, 1996.

[34] D. W. Rule and R. B. Fiorito. Imaging micron-sized beams with optical transition radiation. *AIP Conference Proceedings*, 229(1):315–321, 1991.

[35] Yukio Shibata, Kimihiro Ishi, Toshiharu Takahashi, Toshinobu Kanai, Fumitaka Arai, Shin-ichi Kimura, Toshiaki Ohsaka, Mikihiko Ikezawa, Yasuhiro Kondo, Ryukou Kato, Shigekazu Urasawa, Toshiharu Nakazato, Satoshi Niwano, Masahiro Yoshioka, and Masayuki Oyamada. Coherent transition radiation in the far-infrared region. *Phys. Rev. E*, 49(1):785–793, Jan 1994.

[36] A. Tremaine, J. Rosenzweig, S. Anderson, P. Frigola, M. Hogan, A. Murokh, C. Pellegrini, D. Nguyen, and R. Sheffield. Measured free-electron laser microbunching using coherent transition radiation. *Nuclear Instruments and Methods in Physics Research Section A: Accelerators, Spectrometers, Detectors and Associated Equipment*, 429(1-3):209–212, 1999.

[37] Brian M. Kincaid. A short-period helical wiggler as an improved source of synchrotron radiation. *Journal of Applied Physics*, 48(7):2684–2691, 1977.

[38] L. Landau. On the vibration of the electronic plasma. *J. Phys. USSR 10, 25 (1946) [JETP 16, 574 (1946)].*

[39] P. Musumeci, R. K. Li, and A. Marinelli. Nonlinear longitudinal space charge oscillations in relativistic electron beams. *Phys. Rev. Lett.*, 106:184801, May 2011.

[40] Kwang-Je Kim. Three-dimensional analysis of coherent amplification and self-amplified spontaneous emission in free-electron lasers. *Phys. Rev. Lett.*, 57(15):1871–1874, Oct 1986.

[41] L. H. Yu, S. Krinsky, and R. L. Gluckstern. Calculation of universal scaling function for free-electron-laser gain. *Phys. Rev. Lett.*, 64(25):3011–3014, Jun 1990.

[42] A. Marinelli, E. Hemsing, and J.B. Rosenzweig. Three dimensional analysis of longitudinal plasma oscillations in a thermal relativistic electron beam. *Phys. Plasmas 18, 103105 (2011).*

[43] Ronald C. Davidson, W. Wei li Lee, Hong Qin, and Edward Startsev. Implications of the electrostatic approximation in the beam frame on the nonlinear vlasov–maxwell equations for intense beam propagation. *Physics of Plasmas*, 9(1):340–344, 2002.

[44] E. Hemsing, A. Marinelli, and J. B. Rosenzweig. Generating optical orbital angular momentum in a high-gain free-electron laser at the first harmonic. *Phys. Rev. Lett.*, 106:164803, Apr 2011.

[45] Ming Xie. Grand initial value problem of high gain free electron lasers. *Nuclear Instruments and Methods in Physics Research Section A: Accelerators, Spectrometers, Detectors and Associated Equipment*, 475(1-3):51 – 58, 2001. ¡ce:title¿FEL2000: Proc. 22nd Int. Free Electron Laser Conference and 7th F EL Users Workshop¡/ce:title¿.

[46] Zhirong Huang and Kwang-Je Kim. Three-dimensional analysis of harmonic generation in high-gain free-electron lasers. *Phys. Rev. E*, 62:7295–7308, Nov 2000.

[47] Agostino i, Erik Hemsing, and James B. Rosenzweig. Three dimensional analysis of longitudinal plasma oscillations in a thermal relativistic electron beam: Application to an initial value problem. *Physics of Plasmas*, 19(6):063108, 2012.

[48] Z. Huang, M. Borland, P. Emma, J. Wu, C. Limborg, G. Stupakov, and J. Welch. Suppression of microbunching instability in the linac coherent light source. *Phys. Rev. ST Accel. Beams*, 7:074401, Jul 2004.

[49] J. Qiang, R.D. Ryne, M. Venturini, A. A. A. A. Zholents, and I.V. Pogorelov. *Phys. Rev. ST Accel. Beams*, 12:100702, Aug 2009.

[50] D. Xiang, E. Colby, M. Dunning, S. Gilevich, C. Hast, K. Jobe, D. McCormick, J. Nelson, T. O. Raubenheimer, K. Soong, G. Stupakov, Z. Szalata, D. Walz, S. Weathersby, M. Woodley, and P.-L. Pernet. Demonstration of the echo-enabled harmonic generation technique for short-wavelength seeded free electron lasers. *Phys. Rev. Lett.*, 105:114801, Sep 2010.

[51] D. Xiang, E. Colby, M. Dunning, S. Gilevich, C. Hast, K. Jobe, D. McCormick, J. Nelson, T. O. Raubenheimer, K. Soong, G. Stupakov, Z. Szalata, D. Walz, S. Weathersby, and M. Woodley. Evidence of high harmonics from echo-enabled harmonic generation for seeding x-ray free electron lasers. *Phys. Rev. Lett.*, 108:024802, Jan 2012.

[52] H. Loos and et. al. *Proceedings of the 2008 Free-Electron Laser Conference, Gyeongju, Korea*, page 485., 2008.

[53] S. Wesch and et. al. *Proceedings of the 2009 Free-Electron Laser Conference, Liverpool, UK*, page 619, 2009.

[54] E. Hemsing, P. Musumeci, S. Reiche, R. Tikhoplav, A. Marinelli, J. B. Rosenzweig, and A. Gover. Helical electron-beam microbunching by harmonic coupling in a helical undulator. *Phys. Rev. Lett.*, 102:174801, Apr 2009.

[55] A. Lumpkin and et. al. *Proceedings of PAC 2009*, pages 3546–3548., 2009.

[56] M. Yan and et. al. *Proceedings of DIPAC 2011, Hamburg, Germany*, pages 440–442., 2011.

[57] A. Murokh and et al. Limitations on measuring a transverse profile of ultra-dense electron beams with scintillators. *Proceedings of the 2001 Particle Accelerator Conference, Chicago*, pages 1333–1335, 2001.

[58] E.L. Saldin, E.A. Schneidmiller, and M.V. Yurkov. A simple method for the determination of the structure of ultrashort relativistic electron bunches. *Nuclear Instruments and Methods in Physics Research Section A: Accelerators, Spectrometers, Detectors and Associated Equipment*, 539(3):499 – 526, 2005.

[59] J. Miao, D. Sayre, and H. N. Chapman. Phase retrieval from the magnitude of the fourier transforms of nonperiodic objects. *J. Opt. Soc. Am. A*, 15(6):1662–1669, Jun 1998.

[60] J. R. Fienup. Phase retrieval algorithms: a comparison. *Appl. Opt.*, 21(15):2758–2769, Aug 1982.

[61] Jianwei Miao, Pambos Charalambous, Janos Kirz, and David Sayre. Extending the methodology of x-ray crystallography to allow imaging of micrometre-sized non-crystalline specimens. *Nature.*, 400:342–344, July 1999.